6 Results

6.1 Limits set by the solar spectrum

In this chapter some basic considerations concerning the maximum attainable conversion efficiency of solar irradiation into electric energy are discussed. The figures given and most of the analysis are based on the formulas given in the textbook "Physik der Solarzelle" [157].

Fig. 6.1a depicts the photon flux as a function of wavelength for a black body with the temperature of the sun (5800 K) and the AM1.5 spectrum. AM stands for airmass and describes the optical path length through the earth's atmosphere. The airmass with the sun in the zenith is by definition one. An airmass of 1.5 correspond to an angle of 48.2 ° and an airmass of 0 describes the photon flux in space.

Since some of the incident light of the sun is scattered and adsorbed in the atmosphere, the AM1.5 spectrum deviates significantly from the spectrum of a black body. The gaps at 760 nm, 940 nm and 1140 nm reflect the absorption of light by water. The gaps at ca. 1400 nm and ca. 1900 nm the absorption of carbon dioxide and water. In general the AM1.5 spectrum is red-shifted compared to the AM0 spectrum. In the UV-region a significant fraction of the incident light is absorbed mainly by ozone, whereas in the IR-region some of the irradiation emitted by the earth is reflected by clouds (greenhouse effect).
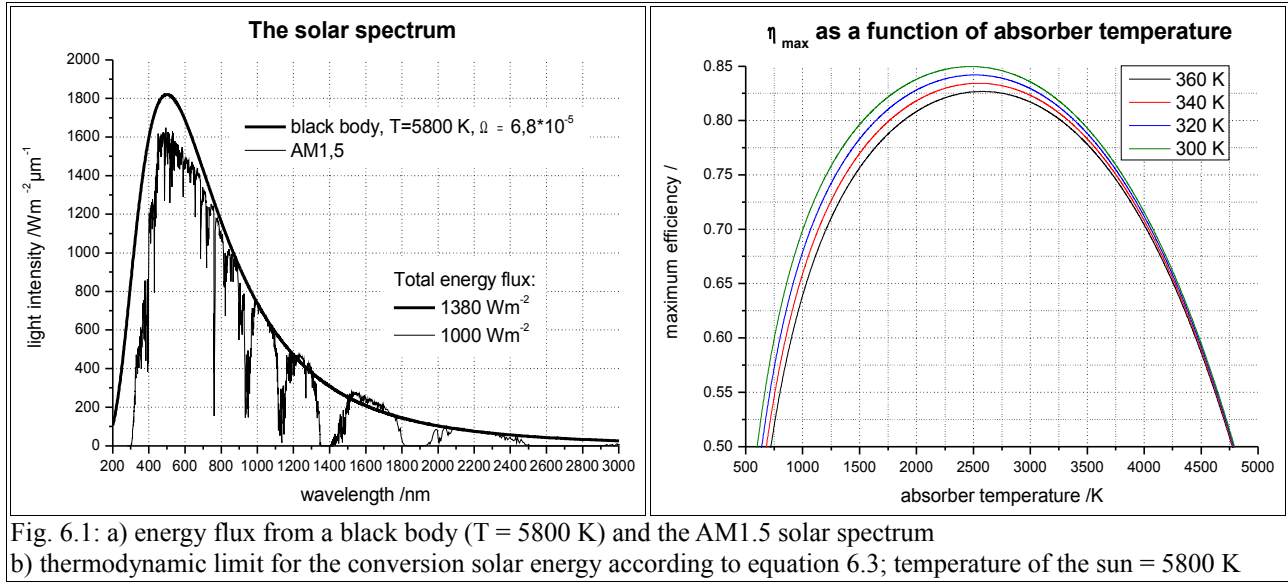
Fig. 6.1: a) energy flux from a black body (T = 5800 K) and the AM1.5 solar spectrum
b) thermodynamic limit for the conversion solar energy according to equation 6.3; temperature of the sun = 5800 K

From a thermodynamic point of view the solar cell can be considered to be an ideal Carnot-machine. The absorber of the solar cell is the hot bath, which is in equilibrium with the solar irradiation, and the surrounding is the cold bath. The useful energy E_{use}, which might be taken from the incoming irradiation is the difference between the solar irradiation $E_{sun,absorbed}$ and the photon flux that is emitted by the absorber $E_{absorber,emitted}$. Using the Stefan-Boltzmann law this gives

$$E_{use} = E_{sun,absorbed} - E_{absorber,emitted} = \frac{\Omega_L}{\pi} * \sigma * (T_{sun}^4 - T_{absorber}^4) \quad (6.1)$$

E_{use} = useful energy flux /W*m^{-2}; Ω_L = solid angle = 6.8*10^{-5}; σ = Stefan-Boltzmann constant=5.67*10^{-8} WK^{-4}m^{-2};
T_{sun} = temperature of the sun /K; $T_{absorber}$ = temperature of the absorber /K

and the efficiency of this process is

$$\eta_{use} = \frac{E_{use}}{E_{sun,absorbed}} = 1 - \frac{T_{absorber}^4}{T_{sun}^4} \quad (6.2)$$

η_{use} = fraction of the solar irradiation that is converted; $T_{absorber}$ = temperature of the absorber /K; T_{sun} = temperature of the sun /K

The useful energy E_{use} is converted into electric efficiency in a Carnot process with a hot and a cold

bath. The maximum efficiency of the Carnot process is achieved when the change in entropy is zero. The maximum efficiency of a Carnot-cycle is given by

$$\eta_{Carnot} = 1 - \frac{T_{surrounding}}{T_{absorber}} \quad (6.3)$$

η_{Carnot} = fraction of the absorbed energy that is converted into electricity; $T_{surrounding}$ = temperature of the surrounding /K; $T_{absorber}$ = temperature of the absorber /K

The total efficiency for solar energy conversion is then given by

$$\eta_{max} = \eta_{Carnot} * \eta_{use} = (1 - \frac{T_{surrounding}}{T_{absorber}}) * (1 - \frac{T_{absorber}^4}{T_{sun}^4}) \quad (6.4)$$

η_{max} = maximum attainable efficiency; η_{Carnot} = fraction of the absorbed energy that is converted into electricity; η_{use} = fraction of the solar irradiation that is absorbed;

Fig. 6.1b depicts the maximum attainable efficiency η_{max} as a function of absorber temperature. The temperature of the surrounding was 300, 320, 340 and 360 K respectively, which covers the range in which a solar cell normally operates. At room temperature η_{max} is 85 % with an absorber temperature of 2478 K. η_{max} decreases linearly with the temperature of the surrounding (equation 6.3) with a slope of ca. -0.045 %/K. For example, if the temperature of the surrounding changes from 25 °C to 85 °C, the thermodynamic conversion efficiency decreases by 2.7 %.

The thermodynamic efficiency does not say anything about how the electric energy is extracted from the system. Most solar cells behave similar to an ideal diode with a current-voltage characteristic following Shockley's diode equation [158].

$$I = I_S * (e^{\frac{eV}{kT}} - 1) - I_{Ph} \quad (6.5)$$

I = current density /mAcm^{-2}; I_S = reverse saturation current /mAcm^{-2}; e = 1.6022*10^{-19} C; T = temperature /K; k = Boltzmann constant = 1.38066*10^{-23} /JK^{-1}; V = voltage /V; I_{ph} = photocurrent /mAcm^{-2}

The saturation current I_S in this model is caused by thermally induced recombination/generation processes. For a single junction solar cell and neglecting non-irradiative processes I_S can be expressed as

$$I_S = \int_{e_g}^{\infty} \frac{2e^4 V^2}{h^3 c^2} * \left(\frac{1}{e^{\frac{eV}{kT_{surrounding}}} - 1} \right) dV \quad (6.6)$$

whereas the photocurrent is

$$I_{Ph} = \int_{e_g}^{\infty} \frac{2e^4 V^2}{h^3 c^2} * \left(\frac{1}{e^{\frac{eV}{kT_{sun}}} - 1} \right) dV \quad (6.7)$$

I_S = reverse saturation current /mAcm^{-2}; e_g = bandgap /V; e = 1.6022*10^{-19} C; V = voltage /V;

k = Boltzmann constant = 1.38066*10^{-23} /JK^{-1}; h = Planck's constant = 6.626*10^{-34} Js; c = speed of light = 3*10^8 ms^{-1};

T_{sun} = temperature of the sun /K;

With equation 6.5 - 6.7 and with

$$\eta_{max, diode} = \frac{I_{MPP} * V_{MPP}}{\int_{e_g}^{\infty} \frac{2e^4 V^2}{h^3 c^2} * \left(\frac{1}{e^{\frac{eV}{kT_{sun}}} - 1} \right) dV * V_{OC}} \quad (6.8)$$

I_{MPP} = current at maximum power point /mAcm^{-2}; V_{MPP} = voltage at maximum power point; V_{OC} = open circuit potential;

one can calculate the maximum efficiency with diode losses $\eta_{max,diode}$ as a function of bandgap energy. Fig. 6.2b shows the graphs for a black body with the temperature of the sun (close to AM0) and the graphs for AM1.5 spectra at different temperatures. It is interesting to note that the $\eta_{max,diode}$ for a band gap <2.2 eV is higher on earth than in space. This is due to the broad absorption of carbon dioxide and water in the infrared region, which does not contribute to the power output of a solar cell anyway. At room temperature $\eta_{max,diode}$ is 35.8 % at bandgap energies of 1.15 and 1.35 eV respectively. The region, in which $\eta_{max,diode}$ > 34 % ranges from 0.99 - 1.50 eV. Thus a large variety of semiconductors are potentially good absorbers for solar cells. With rising temperature, the conversion efficiency $\eta_{max,diode}$ decreases because the reverse saturation current increases – as a first approximation – exponentially with the temperature. At 85 °C $\eta_{max,diode}$ is 26 % lower compared to

an ambient temperature of 25 %. This is almost one order of magnitude more than the decrease observed in the "Carnot" solar cell.

The maximum conversion efficiency $\eta_{max,diode}$ of a solar cell operating at 0 K is depicted in Fig. 6.2a. At 0 K, the fillfactor of a solar cell is 100 % and the power output is given by the product of open circuit potential and short circuit current. Under AM1.5 $\eta_{max,diode}$ is 49.1 % at 1.12 eV and $\eta_{max,diode}$ > 47 % in the range from 0.90 eV to 1.25 eV. That means that the ideal band gap energy decreases with decreasing temperatures.
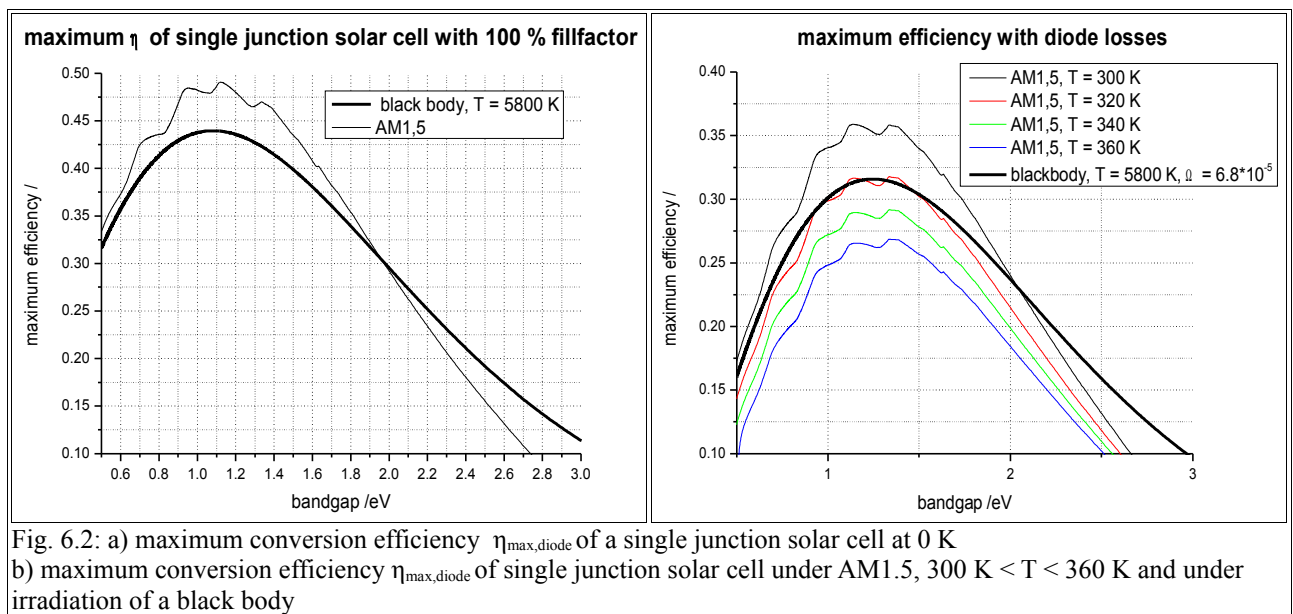

Fig. 6.2: a) maximum conversion efficiency $\eta_{max,diode}$ of a single junction solar cell at 0 K
b) maximum conversion efficiency $\eta_{max,diode}$ of single junction solar cell under AM1.5, 300 K < T < 360 K and under irradiation of a black body

For every single junction solar cell the upper theoretical limit for the conversion efficiency is determined by the band gap (semiconductor cells) or the excitation energy of the absorber (DSSC, organic solar cells). Photons that exceed this threshold energy E_G may excite an electron, but the excess energy is lost in a thermalization step whereas photons with an energy below E_G are not absorbed. The concept of multiple junction solar cells with n absorbers is to make use of a broader range of the solar spectrum. Each absorber has a specific bandgap energy E_g. Absorbers with high band gap energies decrease the thermalization losses wheres absorbers with low energies can also convert infrared irradiation. Fig. 6.3 depicts $\eta_{max,diode}$ in the case n = 2 for a black body with T = 5800 K and $\Omega = 6.8 \times 10^{-5}$ (close to AM0 spectrum). The highest efficiency can be obtained for two absorbers with bandgap energies of $E_{G,1} = 0.9$ eV and $E_{G,2} = 1.7$ eV, which is 43.8 %. With increasing number of junctions, $\eta_{max,diode}$ approaches a limit, which is 85 % for n = ∞. This is the same value, which was already found with the thermodynamic considerations in the beginning of

this chapter.

Fig. 6.3: maximum conversion efficiency $\eta_{max,diode}$ for a solar cell with two different absorbers
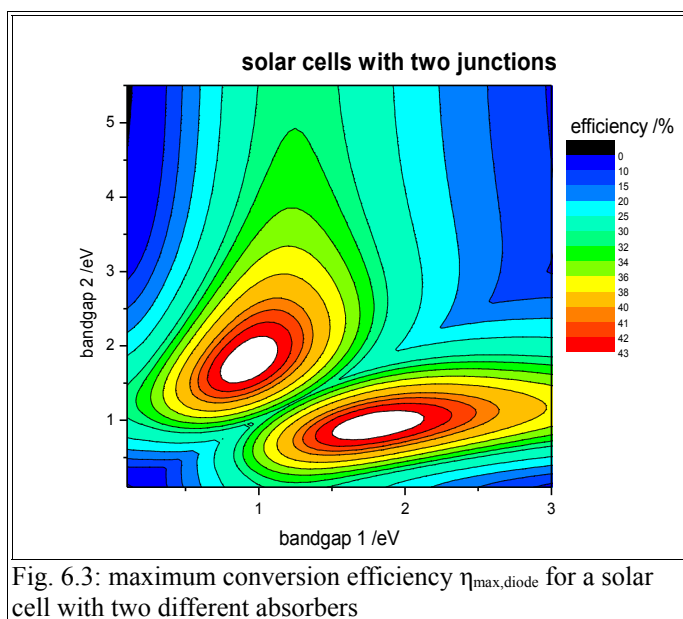
6.2 Transient photovoltage measurements

6.2.1 Experimental setup

An apparatus was built up within this PhD-thesis to measure photovoltage transients of dye sensitized solar cells (DSSCs) and nano surface conductivity solar cells (NSCSCs). The cells were illuminated with an array of LEDs of different color. The current, which flows through the LED-array, is controlled by a solid state switch. In the bias mode, the current and thus the light intensity is constant. If the solid state switch receives a pulse signal from a pulse generator, the current/light intensity increases for a time period between 50 ns - 5 s. The LED, which is used for the bias illumination and the pulse, can but must not be the same. The photovoltage of the DSSC/NSCSC is measured as a function of time with a storage oscilloscope. A sketch of the apparatus is given in Fig. 6.4.
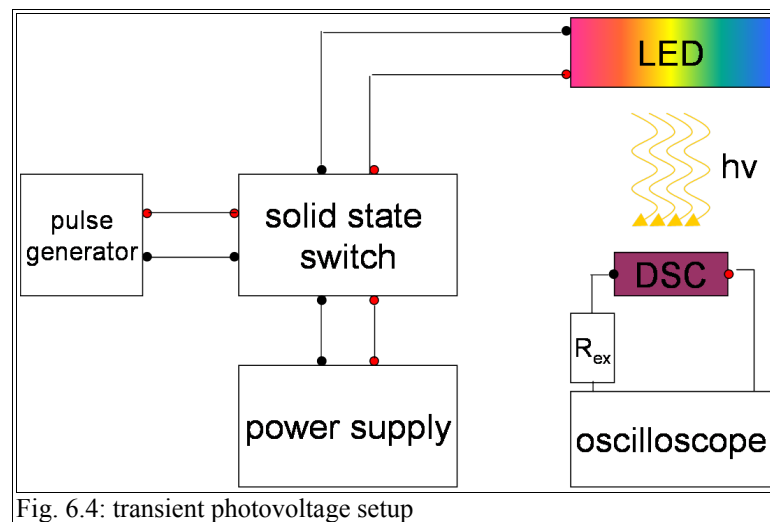

Fig. 6.4: transient photovoltage setup

The pulse generator was a TGP110 from TTi. The pulse length could be varied between 50 ns and 5 s, the amplitude between 0.1 V and 10 V and the repetition rate between 0.1 Hz and 10 Mhz. The shape of the pulse was rectangular in all experiments.

The storage oscilloscope was a USB Scope 1 Mephisto UM 202 from Meilhaus Elektronik. Two channels were available, of which one was used to monitor the current flowing through the LED-

array and one to monitor the photovoltage response of the dye sensitized solar cell. The maximum resolution was 16 bit for an input voltage between ± 100 mV and ± 10 V. The internal memory was 256 kS.

The LEDs were from Luxeon. For most experiments ring modules with 6 LEDs were used and for the rest single "star light" LEDs. Details about the LED specifications are given in chapter 6.2.2.

The solid state switch was made at the Hahn-Meitner institute by Dr. Janata and had the layout given in Fig. 6.5.
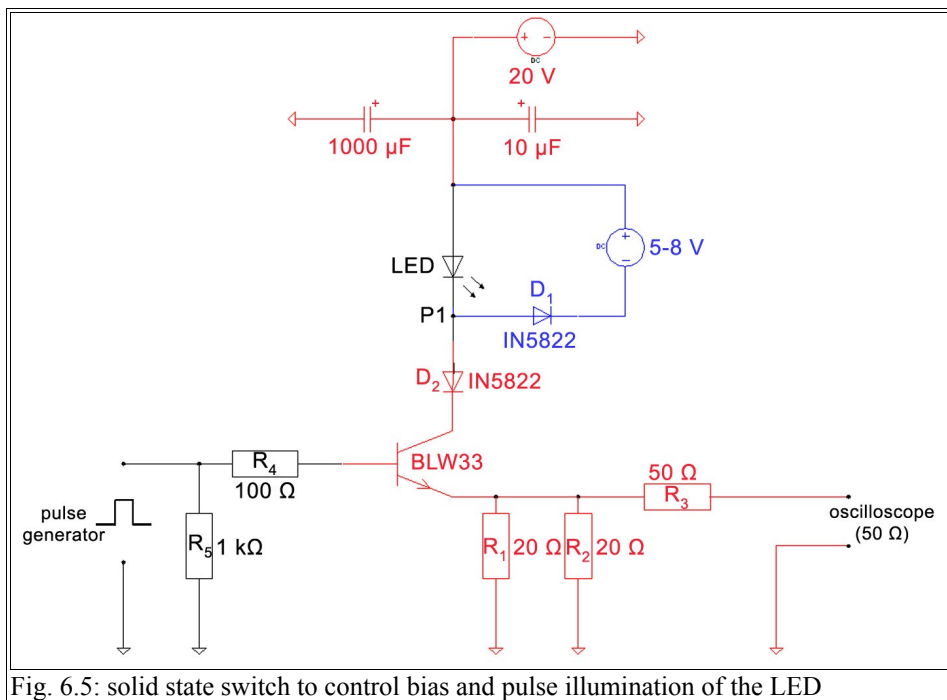

Fig. 6.5: solid state switch to control bias and pulse illumination of the LED

Two power supplies were used to drive the solid state switch, which are labeled blue and red in Fig. 6.5. The blue one was used for the bias illumination of the LED, the red one for the pulse illumination. As long as the transistor BWL33 is locked, the current flows through electric circuit 1 (labeled blue). If a pulse is given by the pulse generator, the transistor switches and the current flows through electric circuit 2 (labeled red) only. This is because at the same time, the potential at point P1 drops and diode D_1 behaves like an insulator. Thus electric circuit 1 is locked.

The transistor has two emitters to lower the inductance of the transistor. The 50 Ω parallel resistor at the oscilloscope was found to reduce the noise of the transient signal significantly.

6.2.2 Calibration measurements

In order to measure the number of photons that hit the solar cell per flash, two different approaches were identified and will be discussed in this chapter.

–   Indirectly the photon flux can be determined by measuring the current I_{diode}, which flows through the LED. The underlying assumption is, that I_{diode} is proportional to the photon flux.

–   Directly, the photon flux can be determined by measuring the photocurrent of a photodiode with a known spectral response.

In the circuitry of the solid state switch shown in Fig. 6.5, it can be seen that the current I_{diode} flows over a resistance of $R1 = 2.5\,\Omega$. The resulting potential drop V can be monitored with an oscilloscope, so I_{diode} can be determined by Ohm's law.

$$I_{diode} = \frac{V}{R1} \quad (6.9)$$

By integrating over the pulse length t_{pulse} the total charge per flash Q_{diode} is accessible. To determine the number of photons per flash n_{ph}, the conversion efficiency of the LED η_{LED} has to be known, which depends on the junction temperature T_j and forward current I_{diode}.

$$n_{ph} = \eta_{LED} * Q_{diode} = \eta_{LED}(T_j, I_{diode}) * \int^{t_{pulse}} I_{diode}\, dt \quad (6.10)$$
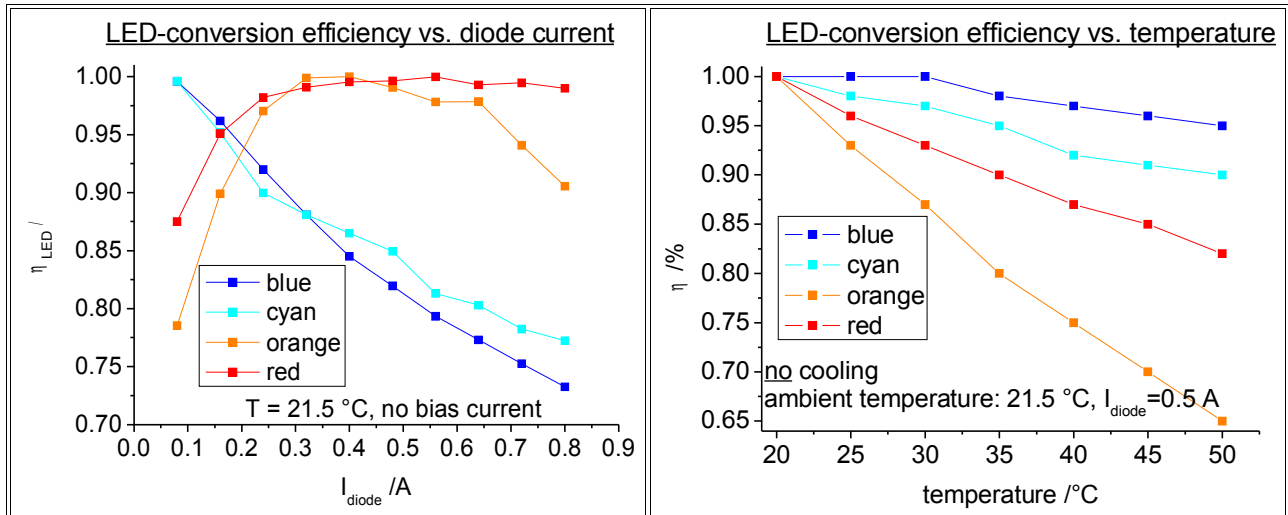
Fig. 6.6: relative LED-conversion efficiency.
a) as a function of the diode current I_{diode}
b) as a function of the junction temperature T_j

Calibration measurements for LEDs with a maximum photon flux at 470 (blue), 505 (cyan), 590 (orange) and 627 nm (red) were done and η_{LED} as a function of junction temperature and forward current I_{diode} is depicted in Fig. 6.6. It is assumed the photon flux I_{ph} is proportional to the current of the photo diode I_{diode} at any time.

It can be seen that η_{LED} decreases with increasing temperature. The temperature coefficients are -0.16 %/K (blue), -0.33 %/K (cyan), -1.17 %/K (orange) and -0.6 %/K (red) respectively.

The junction temperature T_j is a function of the bias current I_{bias} and it was tried to calibrate each LED by taking calibration curves $T_j(I_{bias})$. However, it was found that the equilibration time before $T_j = T_{ambient\ atmosphere}$ takes up to 30 min at $I_{bias} \approx 100$ mA and the temperature T_j at a given current I_{bias} various up to 10 % if the device is not cooled. By employing a fan the equilibration time decreased by one order of magnitude and $T_j(I_{bias})$ could be measured with high reproducibility (Fig. 6.7).

For the blue and cyan LED, the decrease of the conversion efficiency η_{LED} due to heating was negligible. Even at a high bias current it was less than 5 %. However, for the red and the orange LED, η_{LED} decreases by up to 20 % due to heating and needs to be taken into account.

η_{LED} strongly depends on the diode current I_{diode} (Fig. 6.6a). For the blue and cyan LED, a linear decrease of η_{LED} with increasing I_{diode} was found. For the red and orange LED the correlation is more complicated and cannot be described with a simple function. Furthermore the measurement error at low I_{diode} increased significantly. In order to keep the calibration simple, it was decided to use only pulses with a current 0.25 A $< I_{diode} < 0.65$ A for transient measurements. In this region, η_{LED} is

constant for the red and orange LED and has a well defined slope for the blue and cyan LED.
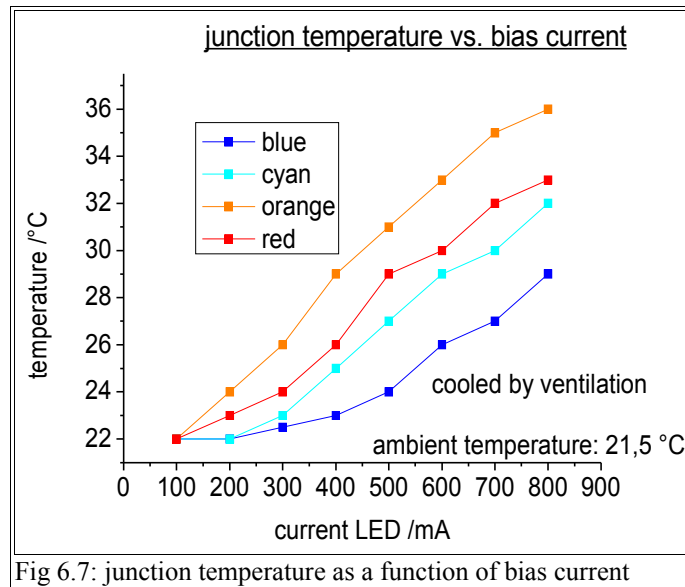

Fig 6.7: junction temperature as a function of bias current

Another way to vary the number of photons per flash is to change the pulse length. As can be seen in Fig. 6.8, the conversion efficiency η_{LED} is constant for a pulse length between 10 µs < t_{pulse} < 1 ms. 10 µs was the time resolution of the oscilloscope and for t_{pulse} >1 ms the shape of the pulse signal was not rectangular anymore. Most experiments were done between 20 µs - 200 µs, for which a constant conversion efficiency η_{LED} can be assumed.
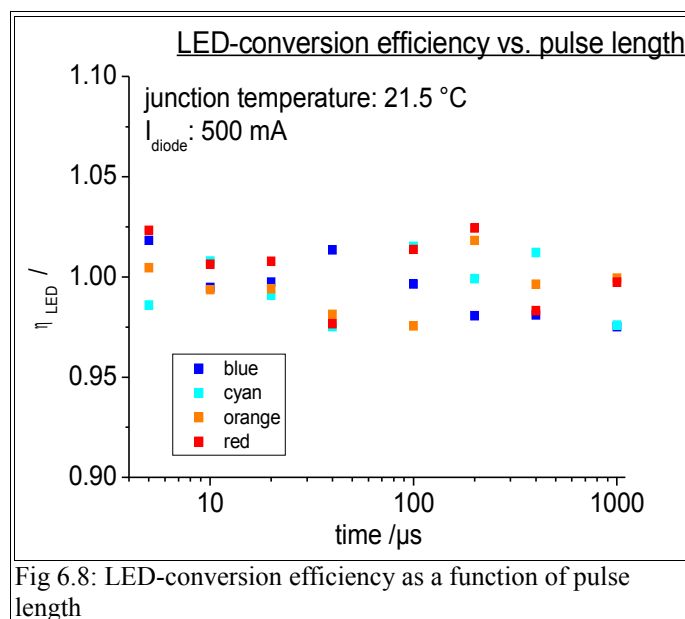

Fig 6.8: LED-conversion efficiency as a function of pulse length

The advantages and disadvantages of taking the LED-current as a measure for the number of photons n_{ph} are summarized in table 6.1.

advantages	disadvantages
I_{diode} is measured automatically with each transient	no absolute measurement
the relative change of η_{LED} is known for different temperatures and for different I_{diode}	measurement is afflicted with an error of up to 10 %

Table 6.1: calculating the number of photons n_{ph} with the diode current I_{diode}

Measuring the photocurrent of a photodiode with a know spectral response is an absolute measurement that gives the photon flux I_{ph} in photons/cm^{2}s^{-1}. The incident photon to current conversion efficiency (IPCE) as a function of wavelength is shown in Fig. 6.9 and the spectrum of the LEDs was taken from the manufacturers data sheet (Luxeon Ring Technical Data DS22). The exact area of the photodiode was measured with the SMSC imaging technique and was determined to be 0.041 cm^{-2}.
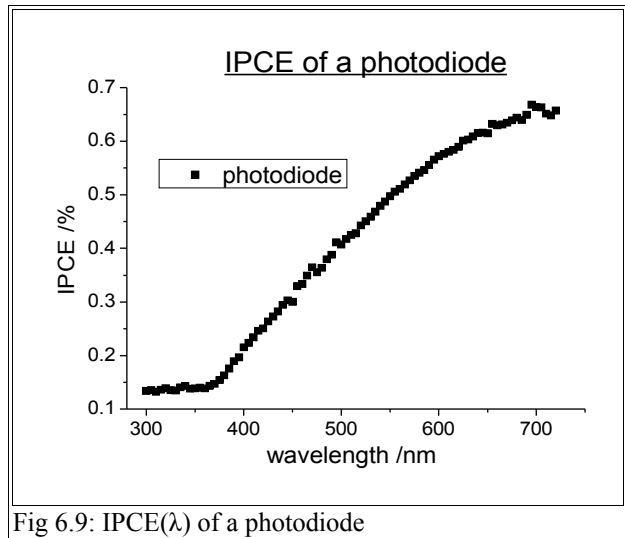
Fig 6.9: IPCE(λ) of a photodiode

With equation 6.11, the photon flux can be calculated as a function of the photo diode current.

$$I_{ph} = \int_0^\infty \frac{I(\lambda)}{IPCE(\lambda)} d\lambda \qquad (6.11)$$

For a typical flash with a pulse length of ca. 100 μs and medium pulse amplitude, the photon flux is about 10^{17} photons/cm^{2}s^{-1}. This corresponds to ca. 100 % of the AM1.5 spectrum (integrated from $0 < \lambda < 640$ nm).

For most transients an absolute measurement of the photon flux I_{ph} was done with the photodiode at the beginning of the measurement and assigned to the diode current I_{diode}. Then the diode current and the relative changes in the conversion efficiency η_{LED} of the diode were used to calculate I_{ph} for all following transients.

6.3 Transport kinetics within nanoporous TiO$_2$ electrodes

Charge transport within dye sensitized solar cells have been extensively studied in the past [149][159][160][146][161][162]. Especially the electron transport in the TiO$_2$-network is subject to an ongoing debate since the kinetics are found to depend on various parameters and reproducibility is typically poor. From a theoretic point of view, the multiple trapping model is today the most accepted mechanism for electron transport in the literature [15][160].

Briefly the transport kinetics depend on the density of trap states (DOS) at a given photovoltage, the charge transfer resistance at the TiO$_2$/FTO interface, the electrolyte composition and the position of the TiO$_2$-conduction band. In this chapter it is tried to quantify the most important parameters that influence the transport kinetics by photovoltage/photocurrent measurements and to develop a diffusion based model. The model simulates the photovoltage/photocurrent as a function of time for cells that are illuminated with a constant bias light and excited with a short light pulse of a few microsecond.

Besides a better understanding of the standard DSSC, the model was found to be very useful to explain degradation phenomena in liquid DSSC (chapter 6.5) and current limitation in Nano Surface Conductivity Solar Cell (chapter 6.4).

Chapter 6.3.1 gives the theoretical background of the model. The continuum equation is introduced and the parameters needed to model the electron transport in the nanoporous semiconductor are identified. It is demonstrated that the electron transport can be treated independently from the hole transport in standard DSSC. Special cases (e.g. measurements at V$_{OC}$) are discussed and if possible analytical solutions to the continuum equation are given. Chapter 6.3.3-6.3.8 give the input parameters of the model. It should be noted that all parameters used in this model can be measured directly and no adjustable parameters are needed. Chapter 6.3.9 discusses the predictions of the model and experimental evidence for the predictions is given. Finally chapter 6.3.10 presents photovoltage measurements under various conditions that are simulated with the model. In order to focus on the model and not to distract the reader, mainly one cell type was used to test the model. The parameters given in chapter 6.3.3-6.3.8 refer to this specific cell composition and were found to be about the same for different cells of the same type. The composition was as follow: A standard DSSC with liquid electrolyte (0.6 M PMII, 0.5 M TBP, 0.1 M I$_2$ in acetonitrile) according to the procedure described in chapter 5.

6.3.1 Development of a transport model for nanoporous semiconductor electrodes

The following model was developed to understand transient photovoltage/photocurrent decay in dye sensitized solar cells with TiO_2 as the nanoporous semiconductor, but in principal it can be applied to other semiconductors as well. So far transient measurements have been mainly done at open circuit potential [14][163][164] or at short circuit potential [135] and the parameters investigated were in most often the extracted charge (at I_{SC}) and the recombination rate (at V_{OC}). Photovoltage transient measurements at V_{OC} have the advantage that the externally measured potential equals more or less the Fermi potential within the film. If the charge generation of the light pulse is furthermore uniform in the film (weak absorption), the description of the system greatly simplifies and the transient basically reflects the first order electron recombination with the electrolyte. However, this is not sufficient to determine the extraction probability of electrons at other points of the I-V-curve and tools to characterize the cell especially at the maximum power point are warranted. In the following chapter a model is developed, which can characterize the cell at any point of the I-V-curve. It is an one dimensional model that treats the nanoporous TiO_2 as a pseudo-homogeneous medium. Under steady state condition (only bias illumination, no light pulse), the model can be used to model I-V-curves.

Generally, the continuum equation for any solar cell includes the generation of charge carriers G(x), the recombination rate R(x) and the flux of holes $J_p(x)$ and electrons $J_n(x)$. The driving force for the transport of holes and electrons is due to diffusion with an effective diffusion coefficient D_n (electrons) and D_p (holes) and due to migration in the electric field E(x) with a mobility μ_n (electrons) and μ_p (holes). The Poisson equation relates the spatial derivative of the electric field to the concentration of mobile charges carriers n(x), p(x) and fixed charge carriers N_D, N_A (donors and acceptors).

This results in a system of four differential equations:

$$\frac{\delta J_n(x)}{\delta x} = \frac{-\delta J_p(x)}{\delta x} = R(x) - G(x) \quad (6.12)$$

$$J_n(x) = \mu_n n(x) E(x) + D_n \frac{\delta n(x)}{\delta x} \quad (6.13)$$

$$J_p(x) = \mu_p \, p(x) E(x) - D_p \frac{\delta \, p(x)}{\delta \, x} \quad (6.14)$$

$$\frac{\delta \, E(x)}{\delta \, x} = \frac{1}{\epsilon_{TiO2}} * (N_D(x) - N_A(x) + p(x) - n(x)) \quad (6.15)$$

For nanoporous DSSC some simplifications can be introduced:

1) E(x) = 0

   The most important assumption made in the model is that no electric field is present in the nanoparticles because the Debye length is typically much smaller than the particle diameter of the TiO$_2$. The Debye length gives the distance, after which the electric field of a charge decayed to e^{-1} due to the shielding effect of other charge carriers with opposite polarity. It is in the order of 0.1 nm for electrons in liquid dye sensitized solar cells, whereas the particle diameter is about 25 nm. Thus no macroscopic electric field can build up in the TiO$_2$ and the charge transport is believed to be only due to diffusion [165].

2) Ambipolar diffusion

   Since the positive cations in the electrolyte cannot intercalate into the TiO$_2$-lattice (except Li$^+$ to some extent), the motion of electrons in the TiO$_2$-nanoparticles create a charge imbalance. The resulting electric field drags the cations along with the electrons. This mechanism is called ambipolar diffusion. The effective diffusion coefficient is determined both by the diffusion coefficient of the positive and negative charge carriers and is given by (taken from [166])

$$D_{amb} = \frac{n+p}{\dfrac{n}{D_n} + \dfrac{p}{D_p}} \quad (6.16)$$

where n is the concentration of negative charge carriers, p of the positive charge carriers and D_n and D_p the respective diffusion coefficients. n is in the range of $5*10^{18}\,cm^{-3}$ at 1 sun bias illumination and, assuming a 0.6 M LiI electrolyte, p is $3*10^{20}\,cm^{-3}$. In this case the diffusion coefficient D_n is about 10 % higher than the measured ambipolar diffusion coefficient D_{amb}. At lower light intensities n decreases exponentially and thus $n \ll p$. In this case

equation 6.16 simplifies and $D_{amb} = D_n$.

3) Hole transport limitation

The hole concentration p in equation 6.16 includes all cations in the electrolyte. However, the hole transport from the dye cation to the counter electrode is done only by the triiodide ions I_3^-. Thus the electron transport might also be slowed down by an insufficient triiodide transport in the electrolyte (both in the nanoporous TiO_2 and the bulk electrolyte [159][154]). The diffusion coefficient for triiodide is about $8.5*10^{-6}$ cm^2s^{-1} [167] (in acetonitrile) whereas the diffusion coefficient for electrons is about two times higher ($1.5*10^{-5}$ cm^2s^{-1} [149]). At the same time the electron concentration at 1 sun is about ten times smaller than the triiodide concentration assuming an electron concentration of $5*10^{18}$ cm^{-3} and a 0.1 M I_3^--solution. As a conclusion the overall charge transport in the cell is rather limited by the electron transport in the TiO_2 than by the hole transport in the electrolyte.

Together with the information about the ambipolar diffusion coefficient it is asssumed that the electron transport can be modeled independently from the hole transport.

With these assumptions equation 6.12 - 6.15 simplify to

$$\frac{\delta J_n(x)}{\delta x} = D_n \frac{\delta^2 n(x)}{\delta x^2} = R(x) - G(x) \quad (6.17)$$

Under non-stationary conditions and with a slightly different notation, the time dependent continuum equation becomes

$$\frac{\delta c(x,t)}{\delta t} = k_g - k_{rec} * c(x,t) + D_{eff} \frac{\delta^2 c(x,t)}{\delta x^2} \quad (6.18)$$

where k_g [$Qcm^{-3}s^{-1}$] is the generation of electrons in the nanoporous TiO_2 film, k_{rec} [s^{-1}] is the recombination rate of conduction band electrons with the electrolyte, D_{eff} [cm^2s^{-1}] is the effective diffusion coefficient of electrons in the TiO_2 film and c(x,t) [Qcm^{-3}] is the concentration of electrons as a function of time and space. Equation assumes that the only driving force for electrons to move within the film is diffusion (kinetic model) that can be described with Fick's law and that electrons recombine with first order kinetics. The derivative with respect to time consists of three parts, the

first one describing the electron generation, the second one accounts for the electron recombination and the third one for the diffusion within the TiO$_2$-layer. This second order differential equation needs three boundary conditions, two in space (equation 6.19, 6.20) and one in time (equation 6.21).

$$\frac{\delta c(0,t)}{\delta x} = I_{ex} \quad (6.19)$$

$$\frac{\delta c(d,t)}{\delta x} = 0 \quad (6.20)$$

$$c(x,0) = c_0 \quad (6.21)$$

Equation 6.19, where I_{ex} [mAcm^{-2}] is the current flowing through the external circuit, says that the chemical potential of the electrons in the film (which is proportional to the concentration gradient) is converted to an electric potential at the front contact. The resulting potential difference drops over some external resistance R_{ex} with a current I_{ex}. Equation 6.20, where d [cm] is the thickness of the TiO$_2$ electrode, says that no electrons flow through the TiO$_2$/electrolyte interface. It is noted that this model treats only the electron transport and not the hole transport in the electrolyte. The hole transport at the TiO$_2$/electrolyte interface equals I_{ex}, thus charge neutrality within the layer is given at any time. Finally equation 6.21 states that the initial electron distribution $c_0(x)$ [Qcm^{-3}] has to be given.

From a descriptive point of view the following processes determine the photovoltage:

The constant bias illumination injects electrons into the conduction band of the TiO$_2$ with a rate k_g, which then recombine with a rate $k_{rec}*c(x,t)$. At some time t_{eq}, a steady state is reached and $c(x,t)$ does not change over time anymore.

If a light pulse of a few microseconds is triggered additional electrons are injected into the TiO$_2$. The equilibrium is disturbed and the photovoltage increases. The absorption of light within the TiO$_2$-layer will basically follow Lambert-Beers law, so immediately after the pulse was triggered the electron distribution will decrease exponentially with the distance from the front contact. Then the electrons start to recombine or diffuse along the concentration gradient into the film. Both effects will decrease the measured potential. Indeed it was observed in all measurements at V_{OC}, that a single exponential decay as it would be expected if only recombination contributed to the voltage decay, cannot explain the voltage decay in the first 100 μs-10 ms. Only after the electron density has

equilibrated across the whole film the decay is single exponential.

The electron concentration and thus the Fermi level within the TiO_2 layer is a function of the distance from the front contact. The TiO_2 film is divided into n slices, each being a capacitor with a photovoltage $V_{ph,n}$. At the front electrode (n = 0) electrons are transfered to the $F:SnO_2$ (FTO) over a transfer resistance R_{trans}. The FTO itself is also a capacitor with a capacitance C_{FTO} and any potential difference between the FTO and TiO_2 equilibrates with a time constant $R_{trans}*C_{FTO}$ since C_{FTO} is typically two order of magnitude smaller than C_{TiO2}.

The only recombination pathway for injected electrons is assumed to be the reaction between conduction band electrons and triiodide.

$$e^-_{TiO2(CB)} + \frac{1}{2} I_3^- \xrightarrow{k_{rec}} \frac{3}{2} I^- \quad (6.22)$$
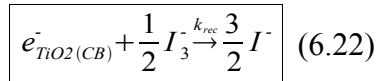
Since the concentration of I_3^- is constant in all experiments it is combined with the overall recombination rate constant. Thus the resulting constant k_{rec} is of first order in electron density with the unit s^{-1}.

One might conclude from reaction 6.22 that a cell without any triiodide should be very efficient since no recombination occurs. However, in that case the overall charge transport would be limited by the hole transport in the electrolyte and one of the main assumption of the model is no longer fulfilled.
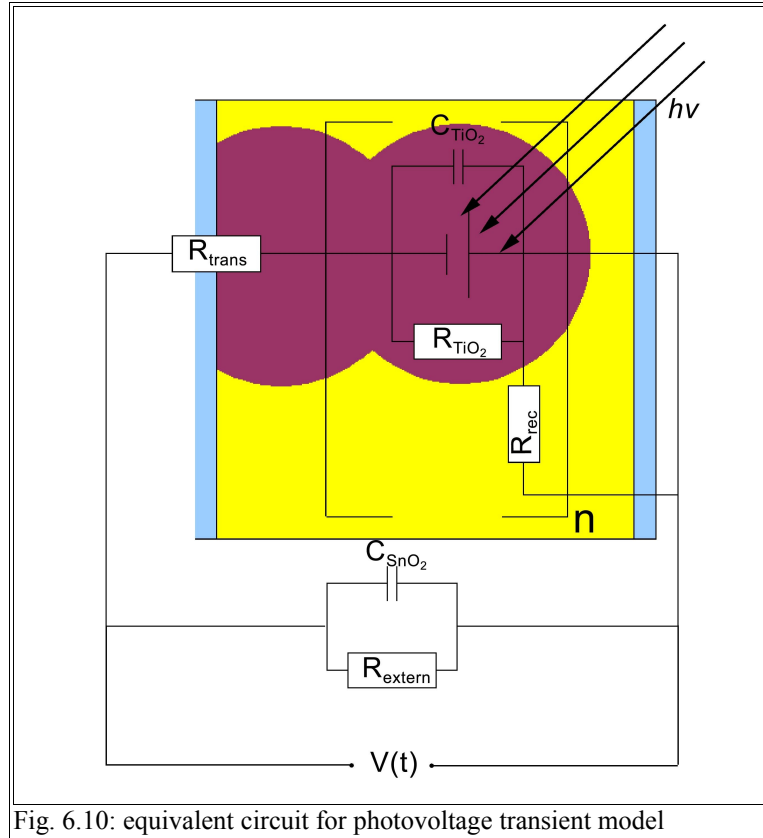
Fig. 6.10: equivalent circuit for photovoltage transient model

Fig. 6.10 shows an equivalent circuit for the model taken from [168]. The externally measured potential V(t) is recorded with an oscilloscope. It results from the charging of the FTO electrode and equals as a first approximation the capacitance of the potential of the FTO electrode. The time τ_{rise} that is needed such that

$$V(t) = \Delta V * (1 - e^{-1}) \quad (6.23)$$

V(t) = measured potential /V; ΔV = potential difference between FTO-capacitor and adjacent TiO$_2$-capacitor /V

will be mostly determined by the capacitance of the FTO and is

$$\tau_{rise} = C_{SnO2} * R_{trans} \quad (6.24)$$

τ_{rise} = risetime /s; C_{SnO2} = capacitance of FTO /Fcm^{-2}; R_{trans} = transer resistance /Ω;

After equilibration such that $V_{FTO} = V_{TIO2}$, the measured potential decreases due to electron recombination and electron diffusion along the concentration gradient. Electron transport within the TiO$_2$ layer is described by the well known trapping/detrapping mechanism [15]. To model the transport rates within the TiO$_2$ layer, an effective diffusion coefficient of electrons D_{eff} is introduced and the flux is described by Fick's law. The effective diffusion coefficient has been an extremely successful concept, however, the interpretation of D_{eff} is not straightforward and strongly depends on the nature of TiO$_2$-particles and to some extend on the electrolyte composition. Compared to a

diffusion coefficient of $10^{-1}\,cm^2s^{-1}$ in single crystalline TiO_2 [169], it is between 2-6 order of magnitude smaller in nanoporous systems. Mainly three factors contribute.

1) trapping/deptrapping

   At normal cell operation (light intensity < 1 sun), all electrons are trapped in localized states below the conduction band and electron movement requires thermal activation to the conduction band edge. Thus the trap state distribution and the position of the TiO_2 conduction band have a great influence on electron transport.

2) film morphology

   each particles/particle interface represents a diffusion barrier for electrons. The coordination number and the interface area have a strong influence on the barrier height and thus on the diffusion coefficient. The coordination number strongly depends on the film porosity and varies between 5 (50 %) and 2.5 (75 %) [170], which was shown to have a significant effect on D_{eff}. The interface area mainly depends on the annealing temperature and increases significantly for sintered films.

3) ambipolar diffusion

   As explained in the beginning of this chapter, the diffusion in nanoporous TiO_2 is believed to be ambipolar. Depending on the concentration of the electrolyte and the light intensity, the effective diffusion coefficient of the electrons might be affected by electrolyte composition.

As a consequence differences of the effective diffusion coefficient D_{eff} might be related to several parameters and comparisons between different experiments are difficult.

No macroscopic electric field is present in the TiO_2 particles since the particle dimensions are too small. There are some indications that the charging of the TiO_2 particles might induce an electric field gradient in the film that adds to the chemical potential gradient [171]. However, this is difficult to prove experimentally since the electron transport still obeys Fick's Law and can be described with a single diffusion coefficient. For this reason it is assumed that diffusion is the only driving force for electron motion in the film.

6.3.2 Parameters for the transport model

Equation 6.17 describes the electron concentration within the TiO$_2$ film as a function of time and place, which is not directly measurable with the transient photovoltage technique. An equation to relate the measured potential of the FTO-substrate V$_{FTO}$(t) to the electron concentration c(x = 0,t) is needed, which is

$$V_{FTO}(t) = \frac{c(x=0,t)}{C_{TiO2}} - I_{trans} * R_{trans} * A_{TiO2}$$ (6.25),

C$_{TiO2}$ = capacitance of TiO$_2$ /Fcm^{-2}d^{-1}; R$_{trans}$ = transfer resistance /Ω; I$_{trans}$ = current flowing through the FTO/TiO$_2$ interface /mAcm^{-2}; A$_{TiO2}$ = area of TiO$_2$ /cm^2

The transfer current I$_{trans}$ that flows through the TiO$_2$/FTO interface has a capacitive I$_{C,FTO}$ part, which charges the FTO-capacitor and an ohmic part I$_{ex}$ that can be directly measured in the external electric circuit. Thus I$_{trans}$ can be expressed as

$$I_{trans} = I_{ex} + I_{C,FTO} = I_{ex} + \left(\frac{C_{FTO} * \delta V_{FTO}}{\delta dt}\right)$$ (6.26)

At the same time V$_{FTO}$ is the externally measured voltage, so the external current I$_{ex}$ can be expressed as

$$I_{ex} = \frac{V_{FTO}}{R_{ex}}$$ (6.27)

The generation rate k$_g$ in the continuum equation 6.17 is the sum of the bias illumination k$_{g,bias}$ and the pulsed light k$_{g,pulse}$.

$$k_g = k_{g,bias} + k_{g,pulse}$$ (6.28)

the bias illumination k$_{g,bias}$ is accessible at short circuit condition, where a nearly quantitative charge extraction is predicted by the model.

$$k_{g,bias} = \eta_g * \frac{I_{ex}(V=0)}{d}$$ (6.29)

The charge generation efficiency η_g comprises all loss mechanisms that are not measured with the transient technique, namely that an absorbed photon does not cause an electron injection, the electron recombination from a conduction band electron with the oxidized dye and all other loss mechanisms on a time scale much shorter than the time resolution of the oscilloscope (<1 µs). η_g is assumed to be constant and can be determined according to the procedure explained in chapter 6.2.2.

As mentioned above the light absorption and the generation rate k_g obeys Lambert Beers Law. Space-resolved, $k_g(x)$ decreases exponentially within the film, so

$$k_g * A * \int_0^d e^{-\alpha * x} dx = k_g \Leftrightarrow A * \int_0^d e^{-\alpha * x} dx = 1 \quad (6.30)$$

Solving 6.27 for A and using 6.26 gives

$$k_g(x) = (k_{g,bias} + k_{g,pulse}) * \frac{\alpha}{1 - e^{-\alpha d}} * e^{-\alpha x} \quad (6.31)$$

Inserting equation 6.25 in the continuum equation 6.17 gives

$$\frac{\delta c(x,t)}{\delta t} = (k_{g,bias} + k_{g,pulse}) * \frac{\alpha}{1 - e^{-\alpha d}} * e^{-\alpha x} - k_{rec} * c(x,t) + D_{eff} \frac{\delta^2 c(x,t)}{\delta x^2} \quad (6.32)$$

Equations 6.24-6.23 contain eleven parameters, which are needed for the model:

1) A_{TiO2}: the area of the TiO$_2$ electrode in [cm^2]. For most experiments A_{TiO2} was 1 cm^2

2) d: the thickness of the TiO$_2$ electrode in [µm], which is measured with a profilometer. For most experiment, d was 9.5 µm.

3) R_{ex} [Ω]: the resistance of the external electric circuit, over which the measured cell voltage drops

4) V_{FTO} (t) [V]: the potential of the FTO front contact as a function of time. It is the externally measured cell voltage, monitored with an oscilloscope

5) α []: the absorption coefficient, determined by measuring the absorption of the layer in an integrating sphere. In this study, LEDs with four different dominant wavelengths were used. The corresponding absorbance of the TiO_2 electrode (thickness 10 μm) is given in table 6.2

color	dominant wavelength	spectral half width	absorbance A_λ
blue	470 nm	25 nm	2.2
cyan	505 nm	30 nm	2
orange	590 nm	14 nm	1
red	627 nm	20 nm	0.6

Table 6.2: absorbance of a 10 μm thick TiO_2-layer for different LEDs

6) k_{rec} [s^{-1}]: the recombination rate constant as a function of bias photovoltage is measured from photovoltage decay measurement at different light intensities. Details are given in chapter 6.3.3.

7) R_{trans} [Ω]: the resistance of the TiO_2/FTO interface as a function of bias photovoltage is derived from the rise of photovoltage transients at open circuit potential. Details are given in chapter 6.3.6.

8) D_{eff} [cm^2s^{-1}]: the effective diffusion coefficient of electrons in the TiO_2 layer as a function of photovoltage. It is derived from equilibration kinetics of electrons in the film. Details are given in chapter 6.3.7.

9) $k_{g,pulse}$ [$Qcm^{-3}s^{-1}$]: The generation rate of electrons of an additional light pulse. In principal $k_{g,pulse}$ can be calculated by integrating the extracted charge of the pulse and divide it by the pulse length t_{pulse}:

$$k_{g,pulse} = \frac{Q_{ex}}{t_{pulse}} = \eta_g * \frac{\int_0^\infty (I_{ex} - I_{bias})}{t_{pulse}} \quad (6.33)$$

where I_{bias} is the current from the bias illumination. However, in contrast to the bias light, the charge extraction efficiency η_g of the pulse is not constant and depends on the photovoltage as will be shown in chapter 6.3.5. For this reason a calibration curve is recorded first and than equation 6.18 is used to calculate $k_{g,pulse}$.

10) C_{FTO} [Fcm^{-2}]: the capacitance of the FTO electrode. It is calculated from derivative of the photovoltage transient signal with respect to time when the cell is switched from a load resistance R_{ex} to open circuit and the illumination is stopped at the same time. Details are given in chapter 6.3.4.

11) The chemical capacitance of the titaniumdioxide C_{TiO2}: It is defined as the number of electrons per volt that can be stored in bulk or surface trap states of the nanoporous TiO$_2$. It relates the potential V_{TiO2} to the total charge Q_{TiO2} within the film.

$$\boxed{V(t)=C_{TiO2}*Q_{TiO2}} \quad (6.34)$$

V_{TiO2}= potential of the TiO$_2$ at the TiO$_2$/FTO interface /V; Q_{tiO2}= total charge within the TiO$_2$ film /Qcm^{-2}d^{-1} ; C_{TiO2} = capacitance of TiO$_2$ electrode /Fcm^{-2}d^{-1}

Typically the unit of the capacitance is Fcm^{-2}, however, it should be noted that the chemical capacitance C_{TiO2} depends on the film thickness d, thus C_{TiO2} is given in Fcm^{-2}d^{-1}. C_{TiO2} typically increases exponentially with the potential V_{TiO2}, so in order to run the model with some potential gradient in the film, the function $C_{TiO2}(V_{TiO2})$ needs to be known. The measurement procedure is given in chapter 6.3.5.

In the literature a more common way to describe the trap state distribution is the density of trap states DOS, which can be expressed as

$$\boxed{DOS=\frac{C_{TiO2}}{e*d*(1-p)}} \quad (6.35)$$

DOS = density of trap states /cm^{-3}; C_{TiO2}= capacitance /Fcm^{-2}d^{-1}; e = elementary charge /C; d = thickness of layer /μm; p = porosity of layer /

The porosity p of the nanoporous TiO$_2$ film was typically 60 % in this study. It was measured by weighing a TiO$_2$ layer with known thickness and area.
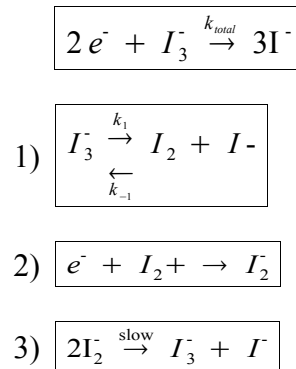
$$\boxed{p=\frac{m_{TiO2}}{A_{TiO2}*d*\rho}} \quad (6.36)$$

m_{TiO2}=mass of sample /g; A_{TiO2} = area of sample; d = thickness of sample /cm; ρ = density of TiO$_2$ = 4.2 gcm^{-3}

6.3.3 The recombination rate k_{rec}

The exact mechanism for the electron recombination with the electrolyte is still under debate. The most accepted mechanism includes, according to [172], the following steps:

total net reaction:

$$2\,e^- + I_3^- \xrightarrow{k_{total}} 3I^-$$

1) $$I_3^- \underset{k_{-1}}{\overset{k_1}{\underset{\longleftarrow}{\rightarrow}}} I_2 + I-$$

2) $$e^- + I_2+ \rightarrow I_2^-$$

3) $$2I_2^- \xrightarrow{slow} I_3^- + I^-$$

The rate determining step is the disproportionation of I_2^- (3), which implies that the over all net reaction is of second order in triiodide concentration and of first order in the electron concentration. To simplify the analysis the triiodide concentration is kept constant in all experiments and is combined with the overall rate constant k_{total}, so that the resulting constant k_{rec} has the unit s^{-1} and describes the electron recombination with a first order kinetic with respect to the electron concentration.

The recombination constant k_{rec} was determined by photovoltage decay measurements at open circuit potential. The transients were fit with a single exponential decay. The recombination rate k_{rec} is inverse proportional to the decay time τ_{rec}. As can be seen in Fig. 6.12, k_{rec} depended strongly on the photovoltage, so it was important to keep the perturbation for each individual measurement small, since k_{rec} was assumed to be constant for each transient. Typically the pulse was adjusted so that the peak of the transient was between 3-5 mV above the open circuit potential.
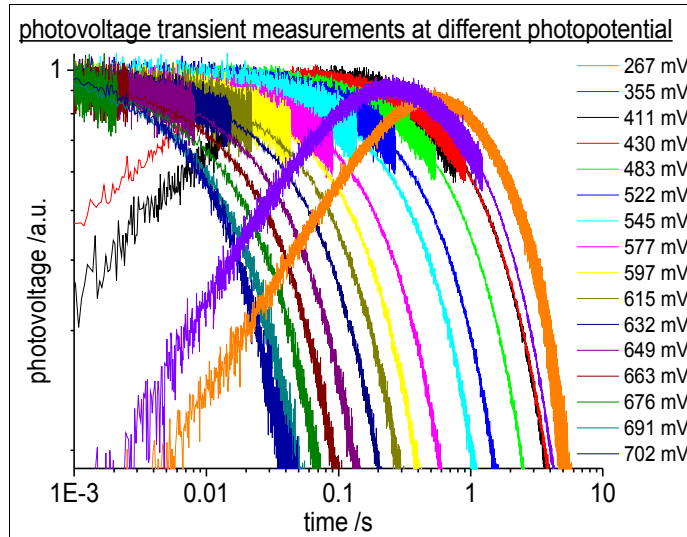
Fig. 6.11: photovoltage transient measurements: excitation wavelength: 627 nm, pulse length: 100 μs; peak pulse: 3-5 mV

Another assumption was that the charge generation of the pulse is constant throughout the film. Otherwise the electrons diffuse into the film and recombine at the same time and both processes lower the photovoltage at the FTO front contact (chapter 6.3.7). For this reason red light with a low absorption coefficient was used (absorbance $A_\lambda = 0.6$) and the cell was illuminated both from the front and back side.

For measurements at very low photovoltage, the transients were RC-limited. This can be seen in Fig. 6.11 for $V \leq 430$ mV. In this case the photovoltage decay was extrapolated to $t = 0$. Fig. 6.11 gives a normalized overview about all measurements in a double logarithmic plot. One can see that the decay time τ_{rec} varies over several orders of magnitude. The corresponding recombination rate constants as a function of photovoltage are given in Fig. 6.12.

As a first approximation the measured photovoltage eV can be interpreted as the chemical potential μ_{el} of the electrons in the TiO$_2$ film.

$$e * V - \mu_{el,0} = \mu_{el} \quad (6.37)$$

where $\mu_{el,0}$ is a constant offset and e the elementary charge. With increasing chemical potential more electrons can provide the activation energy that is needed for the reduction of iodine and thus the rate constant increases. In this interpretation the photovoltage eV represents the kT term of the Arrhenius equation and by plotting k_{rec} against eV^{-1} the activation energy can be extracted. As can be

seen Fig. 6.12b two branches are visible in the Arrhenius plot representing two different recombination mechanisms.

The first one is dominant for V > 550 mV with an activation energy of 990 KJmol^{-1} and a high preexponential factor of $1.4*10^8$s^{-1}. The second one is dominant for V < 450 mV with a much lower activation energy of 36.5 KJmol^{-1}, but also a low preexponential factor of 1.5 s^{-1}.

Obviously the model in [172], where only one mechanism is given, has to be extended. Most likely the reaction of conduction band electron with iodine (reaction 2 at the beginning of this chapter) can be assigned to the reaction with high activation energy because it is the dominant recombination pathway for light intensities >10 mWcm^{-2}.

For the recombination mechanism at low light intensity with a low activation energy, the following reaction mechanism is proposed.

$$1) \quad \boxed{I_2 + \underset{\leftarrow}{\overset{\rightarrow}{}} 2\ I_{TiO2}}$$

$$2) \quad \boxed{e^- + I_{TiO2} \rightarrow I^-}$$
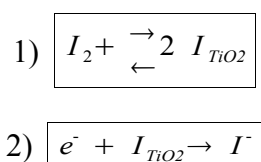
It is analogous to the reduction of iodine on platinum, where the dissociation of iodine is known to be the rate limiting step of the overall reduction [173]. It can be assumed that the equilibrium of reaction 1) is on the left side, thus the concentration of iodine atoms is very small. That is reflected by the small preexponential factor. The reduction itself is facile with a low activation energy (reaction 2). The experimental data fits very nicely with this mechanism, but additional evidence is warranted.
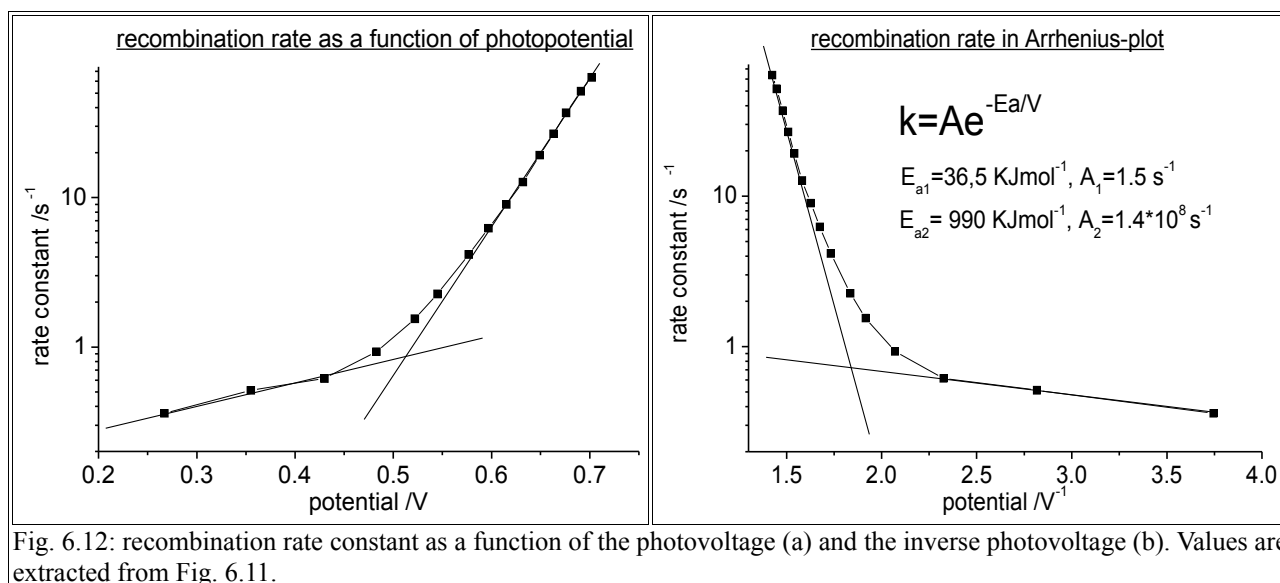
Fig. 6.12: recombination rate constant as a function of the photovoltage (a) and the inverse photovoltage (b). Values are extracted from Fig. 6.11.

6.3.4 The capacitance of the FTO electrode

The capacitance of the FTO-electrode/electrolyte interface C_{FTO} in an operating DSSC is not accessible with standard experimental techniques. It depends on the electrolyte composition, the morphology of the FTO and the area that is occupied with TiO_2-particles. According to an interference reflection study in combination with an analytical model C_{FTO} was found to be $17\ \mu Fcm^{-2}$ for a standard, untreated electrode [174]. In the following, a simple experimental technique is presented that gives the FTO/electrolyte capacitance with an error of ca. 50 %.

The idea is to operate a DSSC with a load resistor R_{ex} under illumination. The current I_{ex} passing the TiO_2/FTO interface can be calculated by $I_{ex} = R_{ex}/U_{ex}$, where U_{ex} is the potential measured at the FTO-front contact. Than the illumination is interrupted and the cell is switched to open circuit operation. Since an electron concentration gradient is present in the cell, the electrons continue to flow to the FTO-contact for some time t_t. Indeed, the photovoltage transient signal increases initially after the illumination was stopped (Fig. 6.13). As t_t approaches zero, the current will be equal to I_{ex}. The electron that pass the TiO_2/FTO interface will charge the FTO/electrolyte capacitor, which can be observed by the potential shift ΔV. Having determined I_{ex} and ΔV one can calculate C_{FTO} by

$$C_{FTO} = \frac{\int_0^{t_t} I_{ex}\, dt}{\Delta V} \quad (6.38)$$

Equation 6.38 can be used as long a t_t is very small. Fig. 6.13 gives ΔV for different bias potential V_{bias}. As expected ΔV does not depend on V_{bias}, which implies that the capacitance of the FTO/electrolyte interface is not influenced by the TiO_2 nanoparticles. However, if V_{bias} is small, the rise of the potential is RC-limited and equation 6.38 is no longer valid. For $V_{bias} > 0.5$ V, the capacitance C_{FTO} is found to be 0.8 µFcm^{-2}. The experiment was repeated at different I_{ex} and in agreement with equation 6.38, ΔV could be predicted by

$$\Delta V = \frac{\int_0^{t_t} I_{ex}\, dt}{C_{FTO}} \quad (6.39)$$

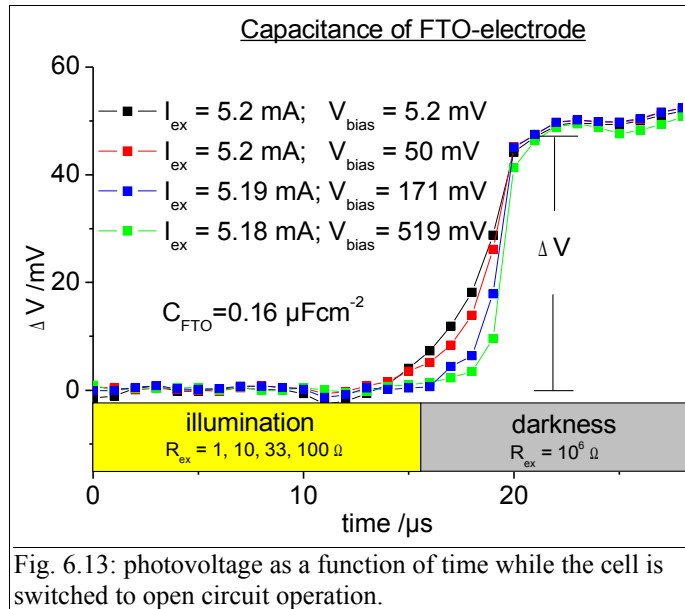

Fig. 6.13: photovoltage as a function of time while the cell is switched to open circuit operation.

The value found for the capacitance is about one order of magnitude smaller than that given in [174]. This can be explained by the $TiCl_4$-post-treatment of the electrodes. By dipping the electrode in an aqueous solution of $TiCl_4$, small, amorphous TiO_2-particles deposit on the electrode

and the FTO substrate. That significantly decreases the contact area between the FTO and the electrolyte and thus C_{FTO} decreases. Without the TiCl$_4$-post-treatment a capacitance of 4 μFcm^{-2} was found, that means that the capacitance is 8 times higher compared to the treated electrode. However, it is two times smaller than the value found in [174], which is attributed to the different type of FTO in that study and the different deposition technique of the TiO$_2$.

These results are in good agreement with a study, in which a compact TiO$_2$ underlayer of ca. 150 nm thickness was used and a capacitance of ca. 1 μFcm^{-2} was found [175]. Compared to the value in [174], this is a 18-fold decrease.

6.3.5 The capacitance of the titanium dioxide

Typically the capacitance of the titanium dioxide electrode is determined with photovoltage transient measurements [164][163]. The cell is illuminated with a constant bias illumination at open circuit potential. At V_{OC}, the Fermi level within the TiO$_2$ film is assumed to be constant. Than a small light pulse is superimposed and additional electrons are injected into the TiO$_2$. This causes the Fermi level to rise within the film before the additional charge carriers recombine. The electron generation by the bias illumination and the pulse are supposed to be constant over the whole film thickness, so the absorption coefficient has to be small. Typically red light is used for this experiment. Most authors claim [14][164] that the total number of injected charge carriers Q_{inj} divided by the peak voltage ΔV of the photovoltage transient gives the capacitance of the electrode.

$$C_{TiO2} = \frac{Q_{inj}}{\Delta V} \quad (6.40)$$

At low light intensity the transient is sometimes RC-limited and a rise time τ_{rise} is observed. Since the electrons already recombine during τ_{rise}, ΔV is found to be too small. In that case the photovoltage decay is extrapolated to t = 0 and the intersection with the y-axis is taken as ΔV, as shown in Fig. 6.14.

Fig. 6.14: bias illumination: 3 mWcm^{-2}; V_{OC} = 510 mV; pulse length = 100 μs
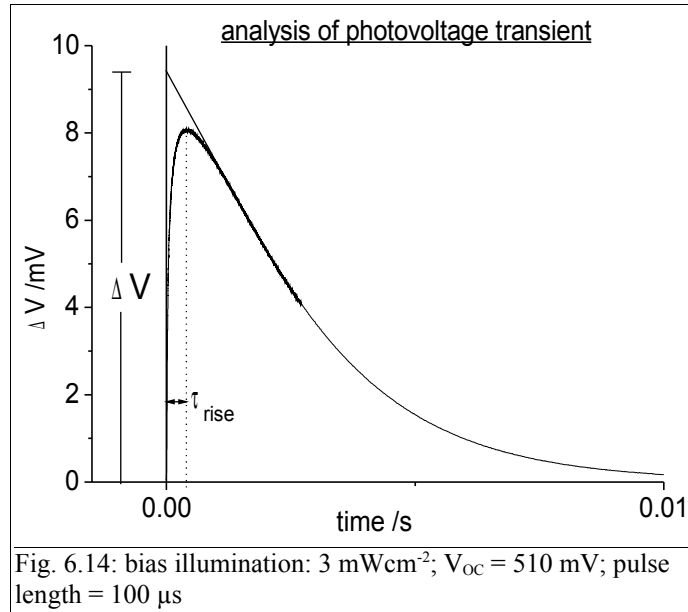
Having identified ΔV, the question arises how to measure the injected charge carriers Q_{inj}. Most authors have measured Q_{inj} by applying the same pulse, which was used for the photovoltage measurement, at short circuit operation and integrate the current over time [14][164][176]. They claim that the charge extraction yield is close to one [164][176] or at least constant [14] (up to 30 % loss). Thus, in the worst case, the capacitance CTiO$_2$ is afflicted with an error, which does not depend on the bias illumination. This assumption seem to oversimplify the situation. The charge extraction probability of an electron will depend on its mobility (expressed by the effective diffusion coefficient D_{eff}) and the recombination rate k_{rec}. More specifically, the diffusion length D_L, given by

$$D_L = \sqrt{D_{eff} * k_{rec}^{-1}} \quad (6.41)$$

has to be longer than the film thickness d.

Both D_{eff} and k_{rec} have been shown to depend strongly on the photovoltage (chapter 6.3.3 and 6.3.7) so charge extraction probability is also expect to depend on the photovoltage. To test this assumption, the same pulse was applied at different photovoltage and the charge extraction Q_{inj} was measured. The highest value (4.3 μCcm^{-2} at 577 mV) was set to one and the relative extraction efficiency is plotted in Fig. 6.15. It can be seen that the charge extraction efficiency decreases with a constant slope of -0.055 %/mV for a photovoltage <577 mV. This can be rationalized by looking at

the recombination rate as a function of photovoltage in Fig.6.12. For a photovoltage <550 mV the exponential decrease of the recombination rate is not as fast as it is between 550-700 mV whereas the exponential decrease of diffusion coefficient does not change in this sector. As a result the fraction of electrons that recombine increases and thus the charge extraction efficiency decreases. Between 550-610 mV the charge extraction efficiency is nearly constant because the slope of both the recombination rate and the diffusion coefficient is the same. Using a single exponential growth fit

$$Y = Y_0 * \exp^{\frac{V_{bias}}{m_c}} \quad (6.42)$$

where Y is the diffusion coefficient and the recombination rate respectively, the parameter m_c is found to be 42.7 mV and 44.0 mV respectively. For a higher photovoltage, D_{eff} does not increase exponentially anymore (Fig. 6.20) whereas the recombination rate k_{rec} does. Again the fraction of electrons that recombine increases the extraction efficiency decreases.

Calculating the diffusion length by equation 6.41, values between $1.5*10^{-3}$ cm and $7.5*10^{-4}$ cm are found. Plotting D_L against the photovoltage gives a similar curve as in Fig. 6.15. The layer thickness d was $1*10^{-3}$ cm.

Using the calibration curve in Fig. 6.15 it is still not known what the absolute value for Q_{inj} is. However, the dependence of the photovoltage on Q_{inj} is clarified and the measured capacitance is only afflicted with a constant error of approximately between -10 % and -20 %.
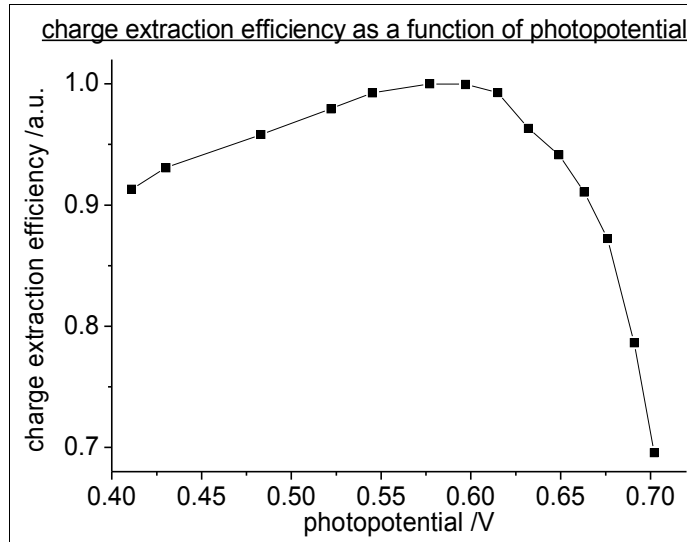
Fig. 6.15:pulse length: 150 µs, bias illumination both from front and back; pulse wavelength: 625 nm; pulse illumination from front side

The capacitance was measured at different photovoltage and the plot is seen in Fig. 6.16. It can be seen that the capacitance increases exponentially for $350\,\text{mV} < V < 710\,\text{mV}$. There is no fundamental or physical reason for this finding but since the empirical observation was made not only in nanoporous TiO_2 electrodes but also in other semiconductors, it is well established to fit the capacitance as a single exponential growth [15].

$$C_{TiO2} = C_{0, TiO2} * \exp^{\frac{V}{m_c}} \quad (6.43)$$

The parameters extracted are $C_{0,TiO2} = 0.301\ \mu\text{Fcm}^{-2}$ and $m_c = 79.7\ \text{mV}$. It should be noted that equation 6.43 cannot be used to determine C_{TiO2} outside the potential range that was experimentally checked. Already for $V < 350\ \text{mV}$, significant deviations from 6.43 were found and it can be expected that C_{TiO2} will level off if V reaches the conduction band.

Fig. 6.16: the capacitance of a nanoporous TiO_2 electrode. The layer thickness was 10 μm, the average particles diameter 20 nm.
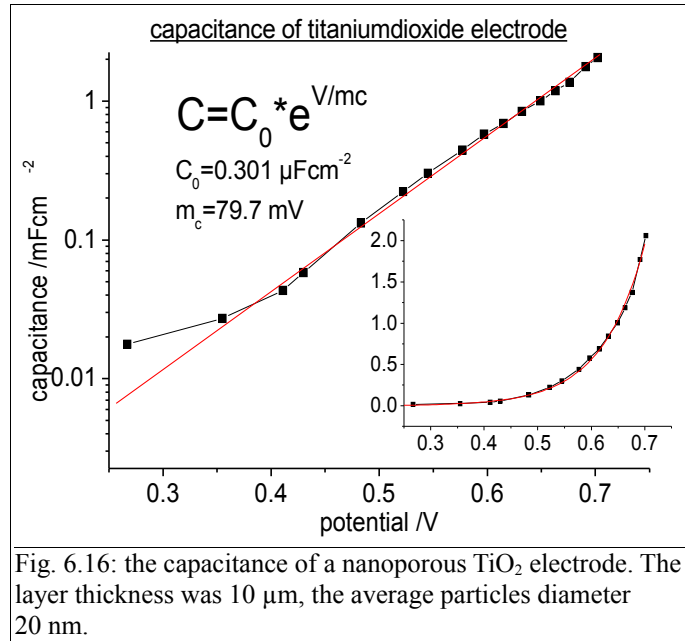
6.3.6 The charge transfer resistance R_{trans}

The charge transfer resistance R_{trans} is the resistance between the TiO_2-layer and the FTO-front contact (Fig. 6.10). It is not the scope of this analysis to interpret R_{trans} since there are many dissenting opinions about the band bending and the potential distribution at the TiO_2/FTO front contact [177][174][175]. It is generally agreed that especially in alkaline environment a potential barrier forms at the interface and that this barrier decreases with increasing photovoltage [177]. But the dominant mechanism for charge transfer, either electron tunneling, charge injection or a combination of both, has not been agreed on yet.

In this study R_{trans} was determined to calculated the potential drop at the FTO/TiO_2 interface at a given point of the I-V-curve. For example, if a DSSC is measured at the maximum power point with $V_{MPP} = 600$ mV, $I_{MPP} = 10$ mAcm^{-2} and $R_{trans}(V_{MPP})=5$ Ω, the potential drop at the interface is expected to be $I_{MPP}*R_{trans} = 50$ mV.

R_{trans} is determined by photovoltage transient measurements at open circuit potential. The nanoporous TiO_2-layer and the FTO/electrolyte interface are treated as two capacitors C_{TiO2} and C_{FTO}, which are connected by the resistor R_{trans}. If a light pulse is superimposed on the bias illumination, additional charge carriers are injected into the TiO_2, which increases the Fermi level in the layer and consequently of the TiO_2-capacitor. The potential difference between the two capacitors equilibrates within a RC time constant. It was already demonstrated that C_{TiO2} is even at low light intensities at

least three order of magnitude higher than C_{FTO} (chapter 6.3.4,6.3.5). That means that V_{TiO2} remains, as a first approximation, constant in this equilibration process and the RC-time constant is determined only by the capacitance of the FTO. Electron diffusion within the TiO_2-layer is believed to have no influence on the RC time constant for the same reason. The electron concentration directly adjacent to the FTO is high enough to charge the FTO-capacitor and the mean length, that an electron has to diffuse, is only 10 nm (for a 10 µm thick layer) in the worst case.

It was demonstrated in chapter 6.3.4 that the capacitance of the FTO/electrolyte interface does not depend on the potential and behaves like a perfect capacitor. Charging can thus be expressed as

$$V(t) = V_{OC} + \Delta V_p * (1 - \exp^{\frac{-t}{R_{trans} * C_{FTO}}}) \quad (6.44)$$

where V_{OC} is the open circuit potential and ΔV_p is the difference between peak potential and V_{OC}. However, equation 6.44 was found to be not sufficient to describe the rise of the transient, since some electrons already recombine within the RC time constant. For this reason the slope of the photovoltage transient immediately after the pulse stopped was taken as a measure for R_{trans}. Differentiating equation 6.44 with respect to t gives

$$\frac{\delta V(t)}{\delta t}(t=0) = \frac{\Delta V_p}{R_{trans} * C_{FTO}} \Leftrightarrow R_{trans} = \frac{\Delta V_p}{\frac{\delta V(t)}{\delta t}(t=0) * C_{FTO}} \quad (6.45)$$

Equation 6.45 can be used as long as the charging of C_{FTO} continues after the pulse stopped. This was true for V < 550 mV. Fig. 6.17 gives R_{trans} as a function of photovoltage. One can identify two branches. Between 390 mV and 550 mV the FTO/TiO_2 interface shows diode-like behavior, that means the current increases exponentially with increasing voltage. Interestingly, in the second branch going from 250 mV to 390 mV, R_{trans} decreases linear with the photovoltage, thus the current I is proportional to $\ln(U/U_0)$.

Fig. 6.17: Charge transfer resistance as a function of photovoltage
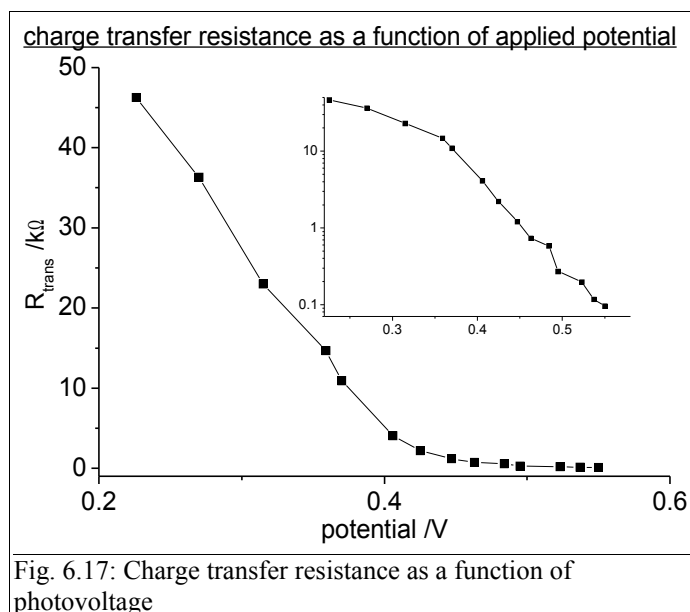
6.3.7 The effective diffusion coefficient D_{eff}

The effective diffusion coefficient D_{eff} describes the mobility of the conduction band electrons in the TiO$_2$. The parameter is not directly accessible but has to be extracted from a model. The general approach was to generate an electron concentration gradient in the TiO$_2$-layer and monitor the equilibration time of the system before the electron concentration is uniform in the whole layer. A concentration gradient can be generated in two ways:

a) The cell is illuminated with a load resistance R_{ex}. A static electron concentration gradient forms. Then the illumination is stopped and at the same time the cell is switched to open circuit operation. The electrons start to equilibrate until an uniform concentration over the whole layer is reached. This method has the advantage that by changing R_{ex}, different concentration gradients can be easily generated and that the equilibration time is typically much faster than the recombination reaction so that as a first approximation electron recombination can be neglected. However, the analysis of the transient is rather complicated because other parameters have to be considered, which affect the accuracy of the measurement. First the potential drop V_{drop} at the FTO/TiO$_2$ interface has to be determined. It depends on the charge transfer resistance R_{trans} and the external current I_{ex}. At high I_{ex}, an overpotential at the counter electrode builds up, because the hole diffusion in the electrolyte is transport limited [159][154]. This overpotential, which shifts the potential of the FTO more positive, is greatly affected by the electrolyte composition and difficult to measure. Finally, the
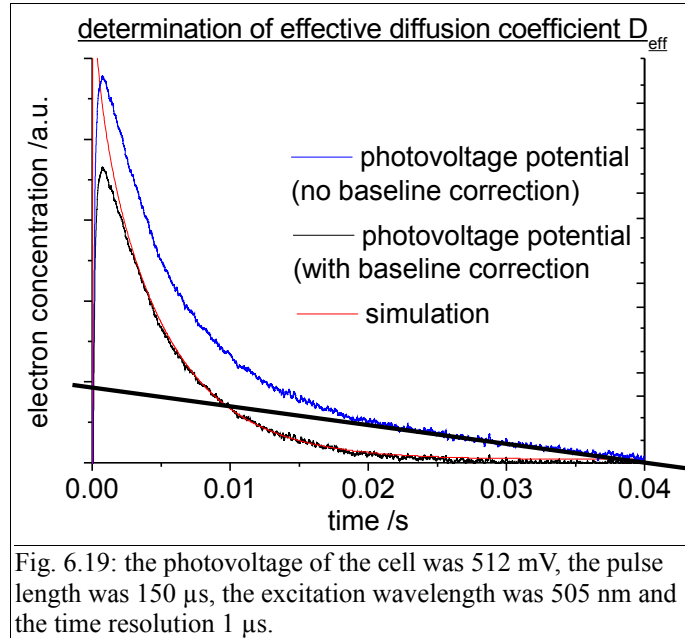
position of the Fermi level within the TiO_2-layer is also based on a model, which includes the electron generation rate k_G, the recombination rate k_{rec}. Using this method after determination of all the parameters needed, it turned out that the value for D_{eff} deviated less than 20 % compared to the method presented in the following.

Fig. 6.18: schematic representation of the electrons chemical potential
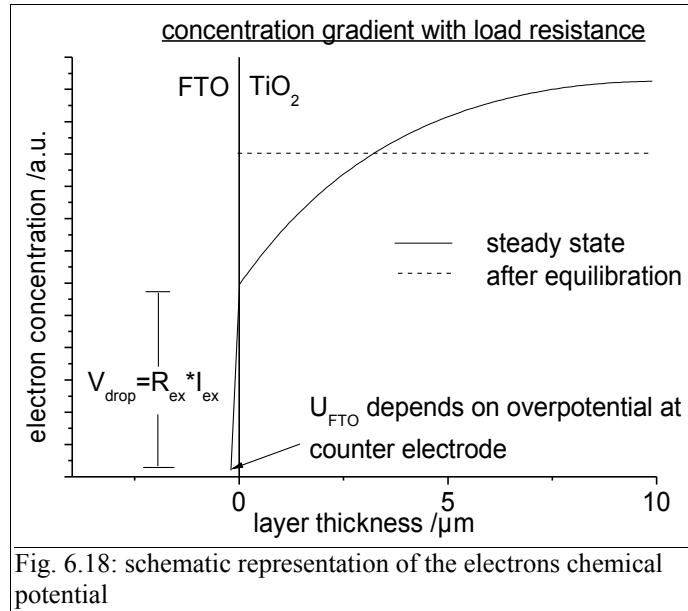
b) The cell is illuminated under open circuit operation both from the front and the back side. That ensures that the electron generation rate k_g, the recombination rate k_{rec} and thus the electron concentration is constant over the whole layer. Than a short LED-pulse of 100 µs with $\lambda = 505$ nm is added to the bias illumination and the photovoltage as a function of time is measured. The only assumption made is that the absorption obeys Lambert-Beers-Law, that means the k_g decreases exponentially with the distance from the front contact. Immediately after the pulse the electron start to diffuse along the concentration gradient into the film and recombine with the electrolyte. Both effects lower the measured photovoltage, however, the recombination reaction is much slower than the equilibration process.

The electron equilibration is modeled with Fick's second law of diffusion. It was found that the equilibration time τ_{eq}, after which the initial electron concentration c_0 generated by the LED-pulse at the FTO front contact ($x = 0$) has decayed to $c_0 * e^{-1}$ depends only on the effective diffusion coefficient D_{eff} and not on the absorption coefficient α or the initial electron concentration c_0. The absorption coefficient α only influences the signal strength, so a wavelength was chosen, which has a high absorption coefficient.

This method works as long as the photovoltage transient is not RC-limited. Since R_{trans} increases significantly with decreasing photovoltage (see above), the RC time constant becomes longer than the equilibration time τ_{eq} for a photovoltage < 400 mV.

Fig. 6.19: the photovoltage of the cell was 512 mV, the pulse length was 150 µs, the excitation wavelength was 505 nm and the time resolution 1 µs.

The analysis of the photovoltage transient includes the following steps:

1) baseline correction:

   the electron redistribution is superimposed by the recombination reaction of conduction band electrons with the electrolyte. The rate constant for electron recombination is typically much slower than the redistribution and it can be fitted as a linear decay immediately after the light pulse. The electron recombination is subtracted from the transient as shown in Fig. 6.19.

2) The baseline corrected transient is fitted using Fick's second law of diffusion. The only assumption made is that the initial electron concentration decreases exponentially $C_0*exp^{-\alpha x}$, where C_0 and α are two arbitrary constants. The only input parameter needed is the effective diffusion coefficient D_{eff}. The electron concentration as a function of time and place $c(t,x)$ is obtained and $c(t,0)$ is used to fit the transient. $c(t,0)$ deviates by a constant factor β from the photovoltage transient,

$$c(t,0) = \beta * V(t)$$ (6.46)

however, β does not have any influence on the decay time τ_{eq}. As can be seen in Fig. 6.19, the model fits the experiment very well except the RC-limited sector, which was not included into the model.

Fig. 6.20a shows some examples for baseline corrected photovoltage transients. The extracted effective diffusion coefficients are shown in Fig. 6.20b. It can be seen that the diffusion coefficient increases exponentially with the photovoltage in the sector from 0.44 V to 0.69 V. Than the slope seems to be somewhat less steep, though not enough data points are available for U > 0.69 V. This result strongly supports the thermally activated hopping mechanism that was developed to describe electron transport in nanoporous semiconductor electrodes [15]. The basic idea is that electrons are trapped in localized states with an energy E_{ts} below the conduction band. In order to move from one trap state to another the electron has to be thermally activated to the conduction band. The rate constant k and thus the waiting time for this activation will depend on the energy of the trap state

$$k = A * \exp^{\frac{-(E_{cb} - E_{ts})}{kT}}$$ (6.47)

k is the limiting step for the diffusion and thus the effective diffusion coefficient D_{eff} is proportional to k as long as E_{cb}-E_{ts} > kT. If the photovoltage increases, the energy gap E_{cb}-E_{ts} decreases, which is reflected in the exponential increase of D_{eff} as shown in Fig. 6.20b. For a photovoltage >0.69 V, the thermal activation to the conduction band is no longer rate limiting, and the diffusion is limited by interparticle connections and grain boundaries. The upper limit for the diffusion coefficient in single crystalline anatase is 1 cm^2s^{-1} [169].
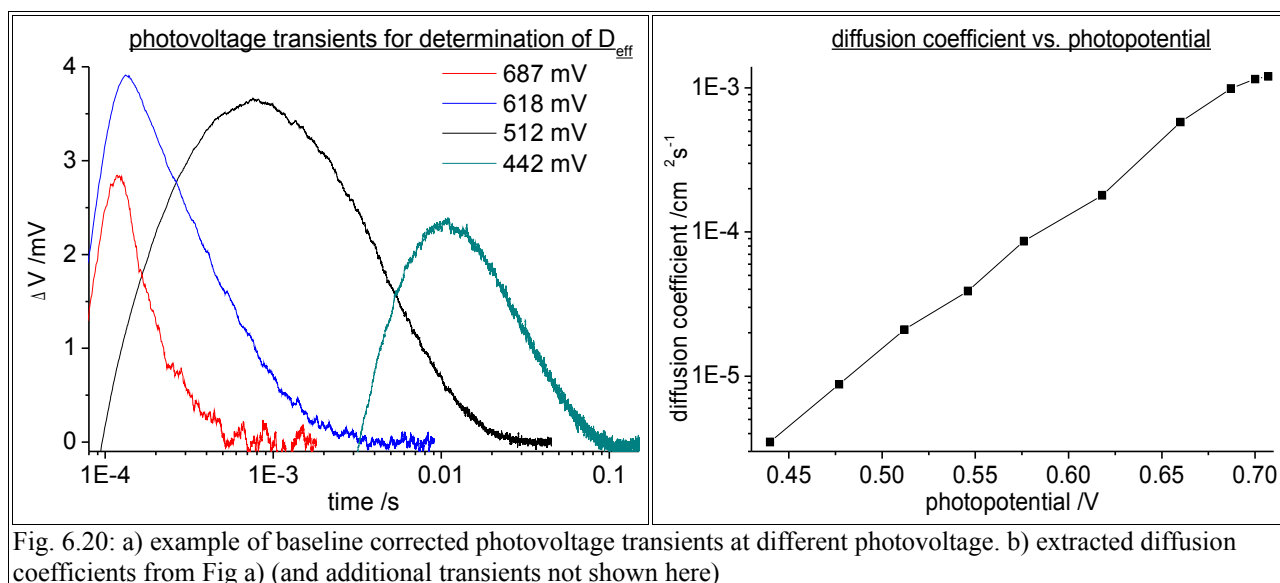
Fig. 6.20: a) example of baseline corrected photovoltage transients at different photovoltage. b) extracted diffusion coefficients from Fig a) (and additional transients not shown here)

For the determination of the effective diffusion coefficient D_{eff} in nanoporous semiconductors, transient photocurrent measurements [176] and intensity modulated photocurrent spectroscopy [178] were already used and described in the literature. The first method suffers the problem, that it needs a trap state distribution as an input parameter and that it has to assume that all injected electrons are extracted at short circuit operation. The authors claim that the latter requirement is fulfilled, however there are indications that the charge extraction efficiency is not independent of the photovoltage (s. chapter 6.3.5). The authors give values between 10^{-8} cm^{2}s^{-1} and 10^{-4} cm^{2}s^{-1} for electron densities between 10^{15} and 10^{18} cm^{-3}. Though the absolute values cannot be compared directly, the exponential increase with the photovoltage that was found, is in good agreement with Fig. 6.20b. The authors of the IMPS-study give a value of $1.5*10^{-5}$ cm^{2}s^{-1} for D_{eff} without the exact photovoltage, so a comparison is again difficult.

To summarize, the determination of D_{eff} from photovoltage transients was not described in the literature before and is proposed as a very simple method that needs no extra input parameters. An exponential increase of D_{eff} with the photovoltage was found supporting the multiple trapping model.

6.3.8 The Fermi gradient within the nanoporous TiO₂-layer

In the previous chapters the transport model was developed and theoretic predictions were supported by experimental evidence. Most parameters can be directly measured and compared to the predicted values. Only the electron concentration within the film is not accessible with the transient technique. However, since the model has been proven to be quite robust, it is worthwhile to check what the predictions of the model concerning the electron distribution within the film are. In this chapter steady state electron distributions both under open circuit potential and with a load resistor R_{ex} are discussed.

At a photovoltage near the open circuit potential an analytical formula is derived based on the central continuum equation , that gives the electron distribution and thus the Fermi level space resolved.

The following assumptions are made:

– the electron concentration $c(x,t)$ does not change over time, that means that the derivative of $c(x,t)$ with respect to time is zero.

– the recombination rate constant k_{rec}, the effective diffusion coefficient D_{eff} and the capacitance C_{TiO2} do not depend on the electron concentration. For this assumption the Fermi gradient and thus the electron concentration gradient have to be flat, which is true only if one measures near open circuit potential.

– electrons are generated at a constant rate k_G throughout the layer. Therefore the cell was illuminated with a red LED-lamp of 620 nm. The absorbance of the TiO₂ layer at this wavelength was 0.6 that means the optical density is very small. Furthermore the cell was illuminated from the front and rear side, so one can assume a nearly constant electron injection.

– the voltage drop at the TiO₂/FTO interface in negligible, which is true only if the external current I_{ex} is small. In this case, the charge transfer resistance R_{trans} does not have to be taken into account. Again, only near V_{OC}, this assumption is justified.

With these assumptions, equation 6.17 simplifies to

$$\frac{\delta c(x)}{\delta t} = 0 = k_G - k_{rec} * c(x) + D\frac{\delta^2 c}{\delta x^2} \quad (6.48)$$

This integral can be solved analytically

$$c(x) = C_1 * \exp^{\sqrt{\frac{k_{rec}}{D_{eff}}} * x} + C_2 * \exp^{-\sqrt{\frac{k_{rec}}{D_{eff}}} * x} - \frac{k_G}{k_{rec}} \quad (6.49)$$

Two boundary conditions are needed:

boundary condition 1: The electron concentration at the front electrode c(x = 0) can be determined if the capacitance C_{TiO2} and the applied potential V_{bias} is known. Since C_{TiO2} is a function of the applied potential, c(x = 0) is

$$c(0) = \int\limits_0^{V_{bias}} C_{TiO2} dV * V_{bias} = C_1 + C_2 - \frac{k_G}{k_{rec}} \quad (6.50)$$

boundary condition 2: The electron flux at x = d (d is the thickness of the TiO$_2$ layer) is zero.

$$\frac{\delta c(x=d)}{\delta x} = 0 = \sqrt{\frac{k_{rec}}{D_{eff}}} * C_1 * \exp^{\sqrt{\frac{k_{rec}}{D_{eff}}} * d} - \sqrt{\frac{k_{rec}}{D_{eff}}} * C_2 * \exp^{-\sqrt{\frac{k_{rec}}{D_{eff}}} * d} \quad (6.51)$$

By rearrangement of equation 6.50 and 6.51 the constants C_1 and C_2 can be determined and inserted into 6.49. The complete solution to 6.48 is then

$$c(x) = -Ae^{\sqrt{\frac{k_{rec}}{D}}x} - A * B * e^{-\sqrt{\frac{k_{rec}}{D}}x} + \frac{k_G}{k_{rec}} \quad (6.52)$$

$$A = \frac{k_G - \int_0^{V_{bias}} C_{TiO2} \, dV * k_{rec}}{\frac{k_{rec}}{D_{eff}} * \left(1 + \left(e^{\sqrt{\frac{k_{rec}}{D_{eff}}} * d}\right)^2\right)} \quad (6.53)$$
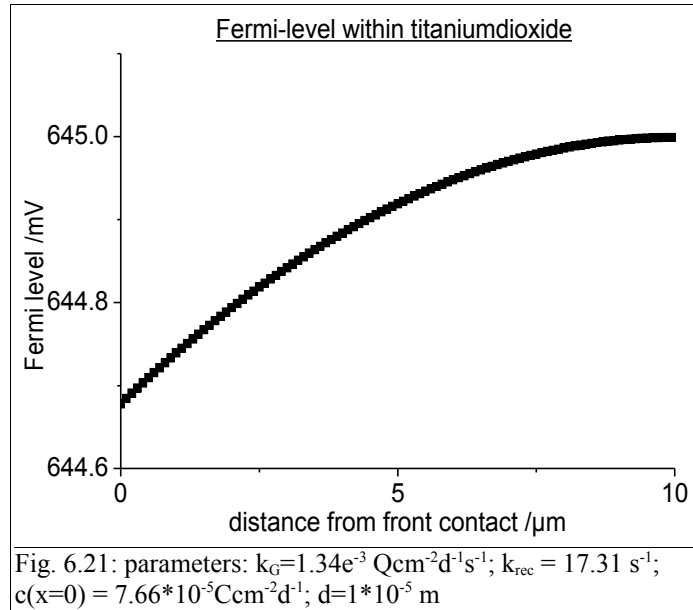
$$B = \left(e^{\sqrt{\frac{k_{rec}}{D_{eff}}} * d}\right)^2 \quad (6.54)$$

Six parameters are needed that have already been discussed in chapter 6.3.2.

– the layer thickness **d**

– the bias potential V_{bias}, which is the potential measured at the front electrode

– **k_{rec}, D_{eff}** and **C_{TiO2}** as a function of the applied potential

– **k_G** is the generation rate and equals the sum of all recombined electrons (with the rate k_{rec}) and the electrons that are extracted and flow through the external electric circuit. The extracted electrons can be easily identified by the ratio of the applied potential V_{bias} and the resistor R_{ex} in the external electric circuit.

$$k_G = c(x=0) * k_{rec} + \frac{V_{Bias}}{R_{ex}} = k_{rec} * \int_0^{V_{bias}} C_{TiO2} \, dV + \frac{V_{Bias}}{R_{ex}} \quad (6.55)$$

It can be seen that the slope of the electron concentration and thus of the Fermi level is mostly determined by the ratio of the regeneration rate to the effective diffusion coefficient D_{eff}. The Fermi level within the TiO_2 near the open circuit potential with the values that were determined in the previous chapters is shown in Fig. 6.21

Fig. 6.21: parameters: $k_G = 1.34e^{-3}$ $Qcm^{-2}d^{-1}s^{-1}$; $k_{rec} = 17.31$ s^{-1}; $c(x=0) = 7.66*10^{-5}$ $Ccm^{-2}d^{-1}$; $d = 1*10^{-5}$ m

Looking at the Fermi gradient at an arbitrary photovoltage the central continuum equation has to be applied and the equation has to be solved numerically. In principal the potential distribution looks like in Fig. 6.22. The potential U_{FTO} is the externally measured voltage. Depending on the external current I_{ex} and the charge transfer resistance R_{trans} the potential V_{drop} drops at the FTO/TiO$_2$ interface. Within the layer the potential is determined by the recombination rate k_{rec}, the effective diffusion coefficient D_{eff} and the generation rate k_G.

Fig. 6.22: schematic representation of the electrons chemical potential
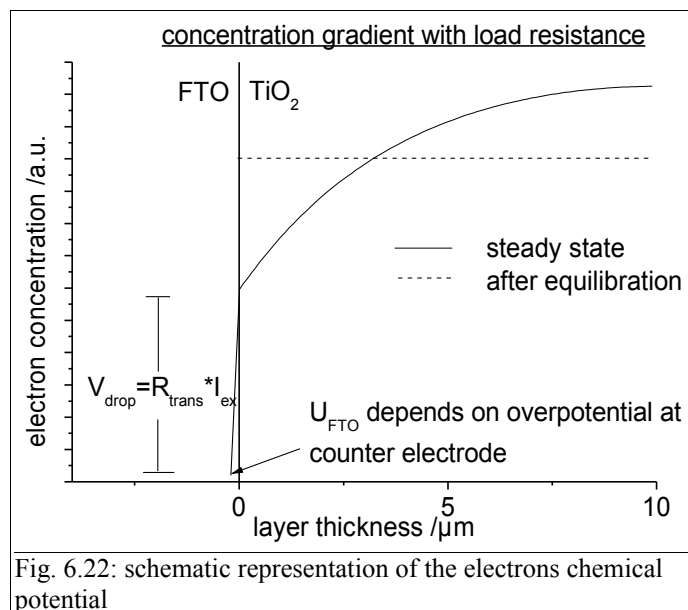
Using the same parameters as for Fig. 6.21 at different photovoltage gives the Fermi level distribution shown in Fig. 6.23. It is interesting to note that most of the potential drops over the TiO$_2$/FTO interface, even near short circuit operation. For example, if the external potential is 13 mV, 489 mV drops over this interface and only 60 mV within the layer. Similar ratios are found at other photovoltage. The voltage drop over the interface is always 4-8 times higher than within the layer.

Secondly it can be seen that the potential drop is negligible if the photovoltage is near V_{OC}. For example at V = 624 mV, the Fermi level changes only by 1.54 mV.

Testing of these predictions were done with the following setup. The cell is operated with a load resistance R_{ex} under constant illumination to generate a certain potential U_{FTO} at the front contact. Then the illumination is stopped and at the same time, the cell is switched to open circuit. If a potential gradient is present, the electrons diffuse initially along the concentration gradient and the photovoltage rises. The peak will be about half of the difference between the potential at the front electrode and at x = d, if a linear gradient is assumed. Indeed for a photovoltage >630 V no rise was detected, whereas the rise at 624 mV was found to be 0.3 mV. This is smaller than the predicted value of ½*1.54 mV, however the value is afflicted with a relative large error due to a noisy signal. For a photovoltage < 600 mV, the measurements were RC-limited and the predicted rise could only be modeled qualitatively.
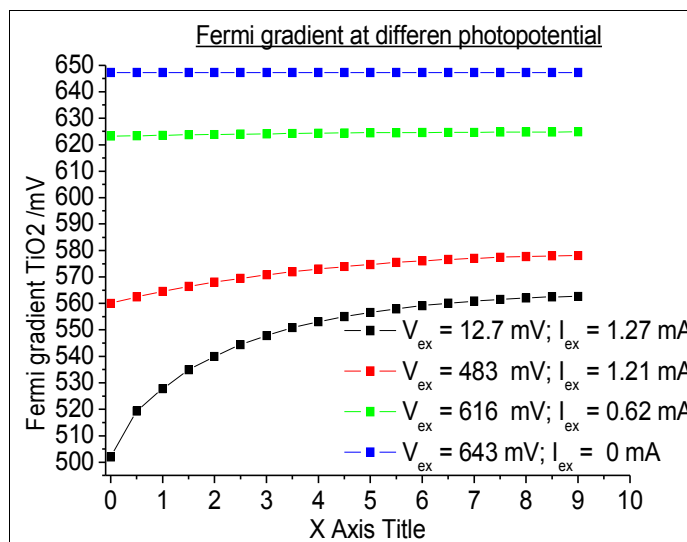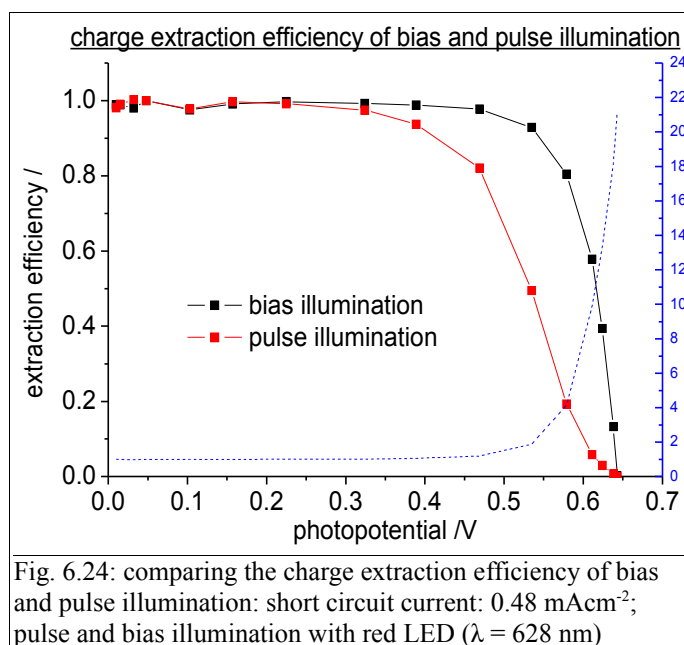

Fig. 6.23: Fermi gradient within the TiO$_2$ layer at different photovoltage

Indirectly the different Fermi gradient within the TiO$_2$ layer can be seen by comparing the charge extraction efficiency η_{bias} of the bias illumination and the charge extraction efficiency η_{pulse} of the pulse. As can be seen in Fig. 6.24, the charge extraction efficiency is up to 20 times higher for the bias illumination than for the pulse at a photovoltage near V$_{OC}$ (blue curve). Near V$_{OC}$, the slope of the Fermi gradient goes to zero near, but the absorption and therefore the charge generation decreases exponentially within the film. So when illuminating with a short pulse, a concentration gradient builds up, which directs the electrons deeper into the film. Thus the extraction probability decreases.

That means as long as the slope of the Fermi gradient is flat η_{bias} will be higher than η_{pulse}. The data in Fig. 6.23 very well matches with the extraction efficiency data in Fig. 6.24. At up to 483 mV, the Fermi gradient within the layer remains flat. Thus $\eta_{bias} > \eta_{pulse}$. Then for V < 483 mV, the Fermi gradient within the layer compensates the concentration gradient of the pulse and η_{bias} approaches η_{pulse}.

Fig. 6.24: comparing the charge extraction efficiency of bias and pulse illumination: short circuit current: 0.48 mAcm^{-2}; pulse and bias illumination with red LED ($\lambda = 628$ nm)
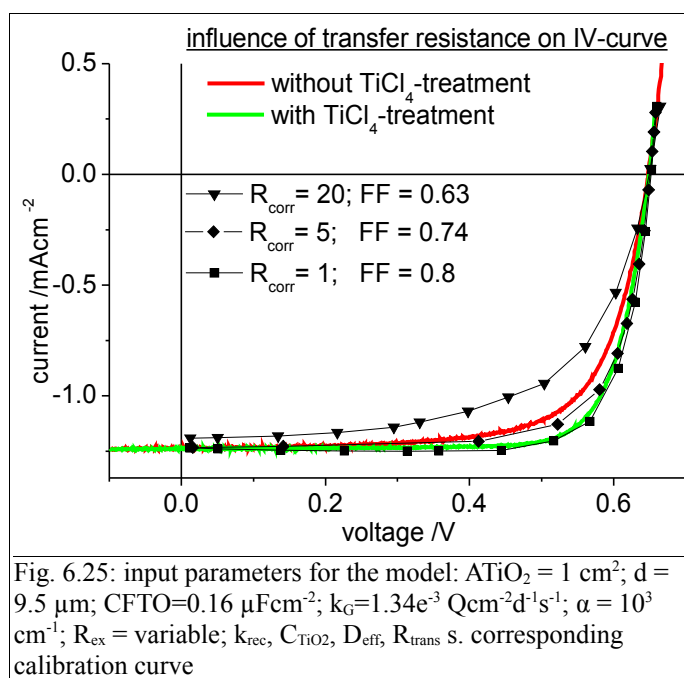
6.3.9 Predictions

As mentioned in the beginning of chapter 6.3, a standard DSSC with a liquid electrolyte (0.6 M PMII, 0.5 M TBP, 0.1 M I_2 in acetonitrile) was used to test the model. First the model was tested under steady state condition with a constant bias illumination to model an I-V-curve by varying the external resistance R_{ex}. As can be seen in Fig. 6.25, the measured I-V-curve (green line) can be fitted very well with the model. The simulation started with an arbitrary initial electron distribution c_0 and it was run until a steady state was reached and c(x,t) was constant.

Then the charge transfer resistance R_{trans} was varied (diamond and rectangle data points in Fig. 6.25) to demonstrated its impact on the fill factor of the DSSC. R_{trans} is one important component of the total series resistance of the cell and is responsible for a voltage drop at the FTO/TiO$_2$-interface. One can see that by introducing a correction factor R_{corr} in order to modify the calibration curve given in Fig. 6.25 the fill factor decreases from 0.8 to 0.63. Obviously the charge transfer resistance R_{trans} is a measure how well the TiO$_2$-particles are attached to the FTO-substrate. One way to decrease the resistance is to increase the contact area of the interface by dipping the electrode into a solution of TiCl$_4$. After annealing in the presence of oxygen a thin amorphous layer of TiO$_2$ is deposited on the FTO/TiO$_2$ surface. If one omits this post treatment (red line in Fig. 6.25), one can see a lower fill factor similar to the fit with $R_{corr} = 5$. Although other parameters (e.g. C_{TiO2}) also change upon the TiCl$_4$ none of them has such a strong influence on the fill factor as R_{trans} has. There is at least some indication that mainly the lower charge transfer resistance is responsible for the better fill factor of these DSSC.

The absorption coefficient α [cm^{-1}] mainly determines, where the charge carriers are generated within the TiO$_2$. The absorbance A_λ is dimensionless and defined by the product of the absorption coefficient and the layer thickness d. A value of $A_\lambda = 1$ means that e^{-1} of the initial light intensity has decayed within the layer. For red light, A_λ is about 0.6 and for cyan light about 2 (table 6.2). For a higher absorbance, more electrons are injected near the TiO$_2$/FTO interface and the probability for an electron to be extracted to the external electric circuit increases. Modeling I-V-curves with all parameters being the same except the absorption coefficient showed that for the same open circuit potential, the short circuit current I_{SC} increases linear with the absorption coefficient. Compared to uniform charge generation ($\alpha = 0$), I_{SC} is about 5.4 % higher for $A_\lambda = 2$ and 13.9 % for $A_\lambda = 5$ (Fig. 6.25).

Fig. 6.25: input parameters for the model: $ATiO_2 = 1$ cm^2; d = 9.5 µm; CFTO=0.16 µFcm^{-2}; k_G=1.34e^{-3} Qcm^{-2}d^{-1}s^{-1}; $\alpha = 10^3$ cm^{-1}; R_{ex} = variable; k_{rec}, C_{TiO2}, D_{eff}, R_{trans} s. corresponding calibration curve

The difference (ca. 3 % if one compares red and cyan light) is within the error margin of a standard I-V-curve. Other parameters (slight temperature differences, age of the cell, duration of illumination) have an impact in the same order of magnitude, so simply recording I-V-curves with different wavelengths was found not to be a good experiment to test the predictions given in Fig. 6.25.

A better test arrangement was to use a red and a cyan LED as the illumination source and compare the short circuit current at a given open circuit potential. First the light intensity for both LEDs was adjusted to give the same open circuit potential. Then the cell was switched to I_{SC} and the current for the red and cyan illumination was compared. With this direct comparison it was found that the current for the cyan LED was 5.9 % higher than for the red LED. This is about two times higher than the theoretic predictions. That indicates that either the absorption mechanism deviates from Lambert-Beers-Law (e.g. light scattering) or the absorption coefficient is error afflicted. To measure the absorption of the TiO$_2$-layer, the optical properties of each individual cell component (FTO-glass, electrolyte, TiO$_2$) was determined first. Than the absorption of the complete cell was measured and the absorption of the electrolyte and FTO-glass was subtracted. However, since the interfaces within the cell (e.g FTO/TiO$_2$) are different compared to the individual measurements (e.g. FTO/air, TiO$_2$/air) this approach might be oversimplified and the value for α not correct.

Nevertheless, the theoretic predictions could be verified qualitatively and it was shown that the

electron extraction probability depends on the place of the charge generation.

Another way to test the influence of the absorption coefficient α on the photovoltaic characteristics is to monitor the photovoltage rise. For this experiment the cell was stored in darkness at short circuit operation to extract all electrons in the TiO_2 film. Than the illumination started and at the same time, the cell was put to open circuit operation. The photovoltage as a function of time was monitored. Again red ($A_\lambda = 0.6$) and cyan ($A_\lambda = 2$) was used for the experiment. As can be seen in Fig. 6.26, the photovoltage rise for the red light is slower since the mean path length of an electron to diffuse from the place of generation to the front electrode is longer. The corresponding fits can reproduce this observation quite well stressing once again the importance of where the charge carriers are generated.
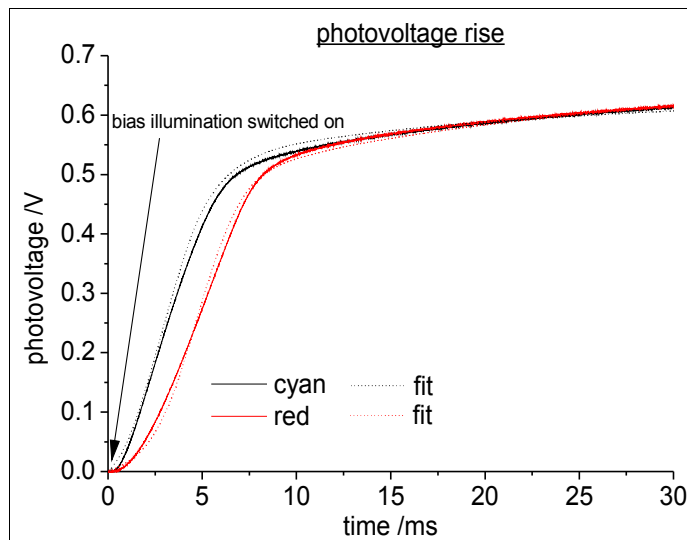
Fig. 6.26: photovoltage rise for a DSSC illuminated with a red and cyan LED (lines). The corresponding fits are given by the dotted lines; input parameters: $ATiO_2 = 1$ cm^2; d = 9.5 μm; CFTO=0.16 μFcm^{-2}; k_G=1.34e^{-3} Qcm^{-2}d^{-1}s^{-1}; R_{ex} = 1 MΩ; k_{rec}, C_{TiO2}, D_{eff}, R_{trans} s. corresponding calibration curve

6.3.10 Testing the model under various conditions

In this chapter photovoltage transients are modeled varying two parameters: the external resistance R_{ex} and the absorption coefficient α. The bias illumination k_g and the pulse length/width are kept constant. Having determined all remaining parameters in the previous chapters, a complete

characterization of the transient can be done with the model including the Fermi level within the TiO$_2$ layer. The test cell was, as previously mentioned, a standard dye sensitized solar cell assembled according to chapter 5 with the following electrolyte composition: 0.6 M PMII, 0.1 M I$_2$, 0.5 M TBP in acetonitrile.

The external resistance R$_{ex}$ determines the voltage measured between front and back electrode of the DSSC. Transients were recorded on different points on the I-V-curve as shown in Fig. 6.27. Four transients were chosen to be modeled: at V$_{OC}$ (R$_{ex}$ = 850 kΩ), at the MPP (R$_{ex}$ = 3300 Ω), at V = 320 mV (R$_{ex}$ = 680 Ω) and close to I$_{SC}$ (R$_{ex}$ = 100 Ω). The bias illumination and the pulse were both directed to the front electrode of the cell. A red LED (absorbance A$_\lambda$ = 0.6 for the 10 μm thick layer) and a cyan LED (A$_\lambda$ = 2) was chosen to demonstrated the effect of the absorbance on the transient signal.
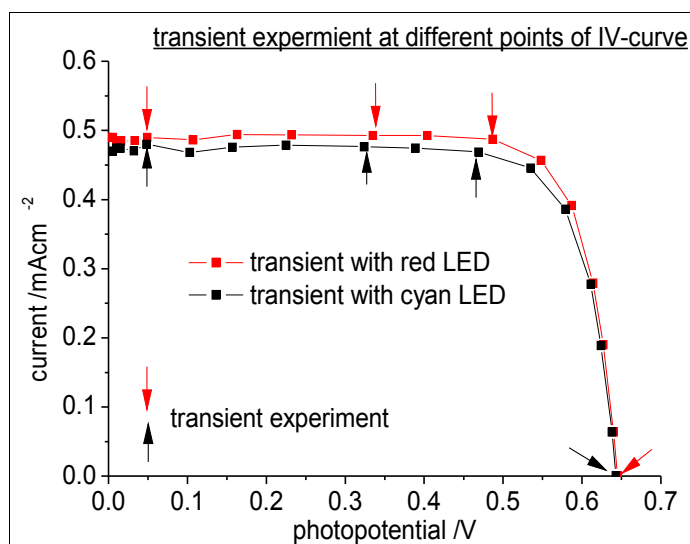

Fig. 6.27: transients measurements at different points of the I-V-curve. The corresponding R$_{ex}$-values were, going from I$_{SC}$ to V$_{OC}$, 1, 10, 33, 100(T), 220, 330, 470, 680(T), 820, 1000(T), 1200, 1500, 2200, 3300, 10000 and 850000(T) Ω.

Fig. 6.28-6.18 give the fits for transients that were marked in Fig. 6.27. Only one parameter set was used for all fits indicating that the model is robust under various conditions.
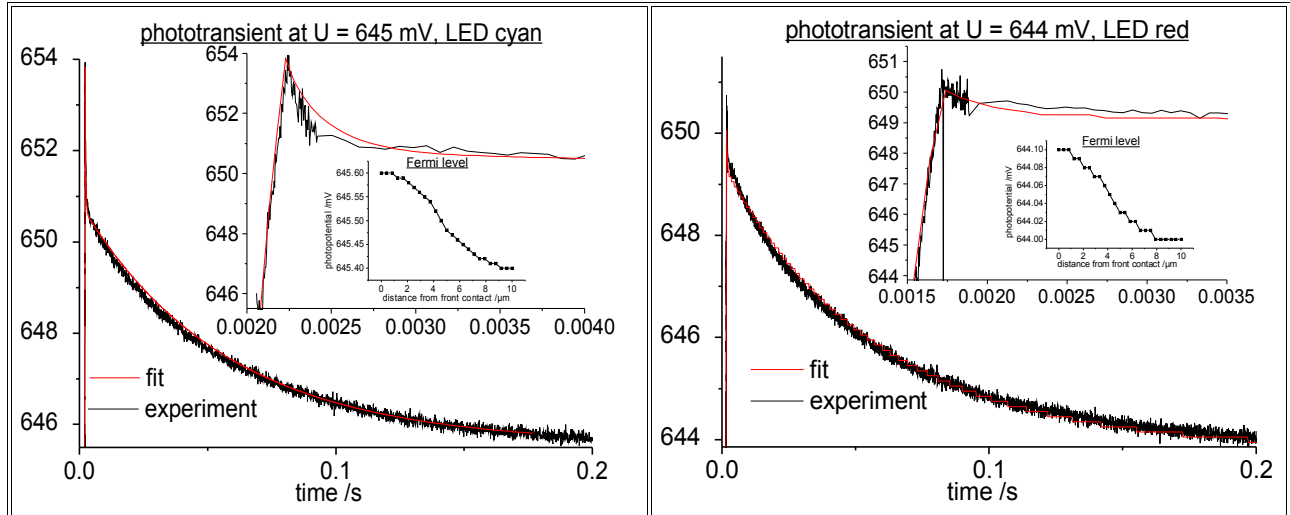
Fig. 6.28: measurement parameter: $ATiO_2 = 1\ cm^2$; $d = 9.5\ \mu m$; CFTO=0.16 μFcm^{-2}; $k_{G,bias}$=0.49*10^{-3} Qcm^{-2}d^{-1}s^{-1}; $k_{G,pulses}$=4.8*10^{-5} Qcm^{-2}d^{-1}; α = 0.6 (right figure) and 2 (left figure) respectively; R_{ex} = 680; k_{rec}, C_{TiO2}, D_{eff}, R_{trans} s. corresponding calibration curve
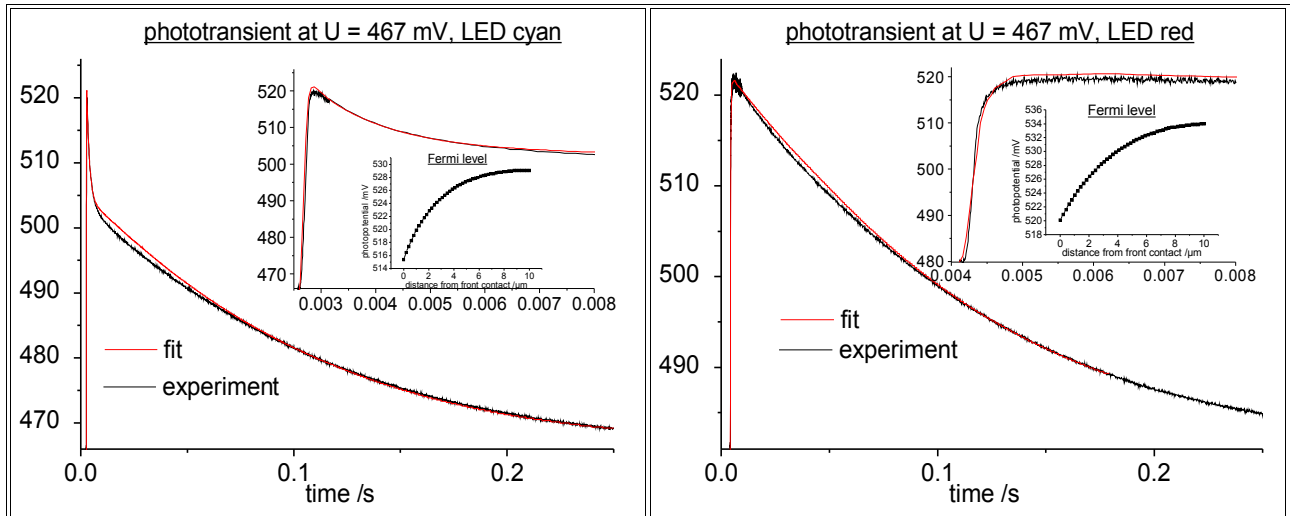
Fig. 6.29: measurement parameter: $ATiO_2 = 1\ cm^2$; $d = 9.5\ \mu m$; CFTO=0.16 μFcm^{-2}; $k_{G,bias}$=0.49*10^{-3} Qcm^{-2}d^{-1}s^{-1}; $k_{G,pulses}$=4.8*10^{-5} Qcm^{-2}d^{-1}; α = 0.6 (right figure) and 2 (left figure) respectively; R_{ex} = 680; k_{rec}, C_{TiO2}, D_{eff}, R_{trans} s. corresponding calibration curve

Fig. 6.30: measurement parameter: $A_{TiO_2} = 1$ cm^2; d = 9.5 μm; CFTO=0.16 μFcm^{-2}; $k_{G,bias}$=0.49*10^{-3} Qcm^{-2}d^{-1}s^{-1}; $k_{G,pulses}$=4.8*10^{-5} Qcm^{-2}d^{-1}; α = 0.6 (right figure) and 2 (left figure) respectively; R_{ex} = 680; k_{rec}, C_{TiO2}, D_{eff}, R_{trans} s. corresponding calibration curve

Fig. 6.31: measurement parameter: $A_{TiO_2} = 1$ cm^2; d = 9.5 μm; CFTO=0.16 μFcm^{-2}; $k_{G,bias}$=0.49*10^{-3} Qcm^{-2}d^{-1}s^{-1}; $k_{G,pulses}$=4.8*10^{-5} Qcm^{-2}d^{-1}; α = 0.6 (right figure) and 2 (left figure) respectively; R_{ex} = 100; k_{rec}, C_{TiO2}, D_{eff}, R_{trans} s. corresponding calibration curve
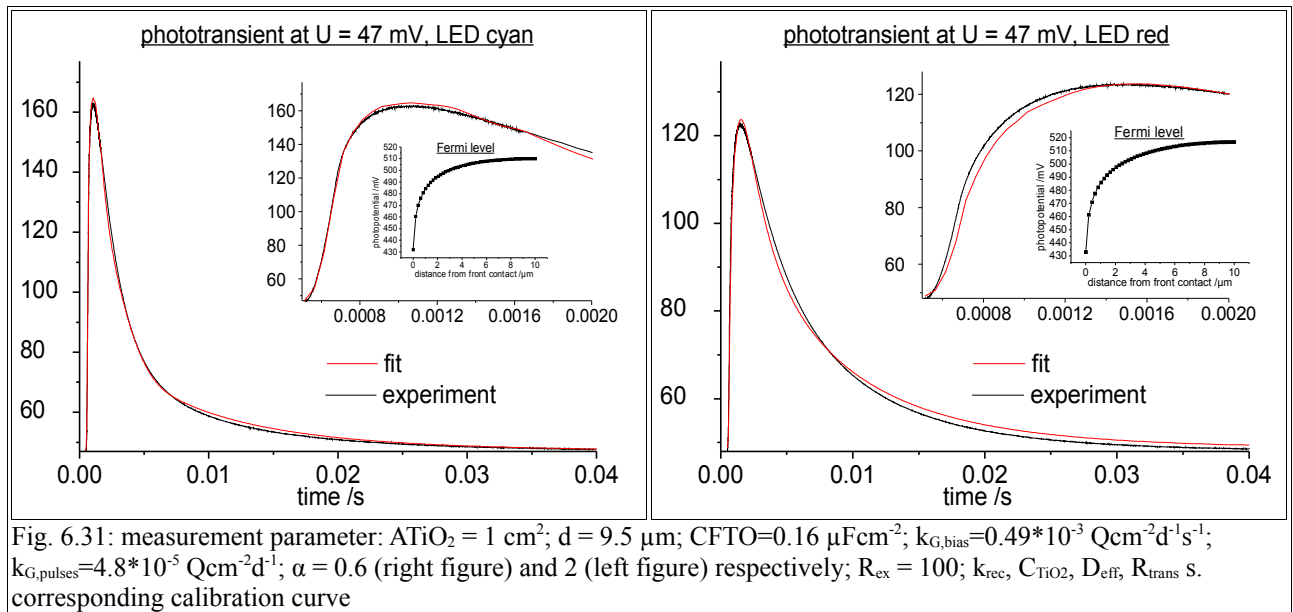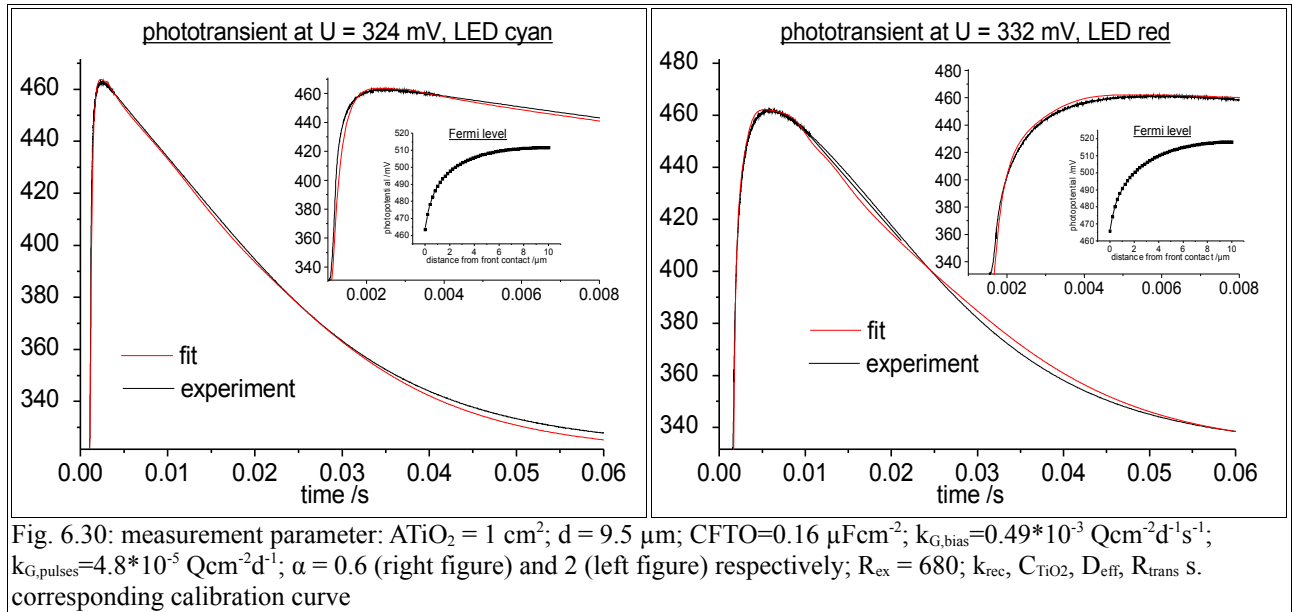
The different absorption of the layer is mainly reflected in two ways.

1) If the Fermi gradient is flat within the layer (Fig. 6.28 and 6.29) an extra voltage decay is seen within the first few μs - ms. Since the absorption and thus the charge injection decreases exponentially from the front contact, the electrons diffuse along the concentration gradient into the layer until the concentration has equilibrated. As a result the electron concentration decreases at the front contact and the measured potential is lower. The effect is more pronounced if the absorbance of the layer is high, which can be seen by comparing Fig. 6.28a/ 6.28b and 6.29a/ 6.29b.

2) The mean diffusion length of the electrons decreases for a higher absorbance. Using Lambert Beer's Law, one can calculate the distance from the front contact where half of the electrons were injected. Solving

$$\int_0^d A * e^{-\alpha x} = 2 * \int_0^x A * e^{-\alpha x} \quad (6.56)$$

for x gives

$$x = \frac{-\ln\left(\frac{1 + e^{-\alpha d}}{2}\right)}{\alpha} \quad (6.57)$$

where d is the thickness of the layer. Calculating the values for cyan light ($\alpha = 2000$ cm^{-1}) and red light ($\alpha = 600$ cm^{-1}) one gets 2.8 µm and 4.3 µm for the distance where half of the electrons are injected (layer thickness d = 10 µm). This is reflected by the faster decay of transients with cyan pulses if a considerable fraction is extracted from the layer (Fig. 6.30 - 6.18).

The key to understand the shape of the transient at different external resistance R_{ex} is the Fermi level within the TiO$_2$-layer. The Fermi-Level at the front contact is determined by the charge transfer resistance R_{trans} and the current I_{ex}, which gives the potential drop V_{drop} at the FTO/TiO$_2$ interface. The Fermi level at x = d, where d is the layer thickness, is determined by several parameters, including the effective diffusion coefficient D_{eff}, the absorbance of the layer and the recombination rate k_{rec}. Looking at Fermi level at x = 0 and x = d as a function of photovoltage (Fig. 6.32), it can be seen that for a photovoltage > 550 mV there is almost no Fermi gradient present in the TiO$_2$ layer and the potential drop V_{drop} is negligible. Than the potential gap between x = 0 and x = d increases continuously as approaching short circuit current. The Fermi level at x = d is pinned for a photovoltage < 380 mV depending on the absorption coefficient of the layer. Extrapolating the Fermi level at x = 0 for short circuit operation it can be estimated that the potential drop will be around 410 mV ($I_{sc} = 0.49$ mAcm^{-2}).
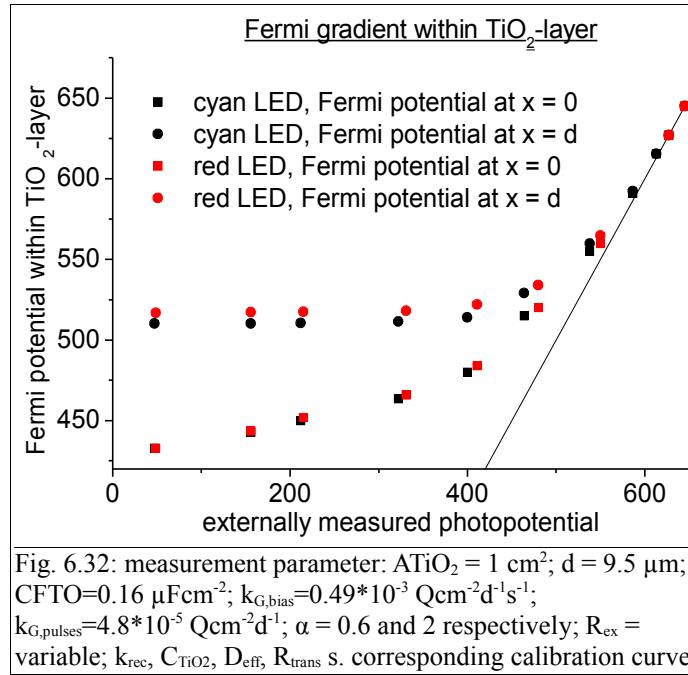
Fig. 6.32: measurement parameter: $ATiO_2 = 1\ cm^2$; $d = 9.5\ \mu m$; $CFTO = 0.16\ \mu Fcm^{-2}$; $k_{G,bias} = 0.49*10^{-3}\ Qcm^{-2}d^{-1}s^{-1}$; $k_{G,pulses} = 4.8*10^{-5}\ Qcm^{-2}d^{-1}$; $\alpha = 0.6$ and 2 respectively; R_{ex} = variable; k_{rec}, C_{TiO2}, D_{eff}, R_{trans} s. corresponding calibration curve

One of the most noticeable features of the transients in Fig. 6.28-6.18 is that the voltage peak increases over one order of magnitude for the same pulse when going from V_{OC} to I_{SC}. At V_{OC}, it is about 5 mV whereas at R = 680 Ω it is already ca. 140 mV. Looking at the peak voltage as a function of photovoltage for more transients, a correlation as in Fig. 6.31 is found. Mainly three parameters determine the shape of the curve:

1) Near V_{OC}, the capacitance of the TiO₂ C_{TiO2} determines the height of the peak ΔV. Since the capacitance decreases exponentially with decreasing Fermi level, ΔV increases exponentially. As a first approximation C_{TiO2} determines ΔV between open circuit potential and maximum power point MPP.

2) Between MPP and short circuit operation the decreasing external resistance R_{ex} determines the height of the voltage peak ΔV. ΔV and R_{ex} are proportional as long as $I_{ex} \approx I_{SC}$. Thus for decreasing R_{ex} the height of the voltage peak also decreases.

3) As can be seen in Fig. 6.28-6.18 and Fig. 6.33 the height of the voltage peak with the cyan LED is significantly larger compared to the red LED when approaching short circuit operation. Near I_{SC} the place of charge generation also determines ΔV. According to equation 6.57, the distance where 50 % of the electrons have been injected is 4.3 µm for the red LED and 2.8 µm for the cyan LED. The ratio, 1.53, matches very will with the ratio of $\Delta V_{cyan} / \Delta V_{red}$, which was found to be 1.7 near I_{SC}.
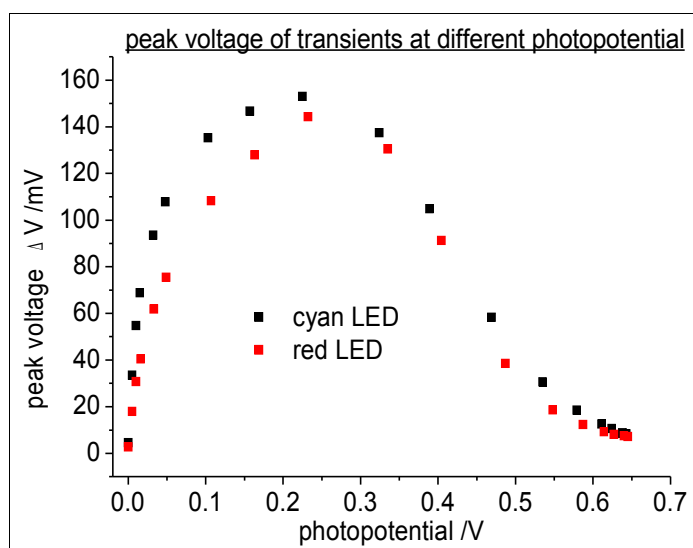
Fig. 6.33: peak voltage ΔV of the transient as a function of photovoltage. The pulse length and width were the same for all transients.

6.4 Nano surface conductivity solar cell (NSCSC)

The application of toxic organic solvents with low viscosity in DSSC imposes mainly two problems for commercialization: what is the ecological impact if a DSSC-module is mechanically damaged and the electrolyte contaminates the environment and how can a liquid with high vapor pressure be encapsulated in a module of 1 m² for at least 20 years? These problems have not been solved yet and new strategies are warranted to replace the liquid electrolyte.

In the following sections the nano surface conductivity solar cell (NSCSC), that was developed within this PhD-thesis for the last two years, is introduced as a novel approach of DSSC with quasi-solid-state electrolytes. The basic idea is to develop a device that equilibrates with the ambient atmosphere and does not need any sealing at all. Hygroscopic salts like LiI are used to attract water from the ambient atmosphere, which is used as a solvent in this device. Air contains about 15 g/m^3 water at 70 % relative humidity (20 °C), which is sufficient to form a supersaturated electrolyte film on the nanoporous TiO_2-particles. The mobility of positive charge carriers in this electrolyte film is high enough to support a photocurrent of about 3.5 $mAcm^2$ for a standard NSCSC.

In chapter 6.4.1 a brief introduction into solid-state DSSC is given and the operation principle of the NSCSC is explained. Then empirical observations that were made within the optimization process of the device and long term stability data are given in chapter 6.4.2. Chapter 6.4.3 deals with the charge transport within NSCSC using transient photovoltage measurements. Chapter 6.4.4 gives experimental evidence on how much solvent on the TiO_2-surface is needed to drive a NSCSC. One of the main challenges in the development of NSCSC is the fast recombination rate at the TiO_2/electrolyte interface. Strategies to slow down the recombination rate are given in chapter 6.4.5. Finally the adjustment of the TiO_2/counter electrode interface is discussed in chapter 6.4.6 and chapter 6.4.7 gives a summary of the experiments and an outlook of upcoming projects.

6.4.1 NSCSC - Operation principle

The NSCSC is an example of DSSC-derivative with a quasi solid state electrolyte so it competes rather with other solid state DSSC than with liquid DSSC in terms of efficiency and long term stability. So far both inorganic and organic hole conductors have been applied in DSSC. The most widely applied inorganic hole conductors are CuI-salts [179][180][181] with a conversion efficiency of up to 4 % initially [182]. Among the organic hole conductors spiro-OMeTAD is the most advanced molecule with a conversion efficiency of up to 4 % [183][184][185]. Among the p-conducting polymers polythiophene [186], PEDOT [187] and polypyrrole [188] have been tested, however, the conversion efficiency in these devices is rather low (up to 1.5 %).

In principal the NSCSC employs the classic LiI/I_2 redox system. However, in contrast to the liquid solution in DSSC with concentrations typically 0.5 M for LiI and 0.05 M for I_2, an supersaturated aqueous solution is present in DSSC, which is the result of an equilibration process with the ambient atmosphere.

$$\boxed{LiI + H_2O \rightarrow LiI_{(aq)}} \quad (6.58)$$
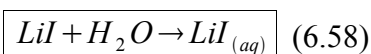
The water uptake of LiI is listed in table 6.3. Anhydrous LiI was used as the starting material. It should be noted that each LiI-unit can contain between 0.5-3 molecules of water of crystallization.

LiI /mg	relative humidity /%	LiI+H_2O (after 24 hours)	LiI*n H_2O, n =
100	50	138	2.8
100	60	145	3.3
100	70	156	4.2
100	80	166	4.9
100	90	175	5.6

Table 6.3: uptake of water at different relative humidity (temperature T = 22 °C)

After 24 hours under ambient atmosphere with variable water content the LiI crystals turn yellowish indicating that it is partly oxidized to I_2 in the presence of oxygen.

In an operating NSCSC ca. 10 mol/dm³ of LiI is present in the nanoporous TiO_2-network, which is quite uniform distributed in the layer with a slight accumulation on the top of the TiO_2-film as can be seen in Fig. 6.34.

Fig. 6.34: SEM-picture of nanoporous TiO_2 with LiI inside the pores. The LiI are the bright spots in the TiO_2-layer, which was confirmed by EDX.
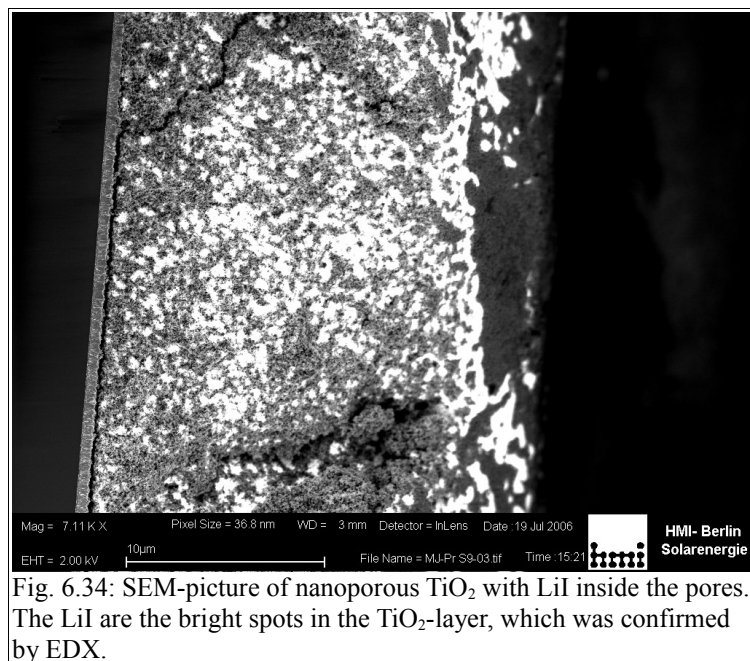
If the NSCSC is exposed to an atmosphere with 60 % relative humidity (22 °C) it takes up about $9*10^{-9}$ mol of water, which corresponds to 6 monolayers of water (chapter 6.4.4).

In addition to the LiI, small amounts of iodine are present on the TiO_2-nanoparticles (ratio I^-/I_2: 100:1). As a result, an supersaturated aqueous solution of LiI/$I_2$ is responsible for the conduction of positive charge carriers in the NSCSC. It is known from the literature, that an I_2/I^--system in the presence of water partly react to I_3^-, I_4^{2-} and to a minor extend to I_5^- and I_6^{2-} [189] and it is believed that the small polyiodide chains play a crucial role in the charge transport. As proposed by other authors working on ionic liquid based DSSC, the charge transport of highly viscous electrolytes is often found to be much faster than predicted by the viscosity of the electrolyte [190][191][192][193]. The most accepted mechanism to explain the enhanced charge transport is a Grotthuss-type mechanism.

$$I_3^- + I_2 \rightarrow I-I...I^- ...I-I \rightarrow I_2 + I_3^- \qquad (6.59)$$
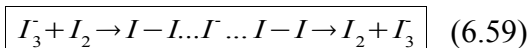
As depicted in 6.59 the electron is transported from one iodine molecule to another by the rearrangement of chemical bonds rather than diffusion of iodide. The rearrangement of chemical bonds is much less sensitive to the viscosity of the surrounding and can even occur in solids (proton diffusion in ice).

Since both iodine and iodide are present in very high concentrations on the TiO_2-nanoparticles in NSCSC, the Grotthus mechanism can support the charge transport from the counter electrode to the oxidized dye. This transport might be supported by diffusion of solvated iodide ions. Fig.6.35 gives a schematic representation of the charge transport in NSCSC.
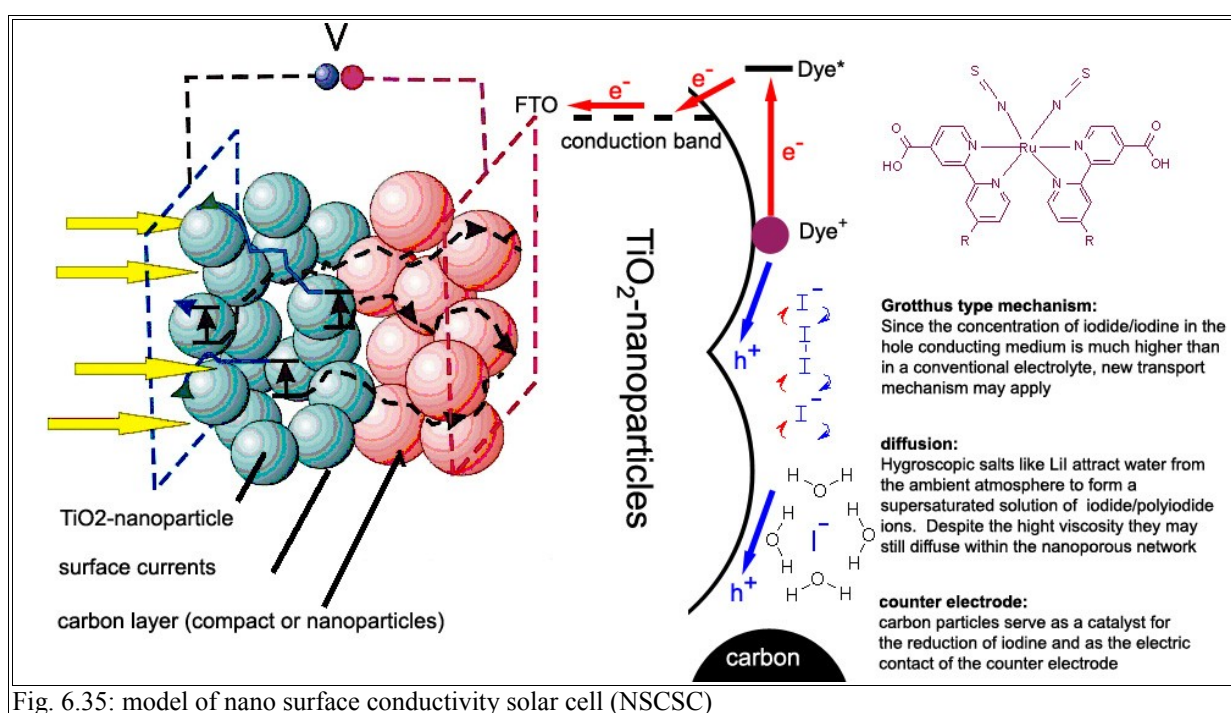
Fig. 6.35: model of nano surface conductivity solar cell (NSCSC)

6.4.2 General findings and long term stability

Some basic properties of the Nano surface conductivity solar cell (NSCSC) are introduced in this chapter. First a general measurement procedure of current-voltage-curves is given. Then the influence of iodine on the photovoltaic performance, the spectral response of sensitized and non-sensitized NSCSC and the long term stability at room temperature is discussed.

Reproducibility is a great concern when cell-performance with different treatment is compared. The

assembly of both NSCSC and DSSC involve many manual production steps making the comparison of cells from different charges difficult. Since the daily production was limited to a maximum of 10 cells in our laboratory better statistics could not be achieved by increasing the number of cells for each experiment. For this reason it was tried to minimize the number of cells and thus the expenditure of time while keeping the reproducibility and reliability of the results as high as possible. The following standards were developed:

1) For all experiments outlined in chapter 6.4, at least three cells were made with the same cell parameters. If one solar cell parameter (I_{SC}, V_{OC}, FF, efficiency) differed by more than 10 % from the others, the cell was not included into the analysis. If one solar cell parameter differed by more than 10 % for all three cells, the whole experiment was repeated.

2) Only direct comparisons between cells of the same experiment were used. It turned out by comparing cells that were made with all parameters being the "same" except the date of cell assembly that the solar cell parameters still differed by up to 30 % in the worst case. Therefore it was decided to draw conclusions only from experiments that were done on the same day, with the electrodes and the electrolyte solution from the same batch and so forth.

The equilibration of the NSCSC with the ambient atmosphere can take several days and the response of the cell to illumination is typically much slower compared to liquid DSSC. Therefore the comparison of the I-V-curves of different NSCSC requires a constant measurement procedure, which was as follows:
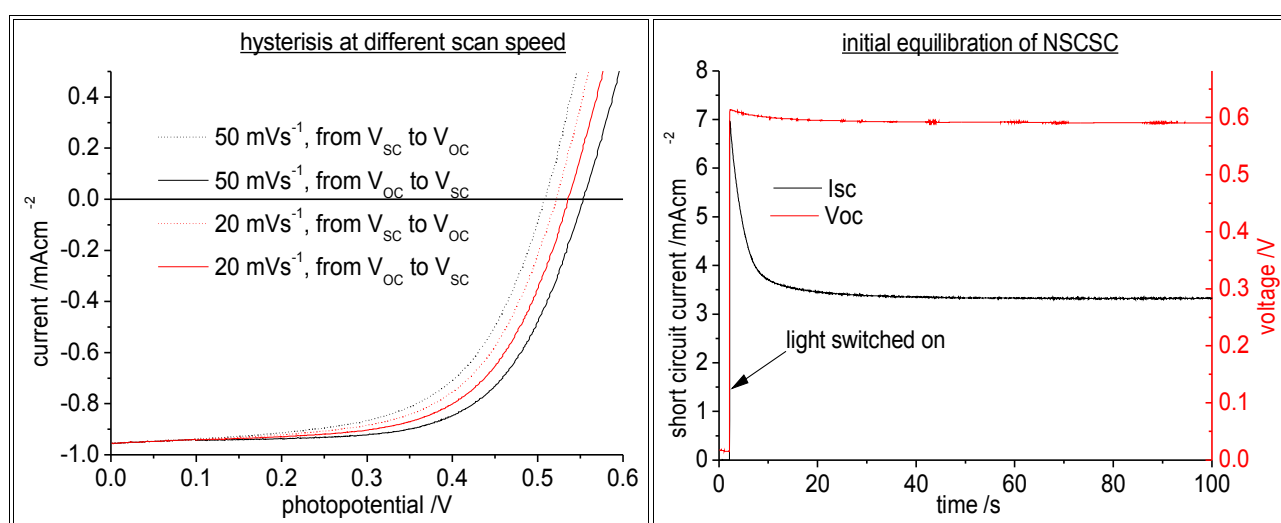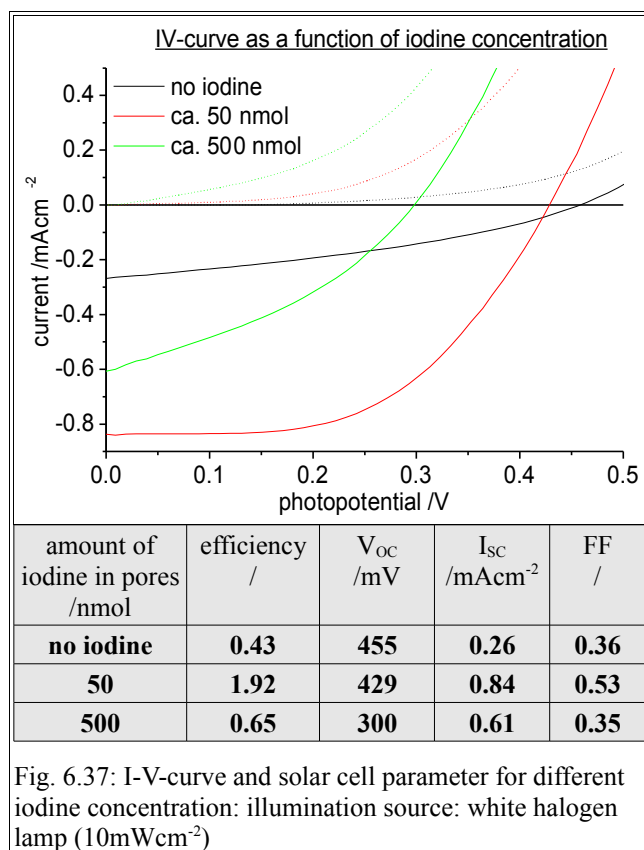

Fig. 6.36: a) hysteresis of I-V-curve at different scan speed (illumination: halogen lamp (15 mWcm^{-2}); b) initial equilibration of short circuit current and open circuit potential (illumination: halogen lamp (100 mWcm^{-2})

1) Hysteresis of I-V-curve: As can be seen in Fig 6.36a, the back and forth scan of the I-V-curve depends on the scan velocity. With increasing scan velocity a hysteresis is found, which is due to capacitive currents flowing in the cell. It was tried to minimize the hysteresis on the one hand while keeping the scan length short. If not stated otherwise a scan velocity of 20 mVs^{-1} was used for all measurements and the average of back and forth scan was used to determine the solar cell parameters.

2) initial equilibration of NSCSC: In Fig. 6.36b, the I_{SC} and V_{OC} of a standard NSCSC is shown as a function of time. It was found that it takes up to 120 s for before a steady state is reached. Since the mobility of I^- and I_3^- is limited on the TiO_2-particles, it takes significantly longer compared to a liquid DSSC before a constant concentration profile is reached. Therefore the cell was illuminated for 120 s at V_{OC} before the I-V-curve was measured. The I-V-curve itself was measured two times and only the second scan was used for the analysis.

The concentration of iodine in a liquid DSSC and a NSCSC determines both the recombination kinetics and the conductivity of positive charge carriers in the electrolyte. The concentration of iodine is typically one order of magnitude less in liquid DSSC and two orders of magnitudes less in NSCSC compared to the iodide concentration. Therefore the transport of positive charge carriers is typically limited by the concentration of iodine rather than iodide [159]. In electrolytes with high viscosity a common tool to increase the conductivity is to increase the concentration of iodine up to 10 times [190]. In long term stability tests a higher iodine concentration (typically two times higher: 0.1 M in standard DSSC) is used to have a buffer if some of the iodine is reduced in the course of the aging experiment [31][194]. At the same time a higher iodine concentration typically enhances the recombination reaction and thus lowers the V_{OC}.

To test the influence of the iodine concentration on the solar cell parameters of a NSCSC, different amounts of iodine were deposited on the surface of the TiO_2-particles: no iodine, 50 nmol and 500 nmol. As can be seen in Fig. 6.37, the cells with 50 nmol performed best in the experiment.

Fig. 6.37: I-V-curve and solar cell parameter for different iodine concentration: illumination source: white halogen lamp (10mWcm^{-2})

amount of iodine in pores /nmol	efficiency /	V_{OC} /mV	I_{SC} /mAcm^{-2}	FF /
no iodine	0.43	455	0.26	0.36
50	1.92	429	0.84	0.53
500	0.65	300	0.61	0.35

The higher recombination rate is reflected by the onset of the dark current. Without iodine the onset is at $V \approx 300$ mV, whereas for higher iodine concentration it is shifted to lower potential. For 500 nmol deposited iodine the rectifying properties is superimposed by a low parallel (ohmic) resistance.

Interestingly the NSCSC works with a modest efficiency even without the addition of iodine. However, the Grotthuss-type mechanism that was discussed in chapter 6.4.1, requires at least some triiodide and the question is, if some iodine is formed in-situ in the NSCSC. For this reason three cells without a sensitizer were operated for one day under illumination with an electrolyte that contained only iodide (cell assembly according to the standard procedure described in chapter 5). Then the electrolyte was extracted with ethanol and the resulting solution was measured with UV/Vis-spectroscopy. Already by visible inspection a yellowish color indicating the presence of iodine could be seen, which was qualitatively confirmed by the broad absorption peak at $\lambda = 295$ nm. Since no sensitizer was present in the cell, the only oxidizing agent in the cell was oxygen, which might either originate from the air or from the titanium dioxide.

For high iodine concentration the recombination reaction is significantly enhanced and thus both the fill factor and the open circuit potential significantly decrease (green curve in Fig.6.37). The color

of the sensitizer irreversibly changes to a brownish hue and the cell degrades within a few days. Obviously the iodine induces some irreversible chemical reaction of the sensitizer, which either affects the sensitizers ability to inject electrons into the TiO_2 or to be regenerated by the electrolyte.

In the course of the experiments to prove the oxidation of iodide on the TiO_2-surface it turned out, that the NSCSC works even in the absence of a sensitizer. NSCSC were assembled according to the procedure described in chapter 5 but without a Ru-dye. Fig. 6.38b gives the I-V-curve of a non-sensitized NSCSC under the illumination of a Steuernagel solar simulator (100 mWcm^{-2}). The short circuit current of the cell is about 20 times smaller compared to a standard NSCSC, reflecting that most of the solar spectrum is not absorbed. However, both open circuit potential and fill factor can compete with sensitized NSCSC.
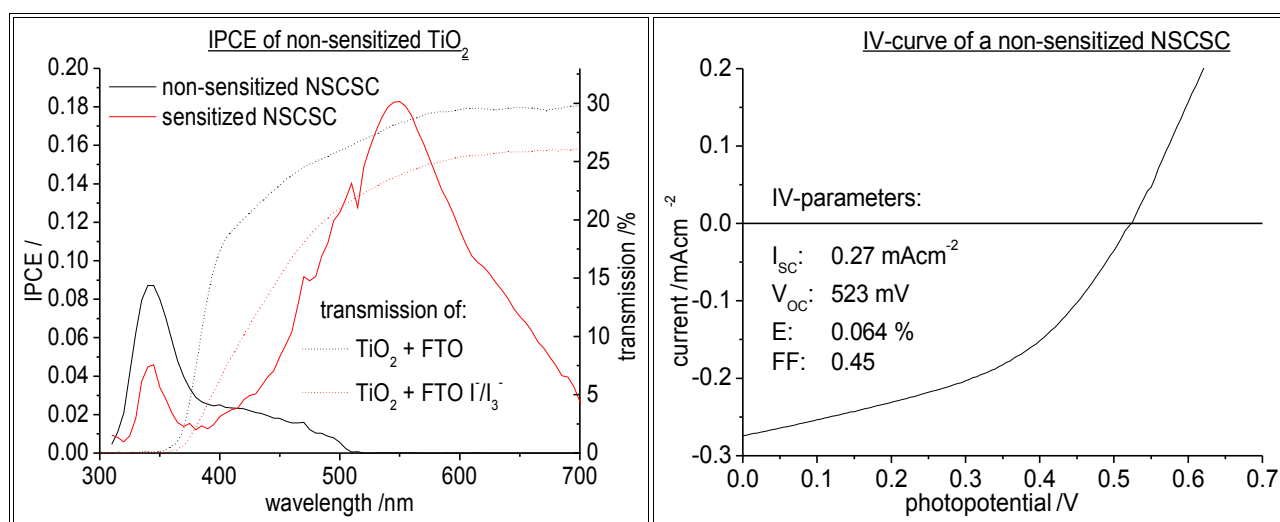
Fig. 6.38: a) IPCE of sensitized/non-sensitized NSCSC of excitation wavelength (xenon flash lamp with monochromator) and transmission of TiO_2 on FTO-glass film with/without electrolyte film
b) I-V-curve of non-sensitized NSCSC (100 mWcm^{-2})

By measuring the spectral response of the cell, it was tried to distinguish between direct band gap excitation and electron injection from sub-band gap states. Fig. 6.38a gives the IPCE as a function of wavelength for a sensitized and non-sensitized NSCSC and the transmission of a TiO_2-layer with/without an electrolyte film. The absorption onset for the nanoporous TiO_2-film is at $\lambda = 350$ nm. As a first approximation, all electrons with $\lambda < 350$ nm are due to direct electron excitation from the valence to the conduction band and if $\lambda > 350$ nm the electrons are injected from localized trap states into the conduction band. Integrating the IPCE-spectrum of the non sensitized

solar and comparing the areas reveals that about 65 % of all electrons are injected from trap states into the conduction band of the TiO_2. Injection occurs in the visible region for wavelength $\lambda < 520$ nm.

These findings are interesting since the photocurrent increases linear with the light intensity and an application as a low-cost photosensor might be possible.

In general the IPCE of a NSCSC is difficult to measure, since the response to an alternating excitation with light is rather slow. As a consequence, the measured IPCE is smaller than expected. Fig. 6.39 shows the IPCE as a function of chopper frequency. Fig. 6.39a gives the absolute, Fig. 6.39b the normalized IPCE. It can be seen that with increasing chopper frequency, the signal strength significantly decreases. Even for the lowest measurable frequency, 15 Hz, the response of the cell cannot follow the excitation. Thus absolute quantum efficiencies could not be obtained with this method.

The signal strength is also a function of the excitation wavelength. The peak at $\lambda = 345$ nm, which is due to the excitation of electrons from trap states, valence band electrons and charge injection from the dye, responds differently to a change of the chopper frequency than the peak at $\lambda = 545$ nm, which is only due to charge injection by the dye.

Thus the interpretation of IPCE-spectra for NSCSC remains rather vague and the method was not used as a standard characterization tool.
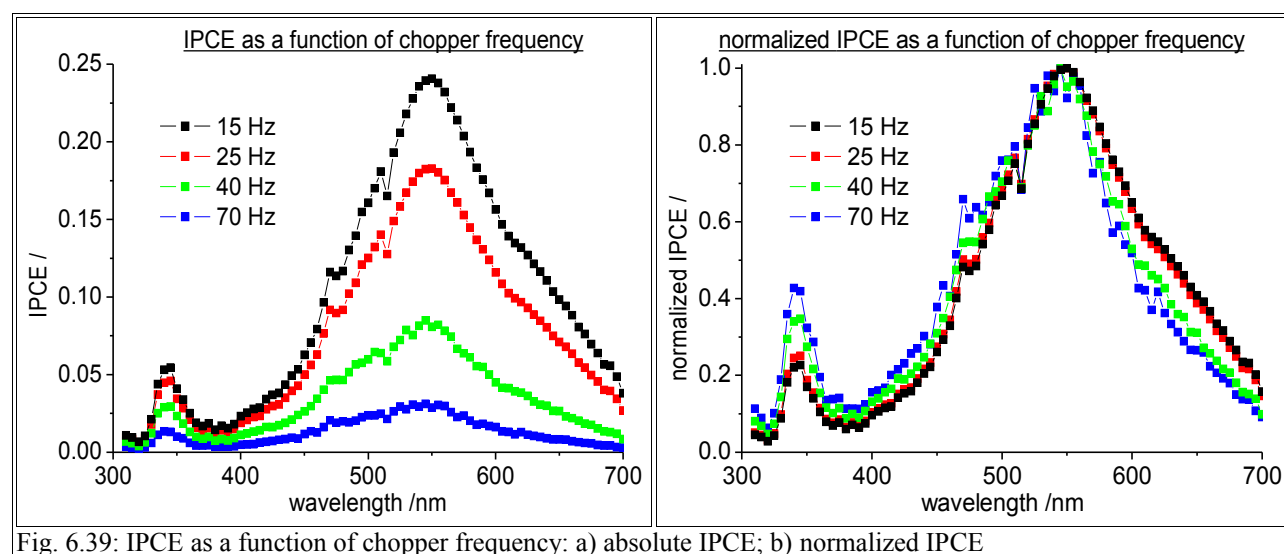

Fig. 6.39: IPCE as a function of chopper frequency: a) absolute IPCE; b) normalized IPCE

Despite these general limitations, the IPCE-spectrum of NSCSCs with different layer thicknesses proved to be useful to demonstrate the short diffusion length of electrons in NSCSC compared to liquid DSSC. The ratio of the diffusion length L_D and the layer thickness d is a measure for the probability that an electron can be extracted from the cell. Assuming that $L_D \approx d$ and that L_D does not depend on the layer thickness, the IPCE should decrease with with increasing layer thickness. Indeed, as can be seen in Fig. 6.40a, the IPCE is inverse proportional to the layer thickness in the measurement interval from 6.8 - 18 µm at the main peak $\lambda = 545$ nm.

In the normalized spectrum in Fig. 6.40b, it can be seen that the IPCE for thick TiO_2-layers is higher for short wavelengths with high absorbance ($\lambda < 370$ nm) compared to longer wavelengths with lower absorbance ($\lambda > 450$ nm). That indicates, that the place of charge generation has an influence on the IPCE. The shorter the distance to FTO-contact, the higher the probability that an electron reaches the external electric circuit.

As a conclusion, the diffusion length of electrons in NSCSC is in the same range as the layer thickness of the TiO_2, and a higher conversion efficiency is expected for thinner electrodes with highly absorbing dyes.
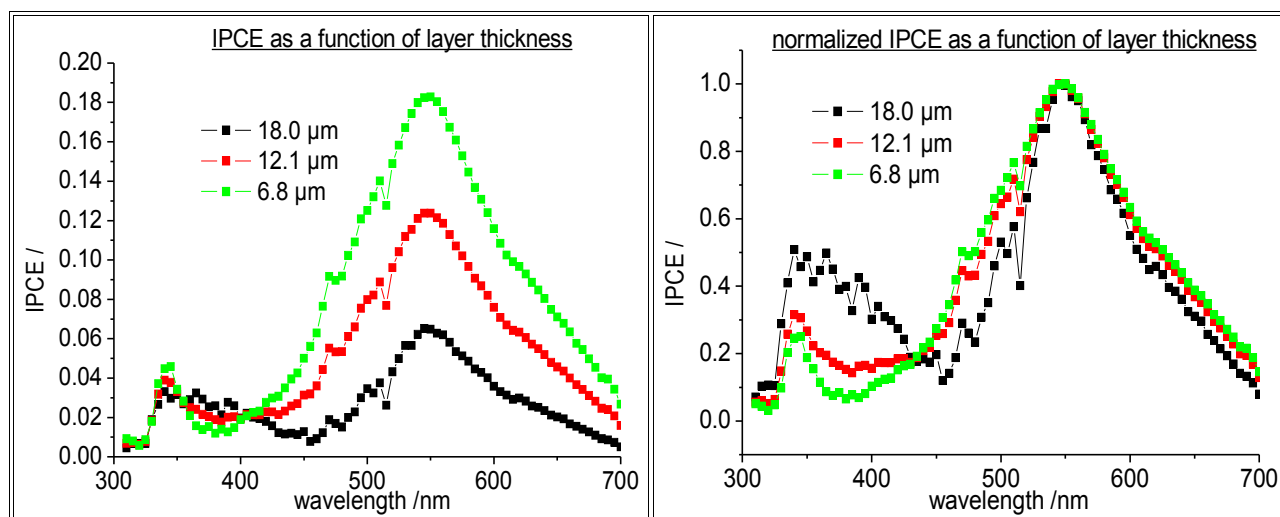
Fig. 6.40: IPCE as a function of layer thickness. Chopper frequency was 15 Hz. a) absolute IPCE; b) normalized IPCE

One of the main drawbacks of alternative hole conductors is that the degradation of the cell efficiency is typically much faster compared to liquid DSSC. For Cu^I-salts some basic stability studies have been done [182][195][179], but for hole conducting polymers and especially for spiro-OMeTAD, no long term stability studies can be found in the literature, which is a strong

indication that the devices degrade rather fast. The degradation found in DSSCs employing Cu^I salts is mainly due to an insufficient pore penetration, crystal growth within the pores and reduction of the thiocynate additive. Organic hole conductors are usually instable in the presence of oxygen of water. Since the NSCSC neither employ organic compounds nor solid crystals, a better stability can be expected.

Since the improvement of NSCSC was an ongoing process during the PhD-thesis, no systematic stability study with standard NSCSC was done so far. However, some preliminary results are available from cells that were kept at room temperature for about one year. Basically three different deposition techniques and compositions of the counter electrode material were compared:

1) dip-coated platinum (7 cells)

2) evaporated carbon (7 cells)

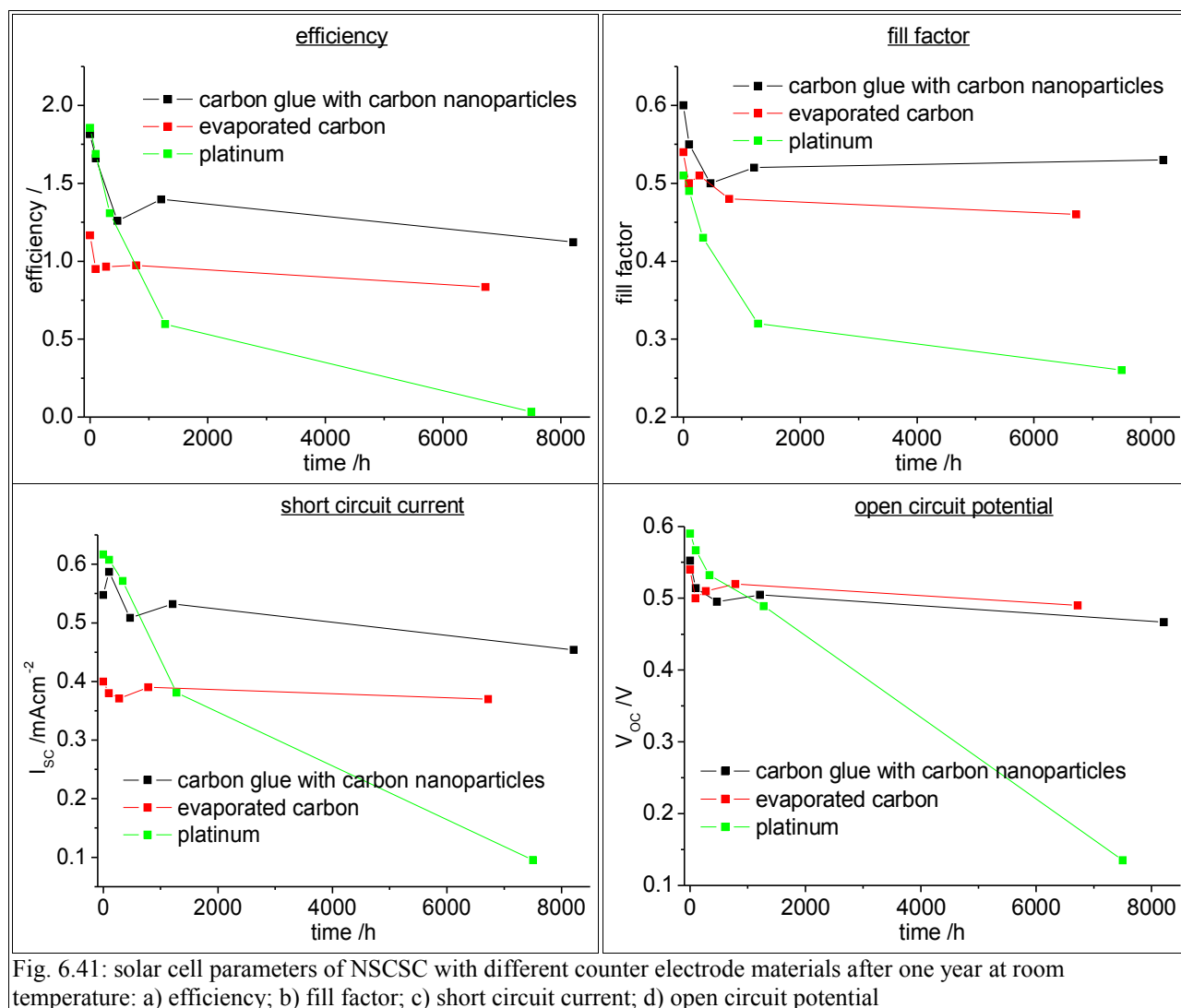3) dip-coated carbon glue with nanoporous carbon particles (5 cells)

Between 5 - 7 cells for each cell type were made and the solar cell parameters were measured in regular intervals (Fig. 6.41). Within the first month about half of the cells degraded for some unknown reason. A bleaching of the sensitizer was detected and the efficiency dropped to less than 10 % of the initial efficiency. It is suspected that an insufficient contact between the TiO_2 and the carbon/platinum counter electrode might be the reason of the observed decay. In this case the oxidized dye cannot be regenerated, which would explain the gradual bleaching.

In the following months a steady decrease of the parallel resistance was observed in some cells. By visible inspection it could be seen that carbon particles were detached from the counter electrode and have short circuited the cell.

After one year, one cell with evaporated carbon, two with carbon glue/carbon nanoparticles, but none with a platinized counter electrode were still working with at least 50 % of the initial efficiency. The data shown in Fig.6.41 depicts the solar cell parameters as a function of time of the best cell for each counter electrode material. Thus the data is not representative but only gives some first hints how stable the cells are in the best case (if no technical problems occur during cell assembly).

Fig. 6.41: solar cell parameters of NSCSC with different counter electrode materials after one year at room temperature: a) efficiency; b) fill factor; c) short circuit current; d) open circuit potential

Despite the limitations of the study it can be seen that the NSCSCs with carbon counter electrodes degraded only were modestly after one year, which clearly shows that both oxygen and water is tolerated by the NSCSC. This is a very important result since the whole cell concept is based on water exchange between the cell and the ambient atmosphere.

The stable V_{OC} (after an initial decrease of 50 mV in the first month the V_{OC} remained nearly constant) gives an indication that the interface dye/electrolyte film/air does not chemically change over time. In contrast to liquid DSSC, were the recombination rate typically increases and the open circuit potential decreases, the recombination rate in NSCSC remains remarkably constant.

None of the cells employing a platinized counter electrode survived the first year although the initial efficiency was even a little bit higher compared to NSCSCs with carbon counter electrodes. It is believed that some platinum is solved in the aqueous electrolyte film and diffuses into the TiO_2-

layer. Since platinum catalyzes the reduction of iodine with conduction band electrons of the TiO_2 the recombination rate in the cell increases significantly.

Although these results are very promising, systematic studies are needed before the stability of this device can be really assessed. Furthermore long term stability test both under elevated temperature and/or illumination are needed.

6.4.3 Charge transport within the nanoporous TiO2 network

A typical nano surface conductivity solar cell (NSCSC) was compared with a standard dye sensitized solar cell (DSSC) by transient photovoltage measurements. The cell assembly was done according to the standard procedure described in chapter 5.

light intensity /mWcm^{-2}	efficiency / %	V_{OC} /mV	I_{SC} /mAcm^{-2}	FF /
10	7.14	686	1.34	0.78
10	1.37	592	0.549	0.42
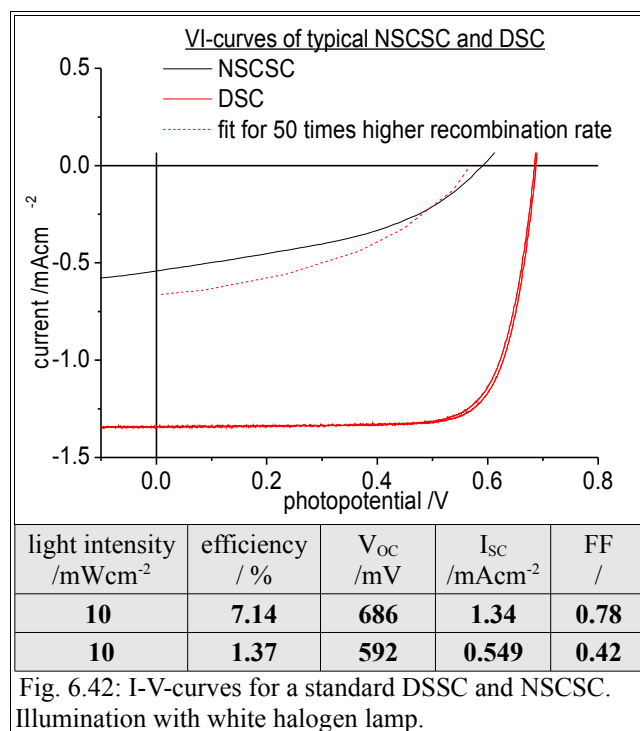
Fig. 6.42: I-V-curves for a standard DSSC and NSCSC. Illumination with white halogen lamp.

The NSCSC and DSSC were stored in darkness at room temperature for one moth prior to the measurement. Especially the initial cell performance of the NSCSC significantly changed within the first few days since the equilibration with the ambient atmosphere is a very slow process that was found to last up to one week. Fig. 6.42 shows typical I-V-curves of a standard DSSC and a standard

NSCSC at 1/10 sun. The NSCSC is about five times less efficient compared to the DSSC, which is mainly due to a lower short circuit current ($\approx$ 2.5 times) and a lower fill factor ($\approx$ 2 times).

Assuming a constant absorption efficiency and a constant charge injection efficiency, it can be concluded that the diffusion length D_L is significantly shorter in the NSCSC. D_L is given by

$$D_L = \sqrt{\frac{D_{eff}}{k_{rec}}} \quad (6.60)$$

where D_{eff} is the effective diffusion coefficient and k_{rec} the recombination rate constant. The question arises, to what extend both parameters contribute to the shorter diffusion length.

To measure the recombination rate k_{rec}, transient photovoltage measurements with NSCSCs were done at different bias illumination at open circuit potential. To ensure a uniform charge generation, a red LED (absorbance of the layer $A_\lambda = 0.6$) was used both for the bias illumination and the pulse. Furthermore the cell was illuminated from the front and back side.

The analysis of the transients follows the procedure introduced in chapter 6.3.3. A set of transients was measured at different bias illumination. The pulse for each transient was the same. A summary of the experiments can be seen in Fig.6.44b (absolute values) and 6.43a (normalized). In Fig. 6.43b, the extracted recombination rates k_{rec} are plotted as a function of the inverse photopotential (Arrhenius-type plot). It can be seen, that k_{rec} was about 50 times higher in a NSCSC compared to a standard DSSC. Assuming an Arrhenius-activated reaction mechanism, two branches are visible similar to those in the liquid DSSCs. The calculated activation energies for both branches are 115 KJmol^{-1} and 622 KJmol^{-1} respectively, which is in the same order of magnitude as the activation energies found for the liquid DSSCs (36.5 KJmol^{-1} and 990 KJmol^{-1}). The two curves mainly differ by a constant factor. The different preexponential factor can be rationalized by the higher surface concentration of iodine in the NSCSC. Since most of the solvent is evaporated in the NSCSC the concentration of I$^-$/I$_3^-$ is between one and two orders of magnitude higher. As mentioned in chapter 6.3.3, the rate constant k_{rec} contains the iodine concentration, thus k_{rec} increases if more iodine is present as an electron acceptor. However, the interpretation of the recombination mechanism remains vague without additional experimental techniques. Though it seems that the rate determining steps are similar in both cells, other mechanisms (e.g. reduction of polyiodide chains) may also apply.
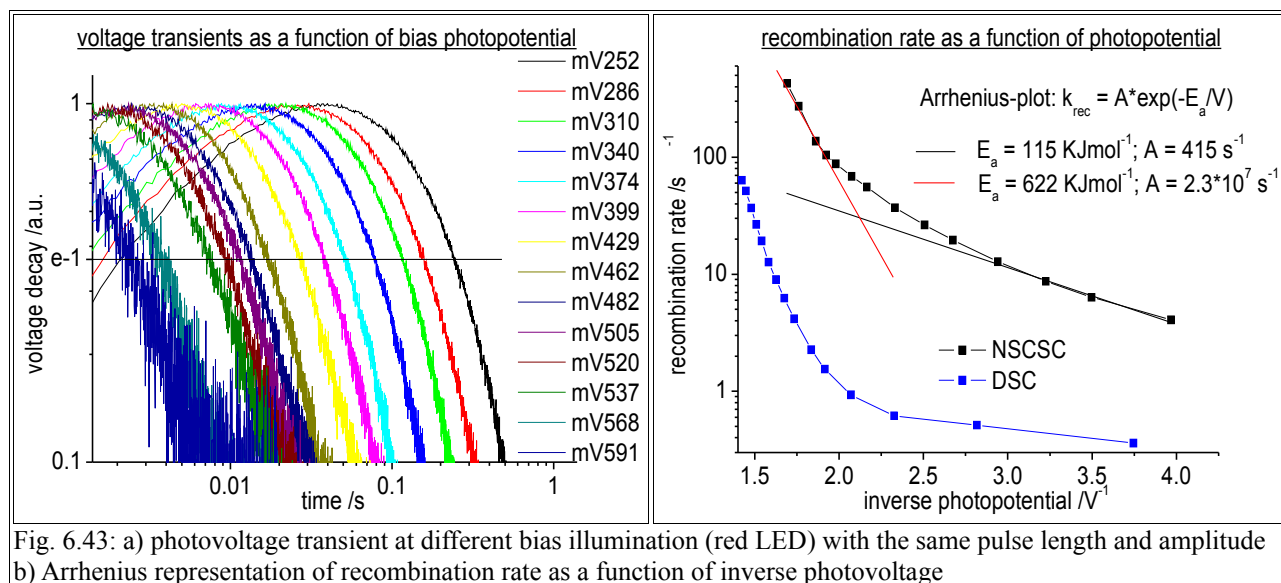
Fig. 6.43: a) photovoltage transient at different bias illumination (red LED) with the same pulse length and amplitude b) Arrhenius representation of recombination rate as a function of inverse photovoltage

The transport model introduced in chapter 6.3 was used to estimate the V_{OC} that is expected with a 50 times higher recombination rate. Using the parameters derived in chapter 6.3 for a liquid DSSC, a shift from 686 mV to 562 mV is predicted. The V_{OC} of a standard NSCSC was 592 mV and thus 30 mV higher. This difference might indicate that the Fermi level of the TiO_2 is shifted more positive in the NSCSC assuming the same trap state distribution. That means that less trap states are available at a given Fermi level and thus the total number of electrons that recombine per second decrease.

Modeling the liquid DSSC with a 50 times higher recombination rate near short circuit operation, a 2.02 times lower current is predicted, which is in good agreement with the experimental findings for the NSCSC. A complete fit of the I-V-curve with all parameters being the same except the recombination rate is shown in Fig. 6.42. It can be seen that by assuming a higher recombination rate both the lower short circuit current and the lower fill factor can be explained.

It was tried to measure the effective diffusion coefficient according to the method described in chapter 6.3.7. However, as can be seen in Fig. 6.44b, the rate of the voltage increase dV/dt, which is needed for the analysis, does not exceed a certain threshold even at high bias light intensity. For this reason, the electrons redistribution, which occurs on a shorter time scale, cannot be seen. In the following, this finding is tried to be explained.

At very low bias light intensity (photovoltage < 300 mV), one can see a RC limitation similar to

liquid DSSCs and the photovoltage rise is delayed. But then, as the charge transfer resistance R_{trans} decreases with increasing photovoltage and the time constant $R_{trans}C_{FTO}$ becomes smaller, one would expect a faster photovoltage rise. As explained in chapter 6.3.1, the photovoltage rise is determined by the charging of the FTO/electrolyte interface, which is considered to be a capacitor with a capacitance of about 1 µFcm^{-2}.

$$V_{FTO}(t) = \Delta V_{max} * \left(1 - e^{\frac{-t}{R_{trans} * C_{FTO}}}\right) \quad (6.61)$$

$$\frac{dV_{FTO}(t)}{dt} = \frac{-\Delta V_{max}}{R_{trans} * C_{FTO}} * e^{\frac{-t}{R_{trans} * C_{FTO}}} \quad (6.62)$$

$$\Delta V_{max} = \frac{\mu_{el,TiO2}}{e} - V_{FTO} \quad (6.63)$$

V_{FTO} = potential at the FTO front contact /V; ΔV_{max} = potential difference between the TiO$_2$ and the FTO /V; R_{trans} = charge transfer resistance at the FTO-TiO$_2$-interface /Ω; C_{FTO} = capacitance of the FTO-electrode /µFcm^{-2}; $\mu_{el,TiO2}$ = chemical potential of the electrons in the TiO$_2$-film /eV; e = elementary charge = 1.6022*10^{-19} C;

Equation 6.61 - 6.63 describe the photovoltage rise for liquid DSSCs.

According to 6.62 the transient dV/dt should be proportional to the peak voltage ΔV_{max} assuming that ΔV_{max} is time-independent, which means that the chemical potential of the electrons in the TiO$_2$ $\mu_{el,TiO2}$ film rises faster than the time resolution of the oscilloscope. Since $\mu_{el,TiO2}$ is proportional to the logarithm of the electron concentration in the TiO$_2$-conduction band and the injection of electrons typically occurs in the femtosecond range, this is believed to be true both for NSCSCs and DSSCs.

However, equation 6.61 assumes, that both electron and hole transport is not limited on a $R_{trans}C_{FTO}$-time scale. This is true for liquid DSSCs, but in NSCSCs, the charge transport is believed be limited due to the following reason. The light intensity of the flash was ca. 10^{17} photons/cm^{2}s^{-1}, which corresponds to ca. 100 % of the AM1.5 spectrum (integrated from 0 < λ < 640 nm). As will be shown later (Fig. 6.45), the short circuit does not increase linearly with the light intensity for an an irradiation > 30 % AM1.5, indicating a charge transport limitation. Thus the charge transport is not limited by the $R_{trans}C_{FTO}$ time constant but by a transport time τ_{tr}, which is significantly longer. If $R_{trans}C_{FTO}$ is substituted by τ_t and under the assumption that $\tau_{tr} \gg t$, equation 6.61 can be simplified by a series expansion. Using a first degree Tayler polynom, it can be written as

$$V_{FTO}(t) = \frac{\Delta V_{max}}{\tau_{tr}} * t, \ t \ll 1 \quad (6.64)$$

The derivative of equation 6.64 with respect to time is then constant.

$$\frac{dV_{FTO}(t)}{dt} = \frac{-\Delta V_{max}}{\tau_{tr}} \quad (6.65)$$

This linear rise of the photovoltage was experimentally observed (Fig. 6.44b). The transport time τ_{tr} will depend on the effective diffusion coefficient of the electrons in the TiO_2, the effective diffusion coefficient of positive charge carriers in the electrolyte film, the concentration gradient of both electrons and positive charge carriers and the bias illumination.

The potential ΔV_{max} depends on the number of charge carriers that are injected into the TiO_2 and the capacitance of the TiO_2. The transients shown in Fig. 6.44b were all measured with the same pulse length and amplitude. Thus, the number of injected electrons can be assumed to be constant. However, ΔV_{max} varies from ca. 3 mV up to 15 mV, indicating that the capacitance of the TiO_2-electrode strongly depends on its chemical potential, which is discussed in chapter 6.3.4 in more detail.

In Fig. 6.44a transients are shown, that were all measured at the same photovoltage V = 340 mV, but with a different pulse amplitude. It turns out that ΔV_{max} increases linearly with increasing pulse amplitude, which indicates, that the injection efficiency of electrons does not depend on the pulse amplitude.
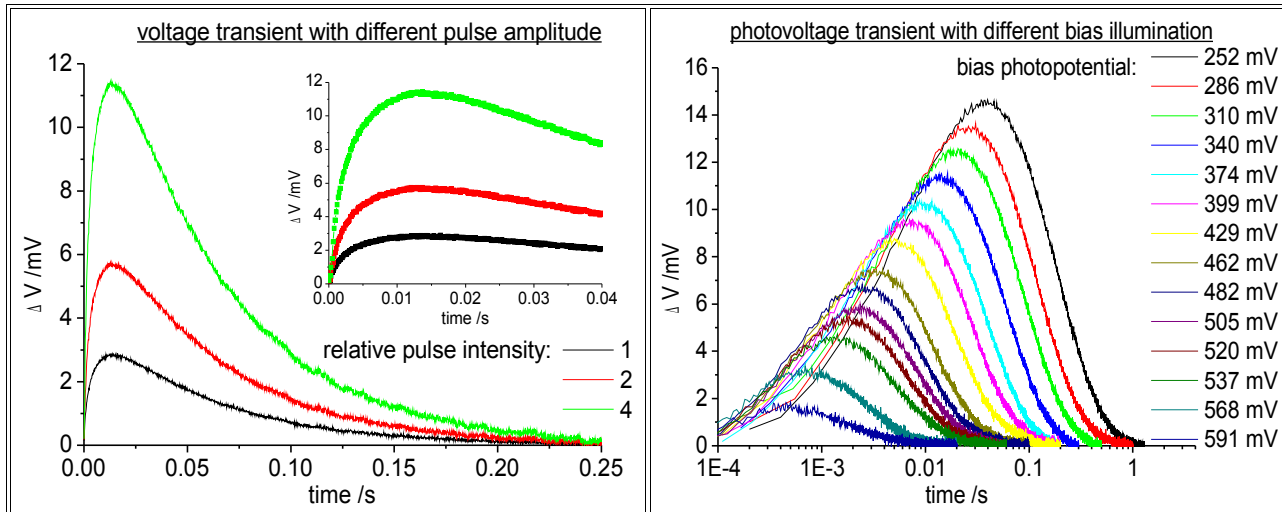
Fig. 6.44:a) measurement at a photovoltage V = 340 mV. The pulse length was the same for all measurements, the pulse amplitude was varied (ratio: 1:2:4)
b) measurement at different photovoltage, which was set by varying the bias light intensity. The pulse length and amplitude was the same for all measurements. Since the capacitance decrease with decreasing photovoltage, the peak voltage ΔV_{max} increase for the same pulse.

To summarize it was shown that the lower efficiency of the NSCSC at 10 mWcm^{-2} bias illumination is due to a 50 times increased recombination rate. Charge transport within the cell and the effective diffusion coefficient of electrons within the TiO$_2$ film at this light intensity is about the same in DSSCs and NSCSCs.

At higher light intensities the transport of positive charge carriers in the NSCSC is expected to limit the short circuit current I_{SC} of the cell. In this case the model developed in chapter 6.3. cannot be applied anymore since one important assumption was that the electron transport in the TiO$_2$ is slower than the transport of positive charge carriers in the electrolyte. To learn about transport limitation within DSSC and NSCSC, the short circuit current was measured as a function of light intensity P_{light}. If neither the electron nor the transport of positive charge carriers is limited, a linear increase of I_{SC} is expected. For the liquid DSSC, this is true for $P_{light} < 200$ mWcm^{-2}, which equals about 2 sun. At this light intensity, a short circuit current of ca. 30 mAcm^{-2} was measured. However, for the NSCSC, the short circuit current starts to level off already for $P_{light} > 15$ mWcm^{-2}, indicating that the cell is transport limited. In principal, both the electron transport and the transport of positive charge carriers can limit the short circuit current. But since the electron transport for the DSSC and NSCSC is similar and electron transport does not limit the I_{SC} for $P_{light} < 200$ mWcm^{-2}, a transport limitation of positive charge carriers in the NSCSC is most likely. According to Fig. 6.45 a maximum current of 3.5 mAcm^{-2} can be achieved with the standard configuration of the NSCSC.

Fig. 6.45: short circuit current at different light intensity.
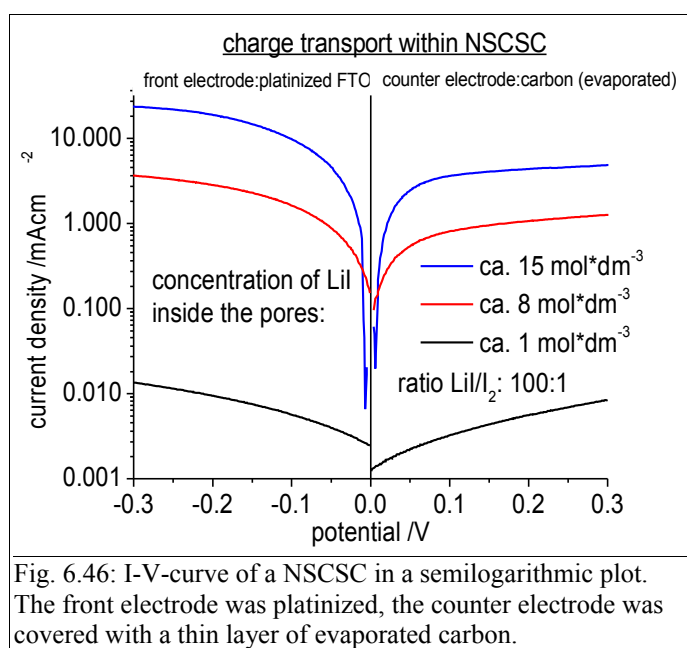Illumination with a white halogen lamp
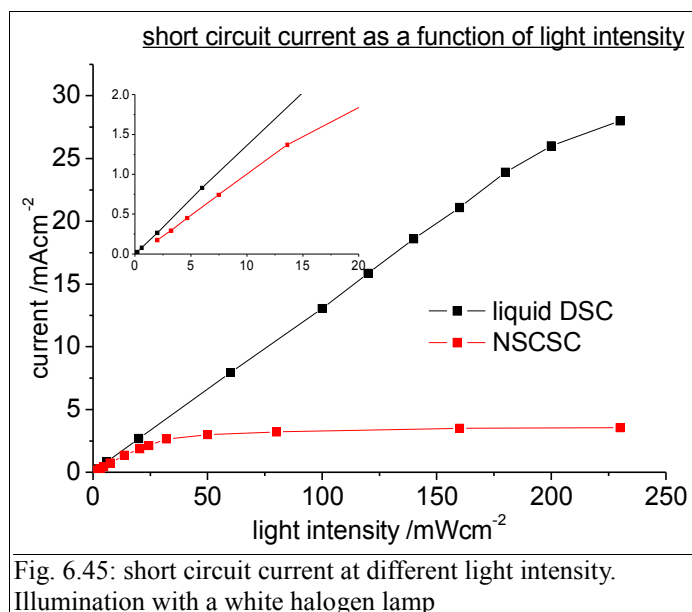
However, without further experimental evidence an electron transport limitation can still not be completely excluded for the following reason. The standard mechanism for electron transport in DSSC assumes ambipolar diffusion, that means electrons and positive charge carriers diffuse together and no electric field builds up. In the liquid DSSC the electrons are shielded by cations in the electrolyte and since the concentration of cations is typically three orders of magnitude higher than the concentration of electrons, the ambipolar diffusion coefficient is mostly determined by the electron diffusion coefficient. This is not necessarily true in the NSCSC. Though the concentration of positive charge carriers is even higher in the LiI/LiI_3-film, the diffusion coefficient for positive charge carriers is expected to be significantly lower, which might affect the ambipolar diffusion coefficient.

It was tried to distinguish between the electron transport in the TiO_2 and transport of positive charge carriers in the electrolyte film by measuring I-V-curves of NSCSCs in the dark. The front electrode was platinized to catalyze electron/hole injection from the FTO substrate to the electrolyte. Since the measurement was done in darkness, no electrons are injected into the TiO_2 and charge carriers are only transported in the electrolyte film.

By applying a positive potential at the front electrode (right branch in Fig. 6.46), holes are injected into the LiI/LiI_3-film. This simulates the hole injection by the dye cation in NSCSC without platinum layer. The positive charge carriers move within the LiI/LiI_3-film to the counter electrode where the iodine is reduced and the positive charge is injected into the carbon layer. As can be seen in Fig. 6.46, the maximum current was 4.8 $mAcm^{-2}$ (at V = 300 mV) for a concentration of LiI/I_2 of

approximately 15/1.5 mol/l, which is the concentration typically used in NSCSC. The saturation current strongly depends on the LiI/LiI_3-concentration. It was found to be 1.2 mAcm^{-2} for $c(LiI) = 8$ mol/l and $c(I_2) = 0.08$ mol/l. At $c(LiI) = 1$ mol/l and $c(I_2) = 0.01$ mol/l the current was around 0.1 mAcm^{-2}.

If normal diffusion is assumed as the dominant transport mechanism a linear increase of the saturation current with increasing concentration would have been expected. The strong increase indicates that a Grotthuss-type mechanism might be dominant.

Fig. 6.46: I-V-curve of a NSCSC in a semilogarithmic plot. The front electrode was platinized, the counter electrode was covered with a thin layer of evaporated carbon.

From Fig. 6.46 it can be concluded that the dominant charge transport limitation is the transport of positive charge carriers. The saturation current of 4.8 mAcm^{-2} is about 40 % higher than the current by varying the light intensity, which gives some indication that also the electron transport is effected. However, since the error of the measurements are estimated to be in the same order of magnitude further experimental evidence is needed.

6.4.4 Influence of solvent concentration on photovoltaic performance

The empirical observation, that the water concentration in the atmosphere is sufficient to support a photocurrent of 3 - 4 mAcm^{-2} in a nano surface conductivity solar cell (NSCSC) raises the question,

how much water (or other solvents) are present on the TiO_2-surface. In this chapter the open circuit potential and the short circuit current as a function of solvent concentration is investigated for three different solvents (water, ethanol and acetonitrile) and an apparatus is introduced that allows the deposition of any liquid solvent in the sub-microgram range on the TiO_2.

Standard NSCSCs have an active cell area of $A_{cell} = 1$ cm² and a TiO_2-layer with a thickness $d = 10$ µm. Assuming a porosity $P_{TiO2} = 50$ %, the volume of the pores within the TiO_2-layer is $V_{pores} = 0.5$ µl. This is the upper limit for the volume of the electrolyte film in the TiO_2-layer. However, in a NSCSC only a fraction of the pores is filled with solvent. Thus a reproducible technique for the deposition of liquids in the range between 0.5 nl as the lower limit and 0.5 µl as the upper limit had to be developed.

First, a brief calculation to convert the volume of the solvent to the number of monolayers on the nanoporous TiO_2-particles surface is given. In the case of water a monolayer has a thickness of about 2.8 Å [196].

The BET surface area of the nanoporous TiO_2-layer is $BET_{TiO2} \approx 50$ m²g^{-1} and the density of TiO_2 is $\rho = 4.2$ gcm^{-3}. For the given cell geometry ($A_{cell} = 1$ cm², $d = 10$ µm) one can calculate the surface area A_{TiO2} by

$$A_{TiO2} = \rho * BET_{TiO2} * A_{cell} * d \quad (6.66)$$
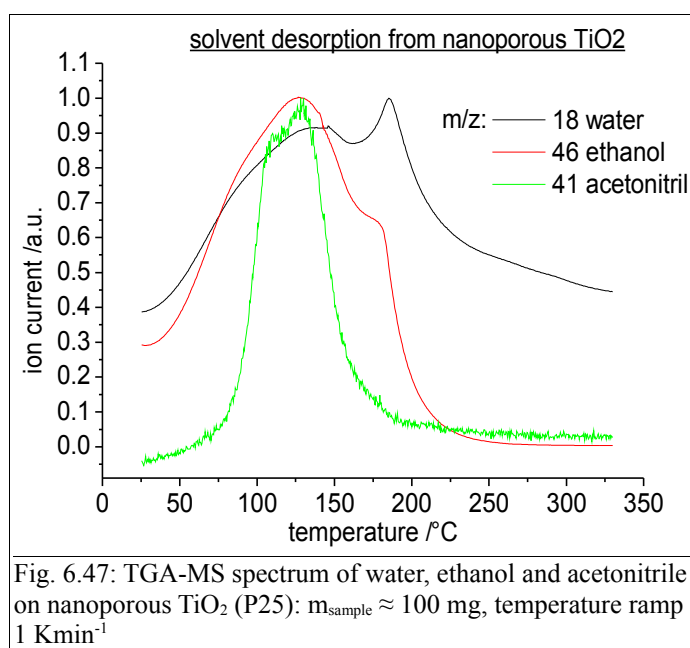
which is 100 cm² for the parameters given. Knowing the thickness of a monolayer and the surface of the TiO_2 one can calculate the number of monolayers n_{ML} by

$$n_{ML} = \frac{V_{pores}}{A_{TiO2} * ML_{H20}} \quad (6.67)$$

For the parameters given the complete filling of the pores would correspond to 17.8 monolayers of water.

Prior to the deposition of solvent molecules, a reference point was defined, which was set to be solvent free. For this reason the desorption of water, ethanol and acetonitrile as a function of temperature was measured by TGA-MS (chapter 3.1). For the experiments, about 100 mg of nanoporous TiO_2 (P25, Degussa) was mixed with 50 mg LiI and 2 mg I_2 and kept in a saturated atmosphere of the respective solvent at room temperature for 24 h. Then the TiO_2 was heated at a rate of 1 $Kmin^{-1}$ and the molecular mass of the solvent was recorded over time with a mass spectrometer.

As can be seen in Fig. 6.47, 90 % of the acetonitrile has desorbed at a temperature T = 160 °C. For ethanol 90 % of the initial amount has evaporated at T = 186 °C. In the case of water the analysis is more complicated since the signal is superimposed by the desorption of water from the walls of the apparatus. At 198 °C a peak is visible that is followed by a constant decrease at higher temperature.

Fig. 6.47: TGA-MS spectrum of water, ethanol and acetonitrile on nanoporous TiO_2 (P25): $m_{sample} \approx 100$ mg, temperature ramp 1 $Kmin^{-1}$

The desorption kinetics significantly depended on the temperature ramp. With decreasing scan rate the temperature $T_{90\%}$, at which 90 % of the initial amount desorbed, decreased. Up to a scan rate of 0.2 $Kmin^{-1}$, $T_{90\%}$ did not saturate. Since the complete desorption of the solvent molecules could only be done at prolonged exposure to temperatures > 120 °C, the TGA-MS-method was not applicable. Thermally induced degradation becomes a serious impediment for long term stability already at a temperature > 80 °C.

Therefore, the desorption of solvent molecules was done at reduced pressure at 50 °C and 10^{-5} mbar

for 24 h. Then the cells were stored under dry argon before the experiment started. It cannot be completely ruled out that traces of solvent (especially water) are still present on the surface, because in contrast to TGA-MS, the desorption kinetics could not be monitored in situ. However, not photovoltaic activity was measured in these "dry" cells ($V_{OC} < 10$ mV, $I_{SC} < 0.1$ µA).

To summarize, a TiO_2-electrode, which was kept for 24 h at 50 °C and 10^{-5} mbar, was defined to be "solvent free" and taken as a reference point.

Fig. 6.48 gives a scheme of the apparatus, that was used for the deposition of volatile liquids. Standard GC-MS equipment was used for the sample loop unit, which was from Vici AG International. The capillaries had 1/16" external diameter and were from Knauer GmbH.

Fig. 6.48: scheme of an apparatus to deposit gases in the range of 10^{-10} mol – 10^{-5} mol.
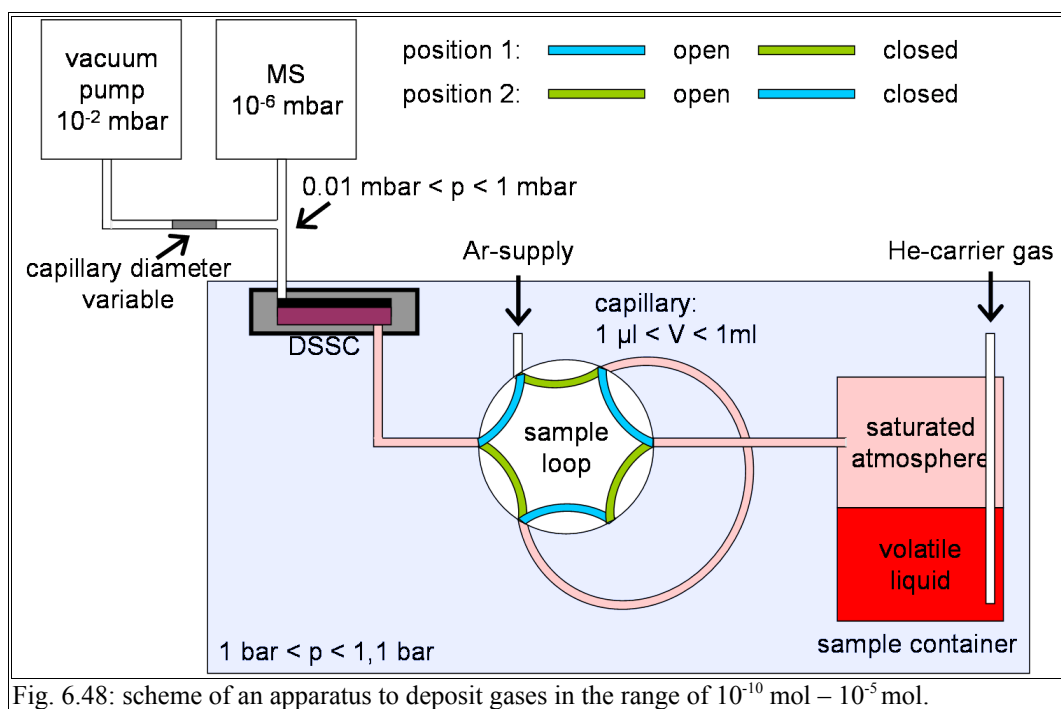
In position 1 (filling mode), only argon flows through the cell. At the same time the He-carrier gas fills the sample loop until the gas composition in the sample loop is the same as in the sample container. In position 2 argon flows through the sample loop and transfers the He/sample-mixture to the test cell.

Behind the test the gas flow is split: a constant fraction is analyzed by a mass spectrometer and the rest is transferred to a fore-vacuum pump. By adjusting the capillary diameter and the capillary

length between the cell and the fore-vacuum pump, it is possible to vary the fraction that is analyzed by the MS. With increasing capillary diameter, the deposition rate of the sample gas increases. It was tried to optimize the gas flow with respect to the retention time of the sample gas (preferably big diameter) and the sensitivity of the mass spectrometer (preferable small diameter). The branching ratio f_{br} of the gas flow, detected in the MS ($Q_{x,det}$) and to the fore-vacuum pump ($Q_{x,FV}$) is not known in most cases and thus an internal standard (He-carrier gas) is used.

$$f_{br} = \frac{Q_{x,det}}{Q_{x,FV} + Q_{x,det}} \quad (6.68)$$

For each solvent a calibration measurement was done prior to deposition. Knowing the vapor pressure of the solvent in the sample container and the volume of the sample loop, the number of molecules in moles n_{SG} can be calculated by

$$n_{SG} = \frac{p_{SG} * V_{sample loop}}{RT} \quad (6.69)$$

The analog expression for the number of molecules of the carrier gas helium n_{He} gas is

$$n_{He} = \frac{p_{He} * V_{sample loop}}{RT} \quad (6.70)$$

In the calibration measurement the complete content of the sample loop was directly transferred to the mass spectrometer. The He-carrier gas and the sample gas signal were recorded over time and by integration over time the charge Q_{He} and Q_{SG} could be correlated with number of molecules n_{SP} and n_{He} in the sample loop.

$$k_{He} = \frac{n_{He}}{Q_{He}} \quad \text{and} \quad k_{SG} = \frac{n_{SG}}{Q_{SG}} \quad (6.71)$$

The factors of proportionality k_{He} and k_{SG} were then used in all subsequent experiments. It should be noted that Q_{he} and Q_{SG} are pressure-dependent and equation 6.71 is only valid if the pressure is constant in the MS.

In the experiment the content of the sample loop is transfered through the cell. Depending on the speed of the gas flow, most or all of the sample gas molecules adsorb on the TiO_2-surface, but none of the He-carrier gas, so the fraction of sample gas molecules significantly deplete behind the cell.

Since the interaction of helium with the cell surface is negligible, the branching ratio f_{br} in equation 6.68 can be calculated using 6.70 and 6.71.

$$f_{br} = \frac{Q_{He,det}}{\frac{p_{He} * V_{sample\ loop} * k_{He}}{RT}} \quad (6.72)$$

With 6.69, 6.71 and 6.72, the number of absorbed molecules $n_{SG,ab}$ is

$$n_{SG,ab} = \left(\frac{p_{SG} * V_{sample\ loop}}{RT * k_{SG}} - \frac{Q_{SG,det}}{f} \right) * k_{SG} \quad (6.73)$$

The only input parameter in equation 6.73 is the vapor pressure p_{SG}, which is 23 hPa (water), 59 hPa (ethanol) and 97 hPa (acetonitrile) according to the Merck ChemDat database.

Prior to each measurement the cell was kept at 50 °C for 24 h at 10^{-5} mbar to remove any solvent on the surface. The deposition of the solvents was done in successive steps. After each deposition step, the short circuit current and the open circuit potential was measured to evaluate the photovoltaic performance. The measurement was done in situ. The illumination source was a red LED, the light intensity was about 0.7 sun. For each solvent a standard NSCSC was used according to the procedure described in chapter 5. As a counter electrode a thin film of carbon was evaporated on the TiO_2 (film thickness: 50 nm), which is assumed to have lower surface area compared to the dip-coated carbon glue (film thickness: 6-30 μm). This is important since one underlying assumption of deposition technique is that the sample gas deposits only on the TiO_2 surface.

The I_{SC} and the V_{OC} measurements were repeated five times within 30 min for each deposition step

to monitor if the values change over time. Since no significant change was found the mean value was taken. As can be seen in Fig. 6.49, similar trends are observed for all solvents. For a low solvent loading (0-3 nmol/cm²) the increase of V_{OC} and I_{SC} is modest. Between 3-5 nmol/cm² a sharp increase is found both for the V_{OC} and the I_{SC} and for a solvent loading > 5 nmol/cm² a constant increase for the I_{SC} is found whereas the V_{OC} remains almost constant. Water and ethanol, which are protic solvents performed better than acetonitrile as an aprotic solvent. This observation was made for other solvents as well: the polarity of the solvent was found to have no influence on the photovoltaic performance whereas a protic hydrogen atom can significantly enhance both V_{OC} and I_{SC} in NSCSC. It is believed that the protic environment can reduce the activation energy for the electron transfer to the oxidized dye molecule.

In the case of water the amount in mol/cm² was converted to the number of monolayers using equation 6.67. Comparing the values found in Fig. 6.49 with the initial performance where the cell was kept at 60 % relative humidity (22 °C) for 24 h, it turned out that about 6 monolayers are present in a cell that is equilibrated with the ambient atmosphere. That corresponds to a pore filling of about 33 %. The pore filling is defined by the ratio of the volume, which occupied by the water, and the total volume of the pores in the nanoporous TiO_2-layer.
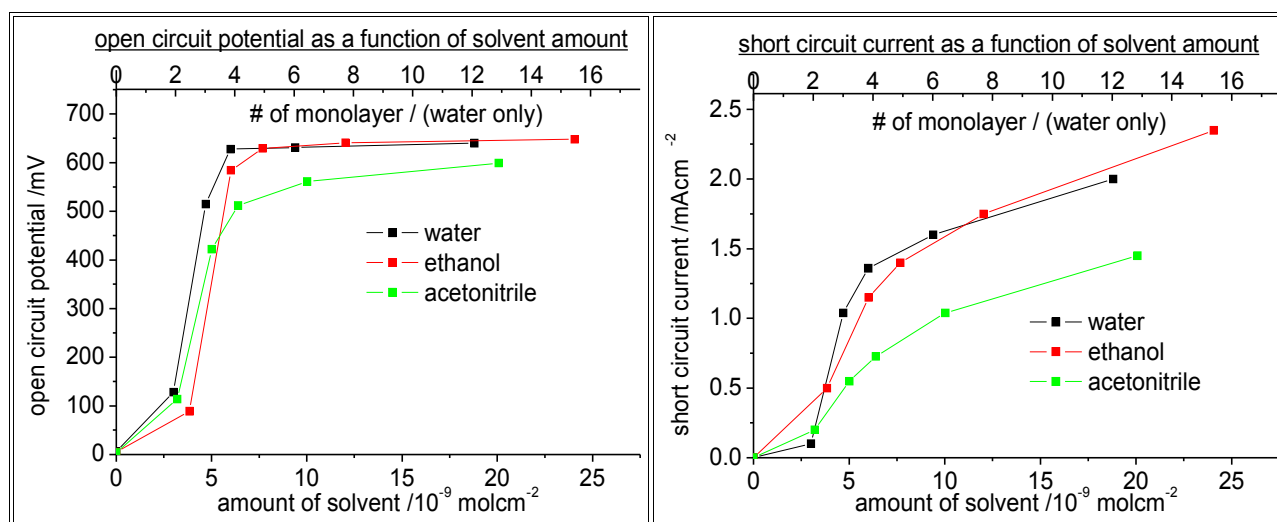
Fig. 6.49: a) open circuit potential and b) short circuit current for different amount of solvent on the TiO_2-nanoparticles; illumination: halogen lamp (ca. 70 mWcm⁻²)

Finally it was checked if the solvent deposition is a reversible process. The solvent desorption (10^{-5} mbar, 50 °C, 24 h) and deposition (3-25 nmol) was repeated three times and the open circuit potential and the short circuit current were recorded as described in the previous section. No

significant trend was observed for the short circuit current with a relative large error of about 20 %. The open circuit potential decreased by 30 mV (water), 45 mV (ethanol) and 28 mV (acetonitrile) after the third cycle indicating that the recombination rate constant has increased or the position of the Fermi level has decreased.

To summarize it was shown that traces of a solvent (water, ethanol, acetonitrile) can significantly increase the photovoltaic performance of the NSCSC and a deposition technique was developed that allows the quantification of the amount of solvent on the nanoporous TiO_2-particles.

6.4.5 Recombination at the TiO_2/electrolyte film interface

In chapter 6.4.3 it was demonstrated that the recombination rate limits the conversion efficiency of NSCSCs. In this chapter strategies are introduced that can help to slow down the recombination rate. This includes the adjustment of the pH, the passivation of the TiO_2/electrolyte interface with rectifying organic compounds, the deposition of white band gap semiconductors on the TiO_2-nanoparticles (core/shell concept) and the introduction of a solid TiO_2-layer on the FTO substrate.

adjustment of pH

It is known from the literature that the flat band potential of nanoporous TiO_2 depends on the pH of the electrolyte [127][135]. In aqueous solution a Nernstian-type pH-dependence is found [127]. With increasing acidity, the flat band potential is shifted electrochemically more positive, which increases the driving force for electron injection. At the same time the potential difference between the conduction band of the TiO_2 and the electrolyte, which determines the open circuit potential, decreases.

Usually, the deposition of coadsorbents, which changes the pH, also alters the recombination rate of conduction band electrons with the electrolyte. For example, the well-known 4-*tert*-butylpyridine both reduces the recombination rate and shifts the flat band potential electrochemically more negative [137][197]. A slower recombination rate also increases the V_{OC}. In general, the change of the V_{OC} is determined both by the recombination rate and the position of the flat band potential. There are examples (guanidinium [198]), where a slower recombination rate compensates the downward shift of the TiO_2 conduction band and a net increase of the open circuit potential is

observed. Since theoretic predictions for the optimal pH are difficult, it has to optimized for each electrolyte/dye composition individually.

LiI /mol*l^{-1}	I$_2$ /mol*l^{-1}	HI /mol*l^{-1}	TBP /mol*l^{-1}	cell assembly	acidity
0.8	0.05	0.2	0.5	50 µl of the electrolyte (solvent: ethanol) were spread on the cell surface with a pipette. The cell was kept at 10^{-5} mbar for 30 min to remove the solvent.	↓
0.6	0.05	0.4	0.5		
0.5	0.05	0.5	0.5		

Table 6.4: electrolyte composition

In a standard NSCSC-cell with the N719-sensitizer, the impact of the pH on the solar cell parameters was scrutinized. The ionic strength in each cell was kept constant. The concentration of the electrolyte components is only given for the precursor solution (table 6.4) and was not determined within the pores.

As can be seen in Fig. 6.50, the I-V-curves basically follow the predicted trend. With increasing acidity the open circuit potential decreases from 646 mV to 365 mV while the short circuit current increases from 0.37 mAcm^{-2} to 0.84 mAcm^{-2}. The net effect was a better overall cell efficiency with increasing acidity.

amount of HI /mol*l^{-1}	efficiency / %	V_{OC} /mV	I_{SC} /mAcm^{-2}	FF /
0.2	1.23	646	0.37	0.51
0.4	1.54	402	0.60	0.64
0.5	1.71	365	0.84	0.56

Fig. 6.50: I-V-curve and solar cell parameters of NSCSCs with different pH of the electrolyte; illumination source: white halogen lamp (10 mWcm^{-2})
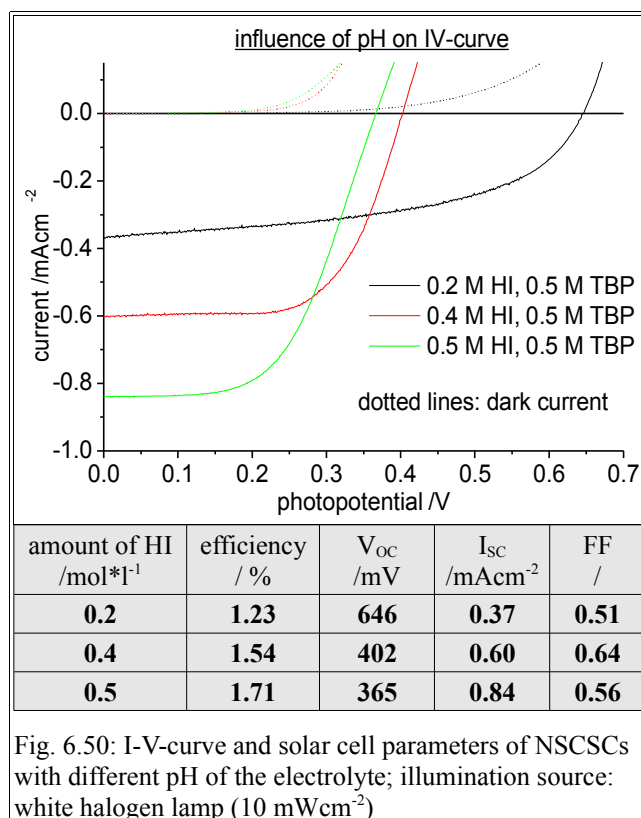
Moreover the ester linkage of the dye to the TiO$_2$ was found to be stabilized in the more acidic environment. In general the ester linkage saponifies in alkaline aqueous solution irreversibly. This problem is found to be less crucial in the supersaturated electrolyte film of the NSCSC, but after some days detached dye molecules can be detected in the electrolyte with UV/Vis-spectroscopy. In the more acidic environment (0.5 M HI, 0.5 M TBP) no detached dye was found indicating that saponification does not take place at all or that the equilibrium constant is very small.

Finally by varying the HI/LiI-ratio the hygroscopicity of the system changes. By visual inspection it can be seen that less water is attracted if more HI is added to the electrolyte and that the electrolyte tends to crystallize. The efficiency of a cell, in which the electrolyte has crystallized, was about one order of magnitude less. By increasing the relative humidity the salts start to melt again. For the cell containing 0.5 M HI and 0.5 M TBP the melting point was at 65 % relative humidity (22 °C). For this reason the I-V-curves were taken after the cells were exposed to an atmosphere with 70 % relative humidity (22 °C).

organic coadsorbents

The second approach to slow down the recombination rate was to use organic coadsorbents. Besides the standard coadsorbent TBP, mercaptans and carboxylic acids were tested. Mercaptans have been investigated as rectifiers in bioelectric system for a long time and significant progress has been made towards organic diodes [199][200]. In DSSC these molecules have not been utilized so far, however, the asymmetric oxidation/reduction of the thiol group make them promising candidates as coadsorbents.

Carboxylic and phosphonic acids have a long history in DSSCs as coadsorbents. Although they are known to decrease the dye uptake by up to 30 % [201], the initial performance is not necessarily lower compared to the untreated reference cell and the long term stability is significantly enhanced for some dye/electrolyte combinations. Especially the open circuit potential, which is a measure for the recombination rate and the flat band position, remains remarkably stable even under elevated temperature (80 °C) [194]. Since the standard molecules used, decylphosophonic acid (DPA) and hexadecylmalonic acid (HDMA), are solids with negligible vapor pressure, more volatile compounds were tested in this study.

The molecules were deposited using the gas deposition apparatus introduced in chapter 6.4.4. The vapor pressure, the deposition amount and the effect both on short circuit current and open circuit potential are listed in table 6.5.
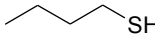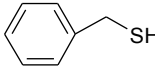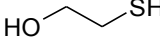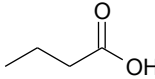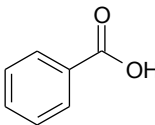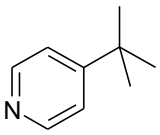
name	structure	vapor pressure /hPa	boiling point /°C	deposition amount /nmol	$V_{OC}/V_{OC,Ref}$ / %	$I_{SC}/I_{SC,Ref}$ /%
1-butanthiol		110.39	97-99	3.6	+10	-18
				14.2	± 0	-43
benzyl-mercaptan		0.5	195-195	0.13	+ 11	- 5
				0.52	+ 19	+ 8
2-mercapto ethanol		1	154-161	0.13	+ 5	+ 16
				0.52	+ 6	+ 8
propionic acid		5	141	0.65	-1	+ 9
				2.1	- 18	+ 17
benzoic acid		0.013	249	$1.7*10^{-3}$	- 1	+ 6
				$6.8*10^{-3}$	- 4	- 5
4-*tert*-butyl pyridine (TBP)		3	194-197	0.39	+ 17	+ 5
				1.56	+ 16	- 8

Table 6.5: influence of coadsorbents on short circuit current and open circuit potential; illumination source: red LED, light intensity: ca. 70 mWcm^{-2}

In the study the I_{SC} and V_{OC} of a standard NSCSC was measured directly before and after the deposition of the coadsorbent. The relative changes are given in table 6.5. Within the mercaptans, benzylmercaptan (0.52 nmol deposition on 1 cm^2 active cell area) and 2-mercaptoethanol (0.13 nmol) were found to significantly increase the conversion efficiency. For benzylmercaptan the increase was mainly due to a higher V_{OC} (+19 %) and for 2-mercaptoethanol due to a higher I_{SC} (+16 %). This initial screening did not aim to determine the effect of the coadsorbent on the recombination rate and the flat band potential. This information can be get by photovoltage transient measurements and will be part of upcoming studies to relate the structure of the molecule with the effect on I_{SC}/V_{OC}.

The optimal deposition amount depends on the affinity of the coadsorbent to the TiO$_2$, its electronic properties and its sterical demand. In this semiquantitative study, only two different concentrations were investigated, which were mainly determined by the length of the sample capillary. Thus it is

doubtful, that the optimal concentration were used. For example, substances with high vapor pressure like 1-butanthiol could only be applied in relative large amounts, which had a negative effect on the conversion efficiency. Whereas the decrease after the deposition of 3.6 nmol was modest (V_{OC} +10 %, I_{SC} -18 %), it was significant after the deposition of 14.2 nmol ($V_{OC} \pm 0$, I_{SC} -43 %). Smaller capillaries are needed to investigate the effect in the sub-nanomol regime.

The carboxylic acids could not significantly increase the performance of the NSCSC. Due to their acidic nature the open circuit potential typically decreased, which was partly or completely compensated by a higher I_{SC}. Propionic acid in a concentration of 0.65 nmol on 1 cm² active cell area gave the best result with + 9 % short circuit current and about the same open circuit potential (-1 %).

TBP, which is the standard coadsorbent in liquid DSSC [137][202], had a positive effect on the NSCSC. In low concentration (0.39 nmol/cm²) an increase of 17 % of the open circuit potential and 5 % of the short circuit current was observed.

To summarize it could be demonstrated that already with a small screening of some organic compounds the efficiency of the NSCSC could be significantly enhanced. The deposition method is very flexible and applicable to any volatile chemical compound, which opens the window to millions of other organic compounds. It is believed that combinatorial chemistry might play a key role in the future development of NSCSC.

core/shell concept

The third approach tried to exploit the core/shell concept, which has been successfully applied for DSSCs [126][180][203][204]. The idea is to passivate the nanoporous TiO_2 particles with a wide bandgap semiconductors, which might enhance the open circuit potential in three ways:

1) The wide bandgap semiconductor acts as a tunnel barrier at the TiO_2/electrolyte interface and directly reduces the recombination rate. If the electron injection rate remains unchanged, the electron concentration under steady state condition will be higher for the cell with the coating. A larger electron concentration in the TiO_2 conduction band shifts the quasi Fermi level upward and thus a larger V_{OC} is measured.

2) The surface coating changes the distribution of charges across the TiO_2/electrolyte interface. If negative charges accumulate on the TiO_2 surface and deplete on the electrolyte side, then the resulting electric field will increase the band offset between the two materials and thus
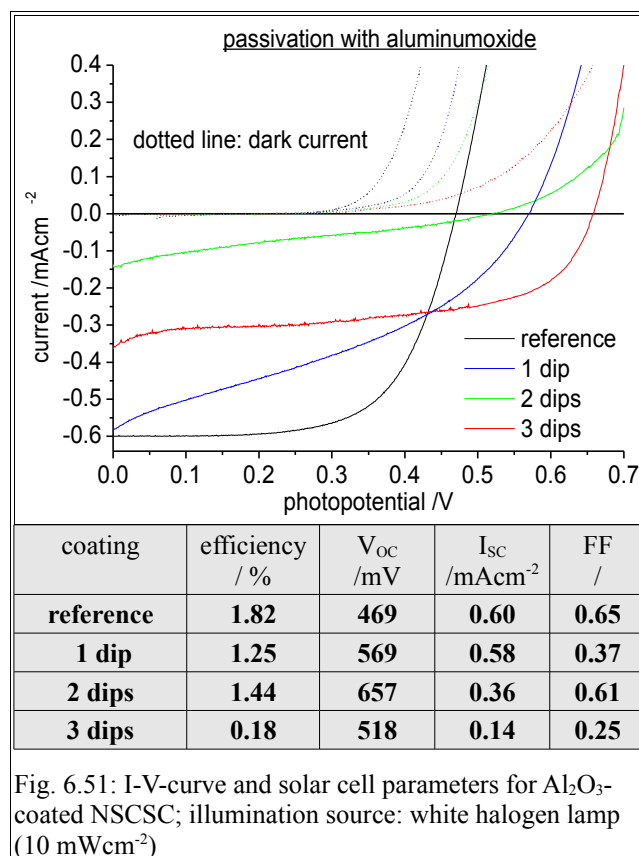
increase the V_{OC}.

3) The coated semiconductor might passivate surface trap states in the TiO_2. This can directly decrease the recombination rate since surface trap states are the dominant recombination sites.

Typical semiconductors applied are Al_2O_3 ($E_g = 9$ eV), ZrO_2 (5 eV) and SiO_2 (8.5 eV). Al_2O_3 so far gave the best results as it is known to suppress the recombination rate very effectively. Al_2O_3-coatings were both applied in liquid systems [203][204] and systems with solid hole conductors [180]. So far it could not be demonstrated that a metal oxide coating can increases the performance of a highly efficient DSSC (> 8 %). But if solid state hole conductors with a high recombination rate are applied, it was found that the efficiency can improve by up to 15 %. For this reason it was scrutinized if metal oxide blocking layers can enhance the efficiency of NSCSCs. The deposition is done by dip-coating [203]:

A 0.1 M solution of aluminum-tri-*tert*-butoxide in dry propan-2-ol was prepared in a glove box. All further steps were done under ambient atmosphere, since the diluted precursor solution is less susceptible to oxygen. The TiO_2-film was immersed into this solution for 15 min at 50 °C. Then it was immediately rinsed with ethanol and fired at 450 °C for 30 min. The deposition cycle can be repeated several times. The coating increased by ca. 2 nm per cycle.

Fig. 6.51 shows the I-V-curves of Al_2O_3 passivated NSCSCs. The cell assembly followed the general procedure introduced in chapter 5. It can be seen that with increasing thickness of the Al_2O_3-coating, the open circuit potential increased and the short circuit current decreased. After three dipping cycles, the V_{OC} increased by 191 mV compared to the reference cell. At the same time short circuit current decreased by almost 33 % and the overall conversion efficiency could not be improved. It can be concluded that the Al_2O_3-coating in a NSCSC slows down both the recombination rate and the injection rate. As a consequence the gain in the V_{OC} due to a slower recombination rate is completely compensated by a lower IPCE.

The fill factor varied significantly and no correlation to the number of dips was found. The measurement of photocurrent transients revealed, that the charge extraction in the coated films was significantly slower, however, the reproducibility of the data was poor. A lower fill factor can be attributed to the higher charge transport resistance in the film. It is reasonable to assume different transport kinetics for positive charge carriers on the coated substrates.

Fig. 6.51: I-V-curve and solar cell parameters for Al_2O_3-coated NSCSC; illumination source: white halogen lamp (10 mWcm^{-2})

coating	efficiency / %	V_{OC} /mV	I_{SC} /mAcm^{-2}	FF /
reference	1.82	469	0.60	0.65
1 dip	1.25	569	0.58	0.37
2 dips	1.44	657	0.36	0.61
3 dips	0.18	518	0.14	0.25

Besides Al_2O_3, ZnO and MgO were tested as metal oxide coatings. However, both V_{OC} and I_{SC} were significantly lower for the coated cells, which gives some indication that the core/shell concept is less suitable for NSCSC compared to other DSSC-derivatives. The main problem seems to be that the metal oxide coating not only slows down the recombination rate, but also the charge injection rate and the transport kinetics of positive charge carriers.

Improving both the recombination rate and the transport of positive charge carriers with the same treatment needs probably a chemically more sophisticated approach. One interesting investigation would be to combine the core/shell concept with the deposition of organic coadsorbents.

compact TiO$_2$-layer

Finally the effect of a compact TiO_2-layer on the FTO-substrate was tested. In general, electrons can recombine both from the conduction band of the nanoporous TiO_2 and from the FTO substrate. Depending on the electrolyte/HTM-composition, the kinetics for both recombination reactions might differ by several orders of magnitude.

In a standard liquid DSSC with an I_3^-/I^--electrolyte, the recombination rate at the FTO/electrolyte

interface is believed to be negligible. Although the exchange current especially near open circuit potential might be faster compared to the TiO_2/electrolyte interface, the area of the interface is about three orders of magnitude smaller. There are studies that indicate that a compact blocking layer might improve the solar cell efficiency [175][205], but in highly efficient liquid DSSCs, blocking layers are usually not applied. The situation is different if other redox couples or solid hole conductors with a very fast recombination rate at the FTO/TiO_2 interface are applied.

For example, Co^{II}/Co^{III}-complexes are used as a redox mediator in liquid DSSCs. In these devices the exchange current at the FTO/electrolyte interface is about $7*10^{-6}\,Acm^{-2}$ and therefore about two orders of magnitude higher compared the I^-/I_3^--redox system [206]. In this case a compact TiO_2-blocking is crucial for the functioning of the cell. The same is true for DSSCs using spiro-OMeTAD [185] or CuSCN [180] as the hole conducting material.

The passivation of the FTO-substrate with a compact TiO_2-layer was used in NSCSCs to distinguish qualitatively between recombination at the FTO/electrolyte interface and at the TiO_2/electrolyte interface. The deposition of the compact layer was done by spray pyrolysis. The FTO-substrate was placed on a hot plate at 450 °C. Then a solution of 0.2 M titanium di-isopropoxide-bis(acetylacetonate) in ethanol was sprayed onto the substrate in pulses of about 2 - 5 seconds. Depending on the number of spray cycles, compact layers with a thickness between 20 - 150 nm were made. Fig. 6.52b shows the height of the layer used in this study, which was 89 nm ± 10 nm.
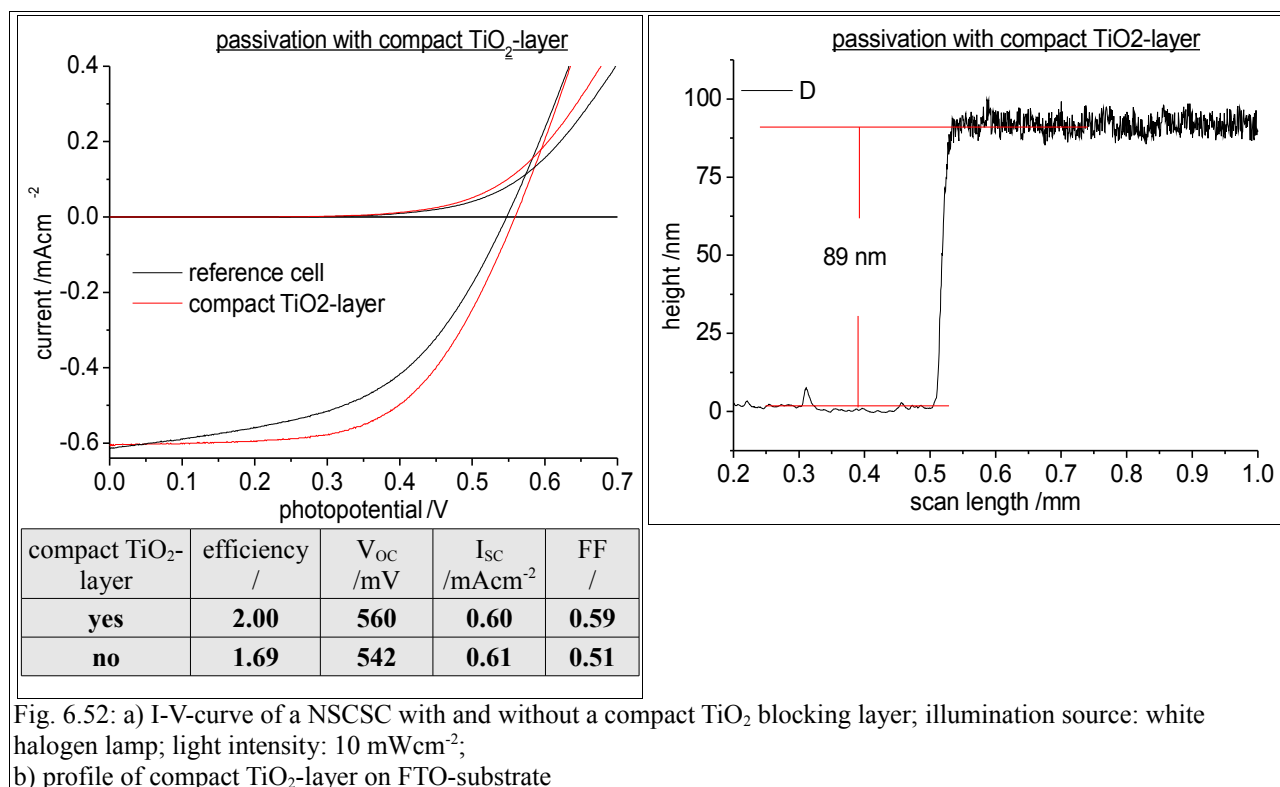
Fig. 6.52: a) I-V-curve of a NSCSC with and without a compact TiO_2 blocking layer; illumination source: white halogen lamp; light intensity: 10 mWcm^{-2};
b) profile of compact TiO_2-layer on FTO-substrate

compact TiO_2-layer	efficiency /	V_{OC} /mV	I_{SC} /mAcm^{-2}	FF /
yes	**2.00**	**560**	**0.60**	**0.59**
no	**1.69**	**542**	**0.61**	**0.51**

The I-V-curve of the passivated cell and the reference cell is shown in Fig.6.52a. It can be seen that the conversion efficiency of the cell with a TiO_2-blocking layer increased about 18 % compared to the reference cell, which was mainly due to a better fill factor. That indicates that the recombination rate at the FTO/electrolyte interface is significantly higher in NSCSCs compared to liquid DSSCs and that a compact TiO_2-underlayer can effectively slow down the recombination rate.

6.4.6 The TiO_2/counter electrode interface

In this chapter different counter electrode materials/deposition techniques are discussed. The standard procedure involves the deposition of a suspension of carbon conducting glue/carbon nanoparticles by the doctor-blade method, which is described in chapter 5. In the following section the evaporation of carbon, the use of platinized FTO-substrates and the evaporation of a thin gold film on the TiO_2 nanoparticles are discussed.

The deposition of the carbon counter electrode with the doctor-blade method has an inherent disadvantage. The carbon particles in the suspension form big agglomerates and after the evaporation of the solvent, the layer is punctured by big holes in the micrometer range. This is especially critical if the contact between the TiO_2 and the counter electrode material is interrupted. Since electrons can only move on the surface of a solid substrate, no dye regeneration is possible in the TiO_2-layer under the hole. As can be seen in Fig. 6.53, the holes might be as big as 3 * 15 µm. As a consequence, the short circuit current and the fill factor in NSCSCs with a poor carbon-layer/TiO_2 interface were found to be significantly lower.
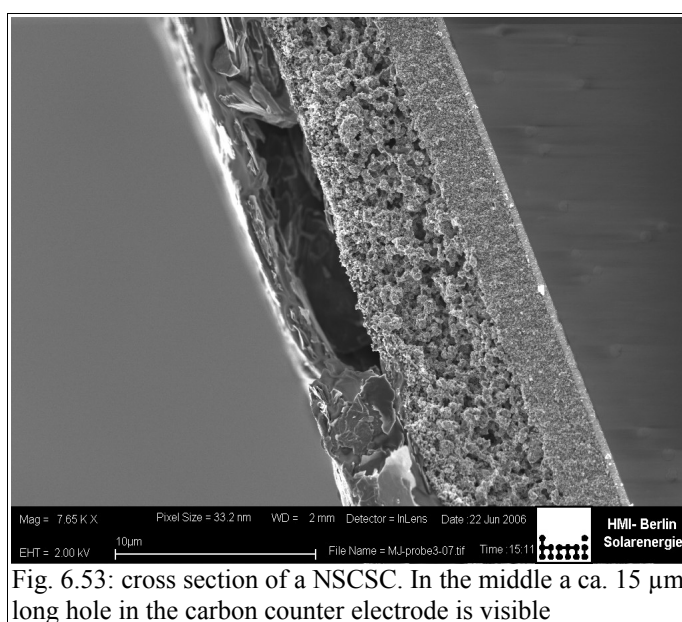
Fig. 6.53: cross section of a NSCSC. In the middle a ca. 15 µm long hole in the carbon counter electrode is visible

Much effort was undertaken to minimize the formation of holes, and some parameters have been identified that play a critical role:

1) **the viscosity of the carbon-suspension**

By adding more solvent, the viscosity of the suspension decreased and the carbon layer became more uniform. At the same time, the number of deposition cycles for a given layer thickness had to be increased.

2) **homogenization of the carbon suspension**

With increasing time of ultrasonic treatment, the suspension became more homogeneous and the agglomerates could be downsized. However, for an exposure > 90 s, no further improvement was observed.

3) **additives**

Surfactants like Triton X were found to minimize the hole formation in the layer. However, since they have a negligible vapor pressure, they could not be removed afterwards. That greatly decreased the catalytic activity of the carbon layer, which is the reason why the addition of surfactants is not part of the standard process.
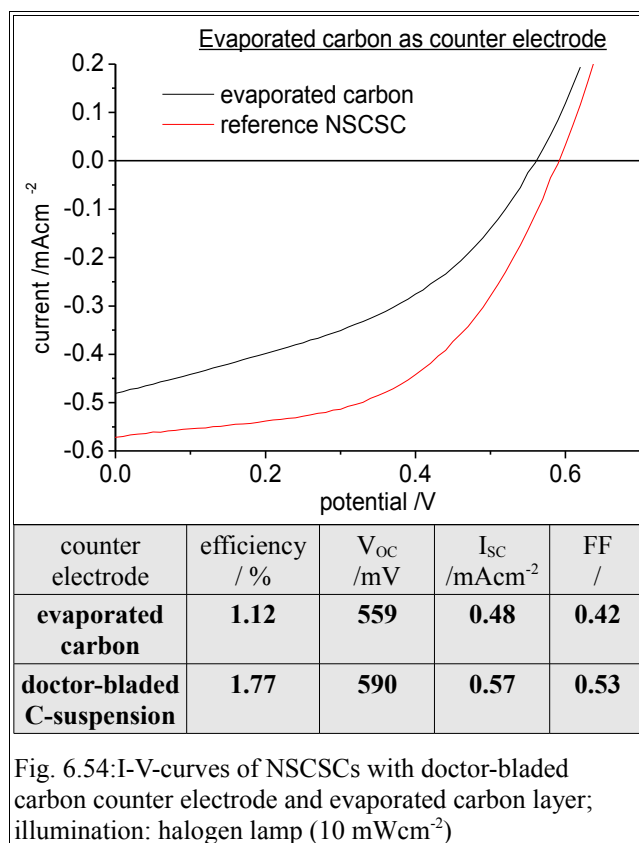
Although the hole formation could be greatly decreased, it was not possible to suppress it completely. Besides the negative effect on I_{SC} and FF, the reproducibility of solar cell parameters was found to be difficult. The properties of the carbon layer varied in terms of layer thickness, catalytic activity and average pore size.

For this reason it was tried to deposit the carbon by evaporation. The sensitized TiO_2-films were placed in a high vacuum chamber at $2*10^{-6}$ mbar. A thin carbon wire was placed above the sample and connected to a power supply. By applying high currents the carbon wire heated up and started to evaporated. The carbon condensated in the cooler surroundings and deposited on the underlying TiO_2-film. The thickness of the layer was mainly a function of the mass of the carbon wire, the distance of the sample to the wire and the pressure within the chamber. For the parameters used, the carbon layers had a thickness of 20 nm.

The composition and deposition of the electrolyte is described in the general procedure in chapter 5. Fig.6.54 compares the I-V-curves of a doctor-bladed carbon counter electrode and an evaporated carbon film. First of all it was interesting to note that the NSCSC with the evaporated carbon layer worked without an insulator between the TiO_2 and the carbon film. The carbon film was directly evaporated on the sensitized TiO_2-film. Thus, the only rectifying spacer at the TiO_2/carbon interface was a monolayer of dye molecules. This close proximity was believed to enhance the recombination rate of conduction band electrons to the carbon film either by tunneling or through non-sensitized points on the TiO_2.

Evaporated carbon as counter electrode

counter electrode	efficiency / %	V_{OC} /mV	I_{SC} /mAcm^{-2}	FF /
evaporated carbon	**1.12**	**559**	**0.48**	**0.42**
doctor-bladed C-suspension	**1.77**	**590**	**0.57**	**0.53**

Fig. 6.54:I-V-curves of NSCSCs with doctor-bladed carbon counter electrode and evaporated carbon layer; illumination: halogen lamp (10 mWcm^{-2})

Moreover due to the high density of states in the carbon, a direct charge injection from the dye into the carbon should be possible. The question arises why this pathway, though thermodynamically feasible, is not a serious impediment for charge separation. The reason for that is probably related to the nature of the redistribution of electron density in the dye in the excitation process. The excitation initiates a shift of electron density towards the ligands, by which the dye is adsorbed to the TiO_2 surface. The ultrafast electron injection into the TiO_2 is apparently rapid enough to provide a selective injection to the TiO_2 and not to the carbon.

So a reasonable conversion efficiency of 1.12 % was achieved. The open circuit potential was only 30 mV less compared to the reference cell. The lower efficiency was mainly due to a poor fill factor (0.42) and a low short circuit current. This is attributed to the relatively small surface area of the compact carbon layer, which reduces its catalytic activity. With a lower exchange current density at the carbon/electrolyte interface, an overpotential builds up at the counter electrode, which reduces both FF and I_{SC}. By varying the layer thickness of the carbon layer (5 nm, 10 nm, 20 nm), it could be seen that the fill factor decreased from 0.42 (20 nm) to 0.31 (5 nm) and the short circuit current from 0.48 mAcm^{-2} (20 nm) to 0.38 mAcm^{-2} (5 nm).

It was not possible to increase the carbon layer thickness > 20 nm with the apparatus used. It would
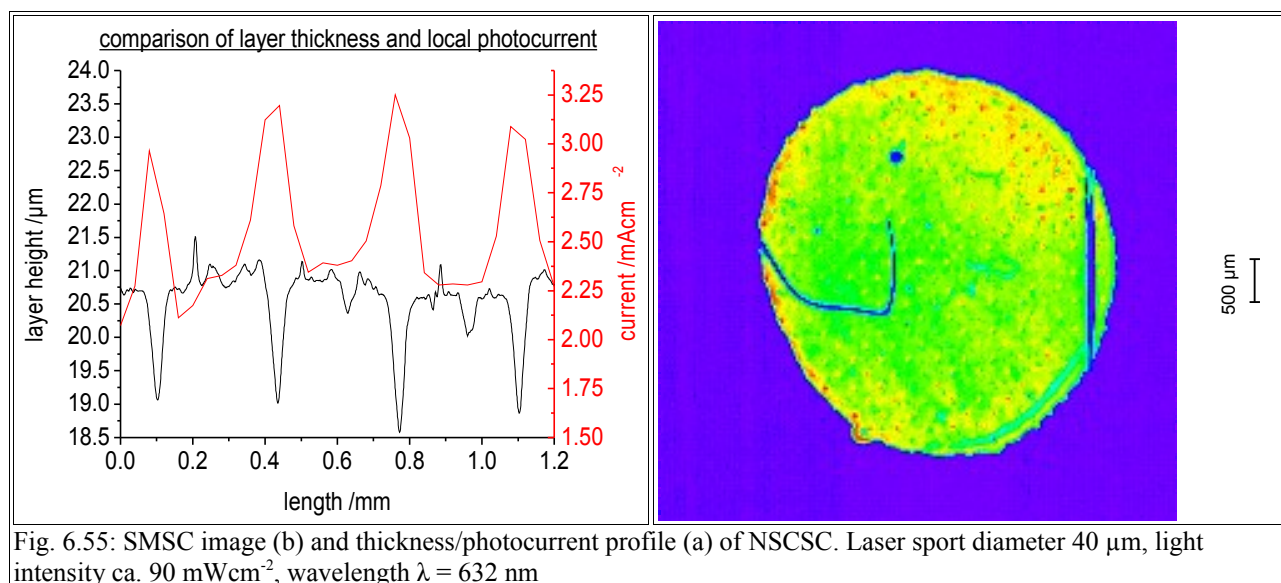
have been interesting to test if the fill factor and short circuit current could be further enhanced by increasing the thickness of the carbon layer. However, it is unlikely that much improvement would have been achieved for the following reason: The carbon layer is compact and if it exceeds a certain thickness it will plug the pores in the TiO_2-film. In this case the deposition of the electrolyte and the water exchange with the atmosphere can only occur at the border of the active cell area, which is believed to be not sufficient.

Compared to a standard NSCSC with a doctor-bladed carbon electrode, the deposition of carbon by evaporation proved to be less efficient. However, the reproducibility of solar cell parameters was much better and the deviation was usually < 10 %. If the surface area of the carbon film can be increased, it might be a considerable alternative to the doctor-blade method.

This might be achieved by employing a roughened TiO_2 film. For example, small holes can be introduced into the TiO_2-layer if a more viscous paste is used for the screen printing. A thickness profile of such a layer is given in Fig. 6.55a. In a space-resolved photocurrent image of a NSCSC with a punctured TiO_2-layer one can see small dots, where the local photocurrent is significantly higher compared to the surrounding (Fig. 6.55b). If one makes a cross section of the two-dimensional photocurrent image and correlate it with the thickness profile (Fig. 6.55a), one can see that the local photocurrent is up to 30 % higher at the place, where the holes are. The area of the carbon/electrolyte interface is enlarged in theses parts, which increases the catalytic activity. As a result, the overpotential for the iodine reduction decreases and the short circuit current increases.

This effect is not seen in NSCSC with a doctor-bladed counter electrode, because the carbon particles are too big to penetrate the small holes.
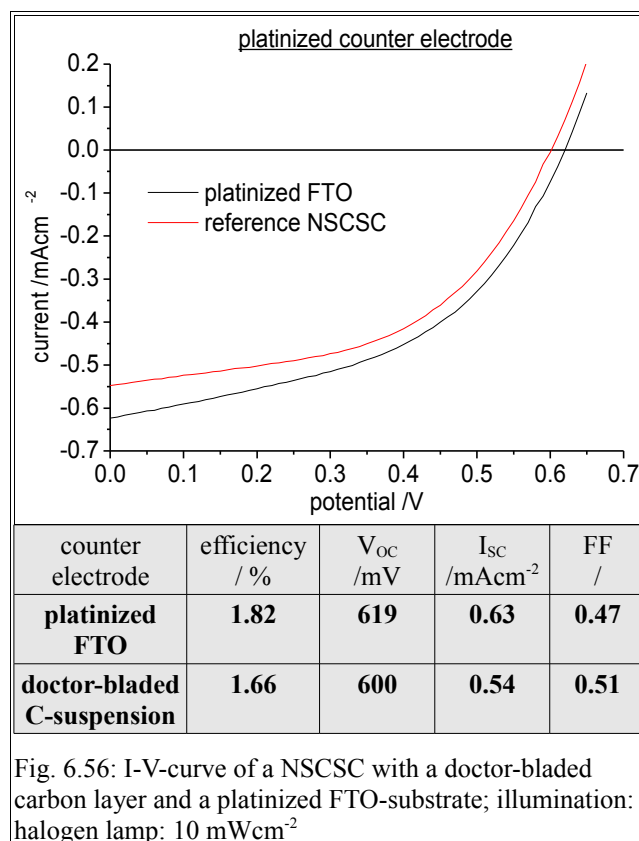
Fig. 6.55: SMSC image (b) and thickness/photocurrent profile (a) of NSCSC. Laser sport diameter 40 µm, light intensity ca. 90 mWcm^{-2}, wavelength $\lambda = 632$ nm

The experiments with an evaporated carbon film on the TiO$_2$ have demonstrated, that a monolayer of dye molecules can effectively rectify the electron current. However, the catalytic activity of the carbon film was insufficient. For this reason, it was tried to use platinized FTO-substrates as the counter electrode, which have a higher catalytic activity. The preparation of the counter electrodes was done according to the procedure described in chapter 5.4.1.

The platinized counter electrode was directly pressed on the sensitized TiO$_2$-film, on which a thin electrolyte film was already deposited (according to the procedure in chapter 5.5). A NSCSC with a platinized FTO-substrate exhibited a 9.6 % higher conversion efficiency compared to a NSCSC with a doctor-bladed carbon counter electrode (Fig. 6.56), which is due to a higher short circuit current and a higher open circuit potential. Mainly two explanation have been identified for the improved performance:

1) the electrode spacing in a standard NSCSC is about 25 - 28 µm (ca. 10 µm TiO$_2$, 15 - 18 µm carbon layer), but for the NSCSC with a platinized FTO-counter electrode the spacing is only 11 - 12 µm. That decreases the average path length, that an electron/hole has to diffuse and thus a lower series resistance is expected.

2) The catalytic activity of the platinum is higher compared to carbon, which decreases the overpotential at the counter electrode.

Fig. 6.56: I-V-curve of a NSCSC with a doctor-bladed carbon layer and a platinized FTO-substrate; illumination: halogen lamp: 10 mWcm^{-2}

counter electrode	efficiency / %	V_{OC} /mV	I_{SC} /mAcm^{-2}	FF /
platinized FTO	**1.82**	**619**	**0.63**	**0.47**
doctor-bladed C-suspension	**1.66**	**600**	**0.54**	**0.51**

Despite the better initial performance, it was found that the NSCSCs with platinized FTO-counter electrodes degrade much faster compared to standard NSCSCs. Most likely some of the platinum dissolves from the counter electrode and diffuses into the TiO$_2$-film, where it drastically enhances the recombination rate.

As a conclusion platinized FTO-substrates were found to enhance the initial conversion efficiency. But since the long term stability even at room temperature is very poor due to Pt-desorption, this method is only applicable if the adhesion of the platinum to the FTO-substrate can be improved.

Finally it was tried to sputter a compact Au-film directly onto the TiO$_2$. A study from Lenzmann *et al.* has demonstrated that gold can be used to regenerate the oxidized dye in a DSSC with a flat TiO$_2$-layer [207]. In this system, gold replaces both the iodine/iodide-couple as the redox mediator and the FTO-substrate as the current collector. However, this approach does not work with a porous TiO$_2$-layer, since the average path length between the gold electrode to the oxidized dye is several micrometers. It was tested if an I$_2$/I$^-$-electrolyte film like in NSCSC can transfer the electrons from the gold electrode to the oxidized dye. The following advantage was expected:

Gold has a very high conductivity ($47.6*10^6$ S/m), thus it can both catalyze the reduction of iodine and transport the electrons with low resistivity. A second FTO-coated glass would then be redundant, which would simplify the cell assembly significantly.

The gold was evaporated on a porous substrate of TiO_2 with an average particle diameter between 20 - 30 nm. The aim was to create a three-dimensional gold network that allows a lateral electron percolation and an exchange of gases in the vertical direction. In other words the film was designed to be thin enough, that it does not block the porous TiO_2 but thick enough, that an interconnected film with low resistance is formed. First the sheet resistance of gold layers with different thickness was measured on FTO and TiO_2.

	sheet resistance for a Au-layer thickness of ... nm in $\Omega/\square$		
	20	**50**	**100**
solid layer with flat surface (data calculated from the electrical resistivity of Au)	0.011	$4.2*10^{-3}$	$2.1*10^{-3}$
FTO	4.0	1.4	0.7
TiO_2	ca. 400	5.6	3.1

Table 6.6: sheet resistance for Au-layers of 20, 50 and 100 nm on different substrates

As can be seen in table 6.3, the sheet resistance of solid gold-layer is about three orders of magnitude lower compared to the layers deposited on FTO and TiO_2, which can be rationalized in the following way: Generally spoken, the average Au-film thickness on a rough substrate is decreased by a factor χ, which corresponds to the ratio of the projected and the real surface area. More specifically, the Au-layer thickness d is a function of the angle α between the plane of the substrate and the evaporation beam.

$$d = d_0 * \sin \alpha \quad (6.74)$$

d = thickness of Au-layer; d_0=layer thickness on a flat substrate; α = angle between the plane of the substrate and the evaporation beam

If the angle becomes $0\,°$ or the surface is shaded by other particles, the electron percolation is interrupted. For thin Au-layers (< 20 nm) the percolation threshold determines the sheet resistance.

In this case the sheet resistance does not depend on the Au-layer thickness.

For the 50 and 100 nm thick layer, the sheet resistance decreases linearly indicating that enough percolation pathways exist. The sheet resistance is about 4 times higher on the TiO_2 compared to the FTO substrate reflecting that the TiO_2 has a higher roughness factor than the FTO.

The gold-coated TiO_2 was employed in a standard NSCSC according to the procedure in chapter 5.5. A summary of the experiments is given in table 6.7.

layer thickness Au /nm	deposition of the electrolyte	V_{OC}/V (initial)	I_{SC} (mAcm^{-2}) (after 60 s illumination)
20	before the deposition of the gold layer	0.453	0.03
50		0.433	1.96
100		0.396	2.25
20	after the deposition of the gold layer	0.296	0.02
50		0.365	2.08
100		0.356	2.22

Table 6.7: experiments employing a thin layer of gold as the counter electrode. The thickness of the TiO_2 layer was 15 μm.
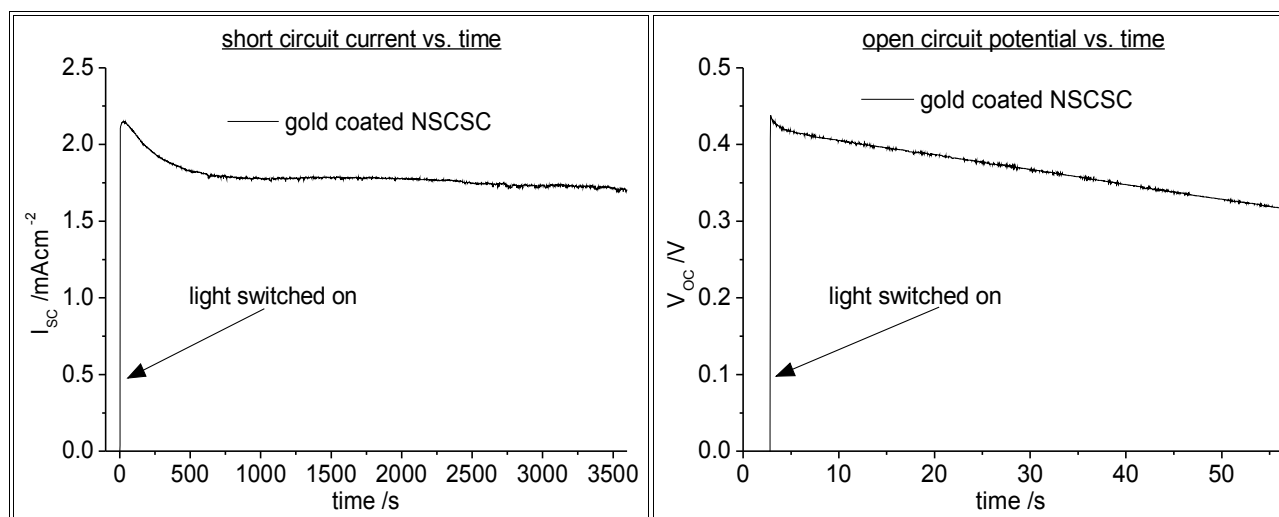

Fig. 6.57: illumination 100 mWcm^{-2}; gold layer: 50 nm thick
a) short circuit current as a function of time; the cell was short circuited before the measurement
b) open circuit potential as a function of time. the measurement was carried out immediately after the cell preparation. The observed decrease of the V_{OC} was irreversible.

Fig. 6.57 shows a typical potentiostatic and galvanostatic measurement for NSCSCs with a gold

coated counter electrode. It can be seen, that within the first 60 s, the open circuit potential decreased linearly by around 100 mV (Fig. 6.57b). The decrease continued (not shown) and after 5 to 10 min the cell potential approached 0 V. By visible inspection it could be seen that the gold layer was corroded after that time and no current was measured under forward or reverse bias indicating that the electrical contact was interrupted. If the NSCSC was partly illuminated and the load resistance was 10 Ω, the corrosion was only observed in the illuminated areas and the corrosion rate was much faster than under V_{OC}. Under a load of 10 Ω, the iodine concentration at the TiO_2/Au interface is higher than under V_{OC}. It can be concluded that gold corrodes only in the presence of iodine and a positive potential at the counter electrode.

At I_{SC}, the cell is fairly stable for at least one hour illumination (Fig. 6.57a). After 500 s± 200 s, a steady value of ca. 1.77 mAcm^{-2} was reached. The measurement (1 hour illumination at RT) was repeated on three consecutive days and no further decrease was observed.

Table 6.7 gives the short circuit current and the open circuit potential for NSCSCs with different Au-layer thickness. For a 20 nm thick Au-layer, a I_{SC} of around 20 - 30 µAcm^{-2} is observed, which is about 2 orders of magnitude lower compared to the I_{SC} of a 50 and 100 nm thick Au-layer (about 2 mAcm^{-2}). The low current is due to the high sheet resistance of the Au-layer (~400 Ω/□). The V_{OC} increased slightly with increasing Au-layer thickness.

To summarize it was found that Au-counter electrodes are stable at I_{SC} and reverse bias but decompose at V_{OC} and forward bias respectively. The question arises, which chemistry leads to the destruction of the gold electrode. The electrolyte basically contains hydrated LiI. The only known binary iodide complexes with gold are AuI, a long zig-zag polymer [208] and AuI_2^- [209][210]. However, both are known to be not stable in water [210].

When exposing a gold coated substrate to a 1 M LiI-solution in water for several days, a blackish precipitate formed, which did not dissolve in HCl or NaOH but in nitrohydrochloric acid. So most likely the precipitate contained small gold particles. As a preliminary model it can be assumed that little amounts of iodine at the counter electrode react with gold to form a Au(I)-complex under forward bias.

$$\boxed{2Au + I_2 + 2I^- \rightarrow 2AuI_2^-} \quad (6.75)$$
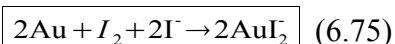
The complex is hydrated and diffuses into the TiO_2-layer. Under this condition it is unstable again and dissociates into the metal and iodine again.

$$\boxed{2AuI_2^- \rightarrow 2Au + I_2 + 2I^-} \quad (6.76)$$
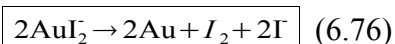
6.4.7 Summary and Outlook

The NSCSC has been introduced as a new type of DSSC, which does not need any sealing and uses atmospheric water as a solvent. The efficiency of 2 % is remarkably high compared to other solid state DSSC devices and long term stability has been proven at room temperature for more than one year. At the moment the high recombination rate and, at higher light intensity, the charge transport within the TiO_2-layer limits the conversion efficiency of the cell. The main advantage of the NSCSC is that the cell is an open system with a percolating network of an electron conductor (TiO_2), an conductor of positive charge carriers (1 - 5 nm thick electrolyte film on top of the TiO_2) and a gas phase that might be used to deposit coadsorbents (s. chapter 6.4.5) or to enhance the conductivity (not realized yet).

The reduction of electron recombination the deposition of coadsorbents is believed to be a very powerful. By means of combinatorial chemistry a large variety of different substances can be tested for their rectifying properties in a very simple manner. The adsorption of substances through the gas phase with the gas deposition apparatus introduced in chapter 6.4.4 allows the uniform deposition of coadsorbents in the 10^{-9} mol range.

The percolating gas phase within the NSCSC might also be used to enhance the conductivity. Chemically inert conductors like carbon nanotubes or transport conducting oxide (TCO) powders (e.g. ITO) might be integrated into the TiO_2-matrix to facilitate electron transport from the counter electrode to the electrolyte film. It would be desirable that these conductors can catalyze the reduction of iodine or polyiodides respectively.

Other approaches might include the variation TiO_2-nanoparticle size. Since the mean length, which a positive charge carrier has to diffuse from the point of generation to the counter electrode in the aqueous electrolyte film does not depend on the radius of the TiO_2-particles but the surface area and thus the recombination rate decreases with increasing radius, bigger TiO_2-particles might be also a tool to enhance the efficiency of NSCSC.

6.5 Accelerated aging tests on dye sensitized solar cells

The long term stability of dye sensitized solar cells has been under a controversial debate in the literature for a long time [211][212][7][194][213][214]. Up to this point no general model for degradation patterns has been agreed on. Several mechanisms are believed to contribute to the overall decline in cell efficiency [212][7], but so far it was not possible to identify the crucial parameters that determine the stability of the device. Even with the same electrolyte/dye combination it was found to be difficult to reproduce the results in different labs [31][194], which raises the question what are the most important processing parameters that might contribute to the different cell characteristics. Up to now it has been agreed on that both light induced degradation of the dye and chemical degradation in darkness contribute to the overall decrease in cell efficiency [211][215].

In this chapter the experiments of a two month research internship at the Energy Center of the Netherlands (ECN) are summarized that aimed to determine crucial parameters for cell stability. The cells were exposed to 80 °C for about 1000 h in average and an ongoing characterization was undertaken.

Besides I-V-measurements the cells were characterized with UV/Vis spectroscopy, impedance spectroscopy, GC-MS and photovoltage/photocurrent transient measurements. The parameters investigated were: water content of the electrolyte (chapter 6.5.2), oxygen treatment of the electrolyte (chapter 6.5.3), TiCl$_4$ post treatment of the TiO$_2$ electrodes (chapter 6.5.4), the purity of electrolyte solvent (chapter 6.5.5) and the cell thickness (chapter 6.5.6).

The studies on the impact of water and oxygen on cell stability were of special importance to assess the potential stability of NSCSC that are introduced in chapter 6.4. It could be demonstrated that water and oxygen do not enhance the degradation of DSSC, which raises hope that the open cell concept of the NSCSC can be a feasible alternative to sealed cells.

For the first time it was demonstrated that DSSCs can pass the 1000 h test at 80 °C in the presence of 5 % water in the electrolyte without any decline in cell efficiency. Other important results include the prove that the enhanced short circuit current of TiCl$_4$-treated cells is due to a better dye uptake and a downward shift of the TiO$_2$-conduction band.

The cell layout and cell assembly was different compared to the procedure given in chapter 5. A so-called masterplate layout was used, in which 5 cells of 4 cm² each are placed on one plate,

which allowed the assembly of highly reproducible DSSC. Chapter 6.5.1 give the experimental details for cell assembly.

6.5.1 Cell assembly

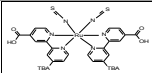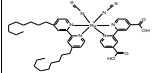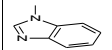The manufacturers and the purity of the chemicals employed in the study are listed below:
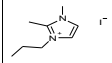
name	manufacturer	purity	formula
N719	Solaronix	-	
Z907	Solaronix	-	
NMBI	Aldrich	99.00 %	
DMPI	INAP	-	
iodine	Merck	99.80 %	I_2
acetonitrile	Merck	99.95 %	CH_3CN
propionitrile (distilled)	Courtesy of EPFL	distilled	C_2H_5CN
propionitrile	Aldrich	99 %	C_2H_5CN
propionitrile	Merck	99.5 %	C_2H_5CN
t-butanol	Merck	99.50 %	C_4H_9OH
titanium(IV)chloride tetrahydrofuran	Aldrich	97 %	$TiCl_4*2THF$

Table 6.8: chemicals used in the study

All the chemicals were used as received without further purification. Transparent conducting glass (F:SnO$_2$-doped) was purchased from Pilkington and had a sheet resistance of 8.5 Ω/□.

The equipment used for the photocurrent/photovoltage transients, impedance and I-V-measurements is listed in table 6.9.

method	equipment	comment
impedance	potentiostat (Autolab)	Steuernagel contant 575 solar simulator used for background illumination (equipped with 575 W metal halide lamp)
photocurrent/photovoltage transients	pulsegeneator (Thurby Thander Instruments) TGP110 10 MHz potentiostat (Autolab)	
stability tests	Solaronix Sulphur-Plasma lamp	
photocurrent vs. voltage	Keithley 2400 Source Meter	illumination with Steuernagel solar simulator

Table 6.9: equipment used in the study

Cells were made by adopting the masterplate concept. A masterplate (Fig. 6.58) has a size of 7,5 * 10 cm and consists of five electrically isolated electrodes each of them being 0,5 * 8 cm. On the front electrode a TiO$_2$ layer of ca. 9.5 µm was screen printed and sintered at 450 °C for 30 min. Then the electrode was immersed into a 50 mM solution of TiCl$_4$*2THF in water for 30 min at 70 °C and rinsed with deionized water and ethanol (technical grade) afterwards. On the counter electrode a platinum-paste was screen printed and fired at 420 °C for 20 min. Prior to use the electrodes were fired again (front electrode 570 °C for 10 min, counter electrode 420 °C for 20 min).

It is noted that the electrodes have to be processed immediately after the heating, as the catalytic activity of platinum decreases if it is exposed to oxygen at room temperature and impurities (carbon dioxide, duste, ...) adsorb on the TiO$_2$-surface.
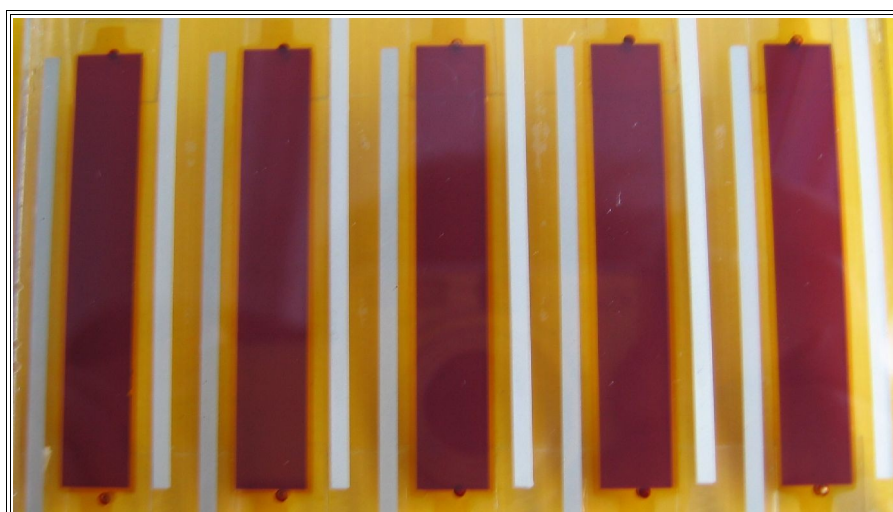

Fig. 6.58: DSSC made with the masterplate concept

Immediately after cooling the front and counter electrode were laminated using Bynel® hotmelt foil. Lamination took place under reduced pressure at 150 °C for 5 min. The distance between front and counter electrode was about 50 μm in average. The coloration of the TiO_2 layer was done in a special coloration machine. The dye solution (1 mM for N719, 0.5 mM for Z907 in acetonitrile/*t*-butanol 1:1) was pumped through two holes in the counter electrode for four hours at 40 °C. After staining, the electrode was flushed with pure acetonitrile to remove all weekly adsorbed dye and dried with nitrogen. The electrolyte (0.6 M DMPI, 0.1 M I_2, 0.5 M NMBI in propionitrile) was then injected with a pipette. The same electrolyte was used throughout the study.

A summary of the experiments in chapter 6.5 is given in table 6.10.

experiment	$TiCl_4$-treatment	electrolyte preparation	parameter		# of cells
water treatment (chapter 6.5.2)	yes	in glove box	reference		7
			addition of 1 % water to the electrolyte		6
			addition of 5 % water to the electrolyte		6
oxygen treatment (chapter 6.5.3)	no	under ambient atmosphere	reference		7
			purging of the electrolyte with oxygen for 3 min		5
			purging of the electrolyte with nitrogen for 3 min		5
$TiCl_4$-treatment (chapter 6.5.4)	yes	under ambient atmosphere	$TiCl_4$ postreatment	remark: another electrolyte was tested, however the results are not included here	6
	no		no $TiCl_4$ postreatment		5
purity of starting material (chapter 6.5.5)	no	under ambient atmosphere	distilled propionitrile		6
			99 % propionitrile		6
			99.5 % propionitrile		5
cell thickness (chapter 6.5.6)	yes	in glove box	4 μm thick TiO_2-electrode		5
			8 μm thick TiO_2-electrode		5
			12 μm thick TiO_2-electrode		5
			16 μm thick TiO_2-electrode		5

Table 6.10: summary of experiments

In each experiment about 20 cells were made. Between two to four parameters were varied in each experiment, thus between 5 - 7 cells were made with the same composition in average. The error bar

given for the solar cell parameters reflect the standard deviation from the given number of cells with the same composition.

Aging tests

The cells were kept in darkness at 80 °C for about 1000 hours. Prior to the characterization (I-V-curves, transient measurements, impedance) the cells were taken out of the oven and kept at room temperature in darkness for 1 - 2 hours. The measurements took about 2 - 3 hours so the heat treatment has been interrupted for 5 hours at the most. This time was subtracted from the total time of the aging experiment.

Photocurrent and photovoltage transient measurements were performed by using a white bias light illumination (three 10 W Solarc lamps WelchAllyn), on which a flash of a red diode array was superimposed. The bias light was adjusted by neutral gray filters to 100, 44, 10 and 3 mW/cm². The diode array comprised two times four diodes, which were arranged in two lines. Within the resulting rectangle the light intensity of the flash was uniform with an error of max. 10 %. The number of photons per flash varied from $0.11\text{-}34*10^{17}$ photons$*$cm$^{-2}*$s^{-1}. The intensity of the flash was adjusted by changing the applied voltage (from 4.8 V to 10 V) or the length of the flash (from 1 to 10 μs). Since the time resolution of the potentiostat is about 20 μs it is assumed that the measured photocurrent/photovoltage curve is only a function of the flash intensity and not of the flash length.

6.5.2 Influence of water on the photovoltaic performance

The role of water in dye sensitized solar cells has not been studied systematically so far and only some data is available on its impact on initial and long term stability [84]. This is astonishing since most solvents contain water to some extend. Furthermore the polymer foils used in present DSSC are permeable for water and the water uptake from the ambient atmosphere might accumulate over time. This is especially true for flexible DSSC with thin PET foils as substrates. Systematic studies on the role of water in liquid DSSC might also help to develop the quasi-solid state NSCSC introduced in chapter 6.4.

In this chapter stability data from cells with a hydrophobic dye (Z907) and a hydrophilic dye (N719), in which water was added to the electrolyte, is discussed (chemical structure on p. 194). In order to assess the maximum concentration of water that might be encountered in a dye sensitized

solar cell under very unfavorable conditions (water penetration through the sealant, high humidity of the ambient atmosphere, impure starting material), an open bottle of propionitrile was allowed to equilibrate with the ambient atmosphere and a water saturated atmosphere. The water concentration in the solvent after 24 hours increased from 0.2 % to 1.1 % and 1.7 % respectively. To be on the safe side the „worst case scenario" was set to be 5 % water in the solvent. In the study, a water concentration of 1 % and 5 % was compared with a reference cell. However, for the clarity of the presentation, only the data for cells with 5 % water in the electrolyte is shown here.
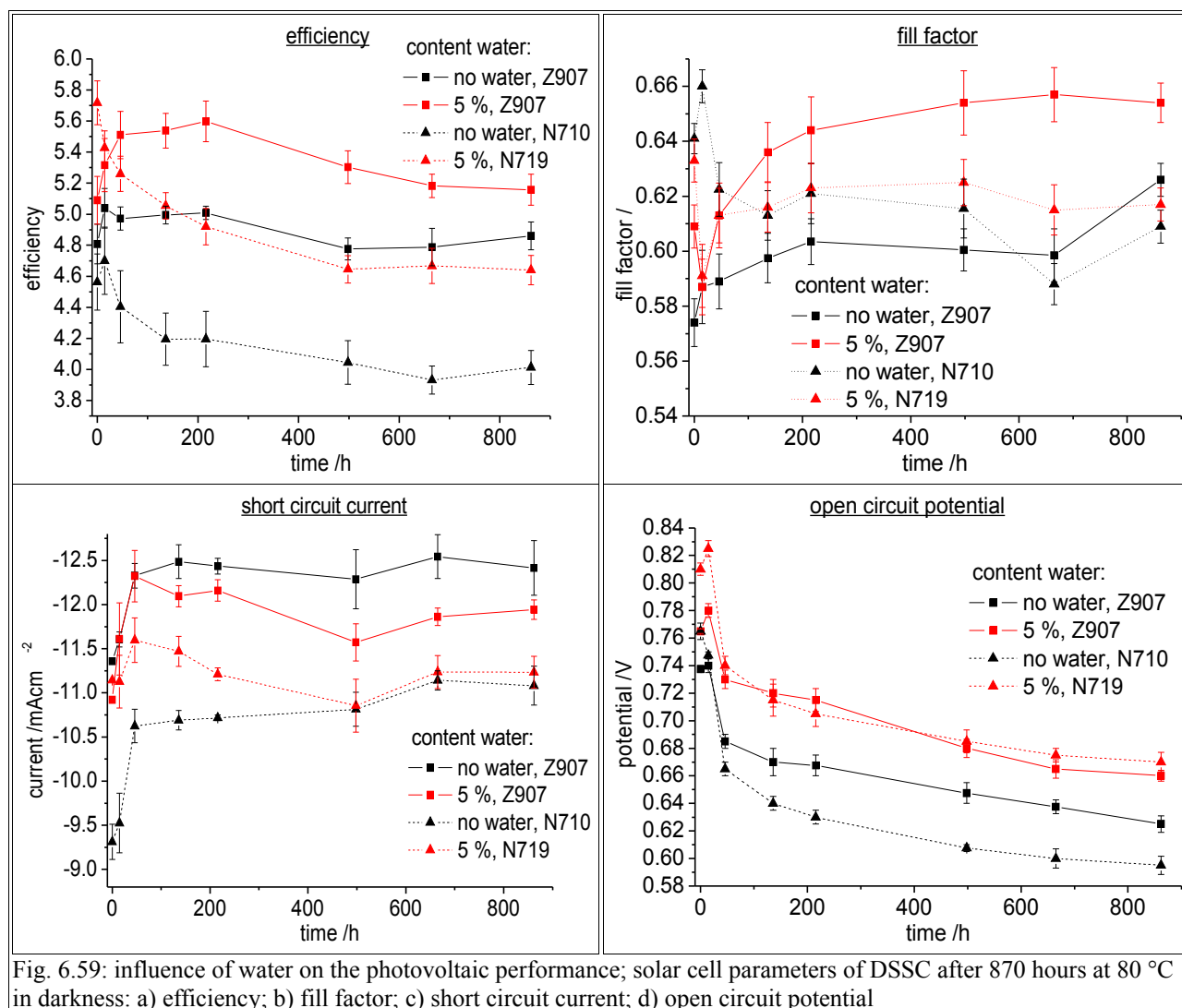

Fig. 6.59: influence of water on the photovoltaic performance; solar cell parameters of DSSC after 870 hours at 80 °C in darkness: a) efficiency; b) fill factor; c) short circuit current; d) open circuit potential

Fig. 6.59 compares the solar cell parameters of water treated cells with the respective reference cells. Interestingly the water treated cells showed not only a better initial performance but also the same stability as the reference cells. For N719 a 15 % and for Z907 a 6 % higher initial efficiency

was observed. The higher performance was still observed after 860 hours at 80 °C indicating that the derivative of the efficiency with respect to time was the same for the reference cells and the water treated cells. For Z907 ca. 97 % and for N719 ca. 85 % of the initial efficiency was retained after the aging test. Although some degradation was observed for the N719 stained cells, this cannot be attributed to the water in the electrolyte since the degradation rate is the same as for the reference.

The higher performance of the water treated cells is mainly due to a higher V_{OC} (Fig. 6.59d) Throughout the test the water treated cells exhibited a higher voltage than the corresponding reference. The effect was most pronounced for N719 stained cells (between 40 - 70 mV) and somewhat less pronounced for Z907 (ca. 30 mV).

For Z907 the higher cell voltage is partly compensated by a lower short circuit current (Fig. 6.59c). Though the initial I_{SC} was about the same it decreased by ca. 4 % after the aging experiment started. For N719 the initial short circuit current was about 14 % higher for the water treated cell and about the same for the time period 500 h < t < 860 h.

This stability data proves that the hydrophilicity of the dye does not determine the stability of a DSSC in the presence of water alone and the proposed saponification of dye molecules [84] can be prevented using the right boundary conditions. For the first time it was demonstrated that water can enhance the efficiency of DSSCs and should be regarded as a coadsorbent rather than an unwanted impurity.

It has been argued [194] that one of the advantages of Z907 is its hydrophobic side chain and its ability to repel water from TiO_2 surface. Though it was shown that water does not detach dye molecules from the surface it might still induce a chemical degradation of the dye. By visible inspection, the stained TiO_2-layer of the water treated cells seemed to be somewhat lighter compared to the reference cell after ca. 200 h at 80 °C. This could be verified by UV/Vis spectroscopy. As can be in figure 6.60, the absorption onset shifted to shorter wavelength when the electrolyte contained water. This is most likely due to a ligand exchange in the Ru-complex. The chromophore SCN is replaced by OH. The lower absorption in the range from 530-700 nm is about the same for N719 and Z907, but only for Z907 a lower short circuit current is observed.

Fig. 6.60: UV/Vis-spectrum of DSSC taken after 500 h at 80 °C.
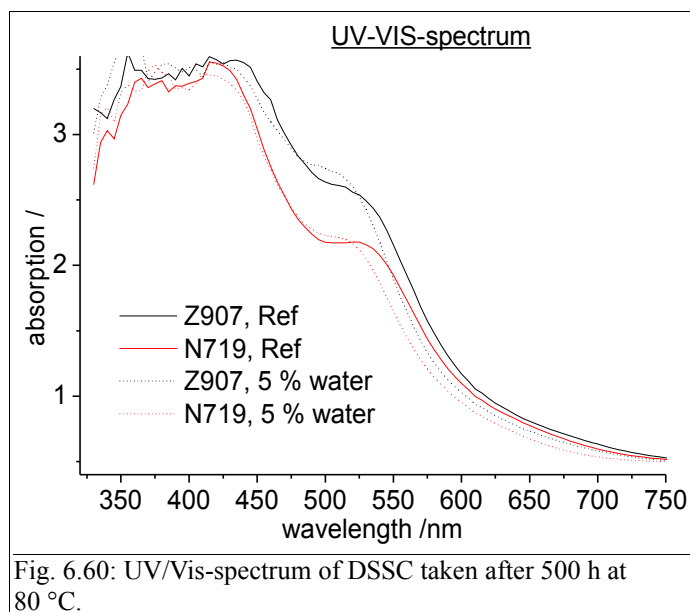
Having demonstrated the beneficial effect of water on the open circuit potential, the question arises, to which extend the suppression of the recombination rate and a shift of the TiO_2-Fermi level contributes. Like any other additive, water can be considered as a coadsorbent that might alter the cell potential in two ways: either by inducing or withdrawing electrons into the TiO_2 or by changing the rate constant for the recombination reaction with I_3^-. In presence of 0.5 M NMBI, the electrolyte is alkaline and the nitrogen atom of the imidazole ring induces electron density into the TiO_2, creating a Helmholtz-layer at the TiO_2/electrolyte interface. Thus an upward shift of the conduction band is expected.

The introduction of a blocking layer between TiO_2 and the electrolyte has been successfully demonstrated both with inorganic [216][217] and organic [218][219] blocking layers. In this study, two different dyes has been tested, one of them being hydrophobic (Z907) the other being hydrophilic (N719). The question is to what extend can the hydrophobic dye Z907 repel water from the surface and are there significant differences to the hydrophilic dye N719. Looking at the recombination rate constant vs. time (Fig. 6.61a) and vs. photopotential (Fig. 6.61b) it turned out that water reduced the recombination rate for both dyes, but for N719, this effect is much more pronounced. The recombination rate was decreased 2.6 times (N719) and 2.0 times (Z907) 24 hours after the cell were exposed to 80 °C and 2.3 times (N719) and 1.1 times (Z907) after 1000 hours at 80 °C. That means that the N719 sensitized TiO_2 surface can suppress electron recombination more effectively and this suppression is almost not effected by the heat treatment whereas for Z907 this effect diminishes over time. Studying Z907 sensitized cells without $TiCl_4$ treatment (not shown

here) the same trend is observed. However, the absolute values (1.3 times slower recombination after 24 h and 1.05 times after 1000 h) are much smaller indicating that the impact of water treatment also depends on the substrate.
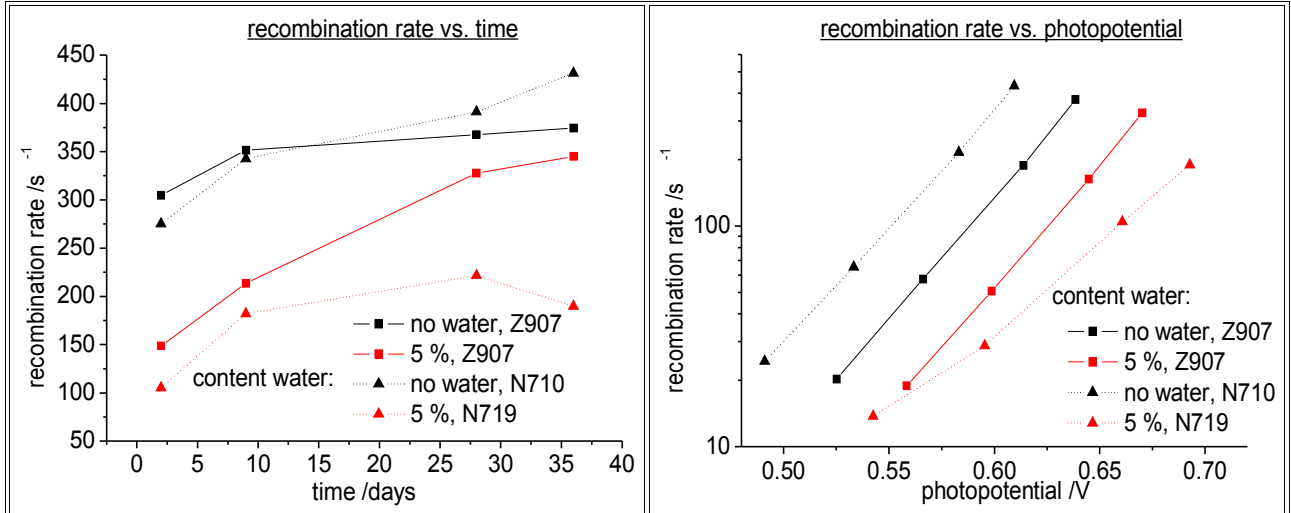

Fig. 6.61: a) recombination rate as a function of time extracted from photovoltage transient measurements; bias light: white halogen lamp 100 mWcm^{-2}; pulse red LED (λ_{max} = 625 nm)
b) recombination rate after 36 days at 80 °C in darkness as a function of photopotential; pulse red LED (λ_{max} = 625 nm)

The impact of the recombination rate on the V_{OC} was estimated by using equation 6.77, which describes the open circuit potential for regenerative electrochemical cells [220]. It is assumed that the incident photon flux is proportional to the short circuit current I_{SC}, which seems to be justified in the range from 3 mWcm^{-2} to 100 mWcm^{-2}.

$$V_{OC} = A * \frac{kT}{e} * \ln \frac{I_{Inj}}{c_{0,el} * k_1 * [I_3^-]} \propto A * \frac{kT}{e} * \ln \frac{I_{SC}}{k_{rec}} \quad (6.77)$$

V_{OC} = open circuit potential /V; A = ideality factor /; kT/e = thermal voltage = 25.7mV; I_{inj} = injection rate /Qcm^{-3}s^{-1}; c_{e^-} = concentration of electrons in darkness /Qcm^{-3}; k_1 = rate constant for triiodide reduction /M^{-1}s^{-1}; [I$_3^-$] = triiodide concentration /M; I_{SC} = short circuit current /Qcm^{-3}; k_{rec} = recombination rate /Qcm^{-3}

By plotting $V_{OC,rec}$ vs. ln(1/k), A was found to be 7.0 ± 1 after 24 hours. Then it decreased continuously to 5.2 ± 0.8 after 1000 hours. By comparing the recombination rate constant of the reference cell with the water treated cell the shift of $V_{OC,rec}$ at a given electron concentration could be determined. After 24 hours $\Delta V_{OC,rec}$ is 150 mV for N719 and 110 mV for Z907 whereas after 1000 hours $\Delta V_{OC,rec}$ is 120 mV (N719) and 15 mV (Z907). Without TiCl$_4$ treatment $\Delta V_{OC,rec}$ was

40 mV (Z907, 24 h) and 10 mV (Z907, 1000 h) respectively, showing the same trend as the $TiCl_4$ treated cell.

To summarize, the extend to which water treatment suppresses recombination depends both on the substrate and the dye.

Beside the different recombination rates the shift of the conduction band $\Delta V_{OC,bandshift}$ might also alter the open circuit potential. To determine $\Delta V_{OC,bandshift}$ an exponential increase of surface trap state towards the conduction band was assumed as done by other authors [221][222].

$$DOS = \frac{1}{e} \frac{\Delta Q}{\Delta V} = DOS_0 * e^{\frac{V_{OC}}{m_C}} \Leftrightarrow V_{OC} = m_C * \ln\left(\frac{DOS}{DOS_0}\right) \quad (6.78)$$

DOS = density of trap states /cm^{-3}; ΔQ = injected charge /C; ΔV = change of photovoltage /V;
e = elementary charge = 1.6022*10^{-19} C;

Plots of ln(DOS) against V_{OC} are shown in figure 6.62. The parameter m_c can be determined from the slope and the band shift $\Delta V_{OC,bandshift}$ corresponds to the horizontal shift between the lines. From equation 6.78 the shift can be calculated to be

$$\Delta V_{OC} = m_C * \ln\left(\frac{DOS_{0,cell1}}{DOS_{0,cell2}}\right) \quad (6.79)$$

From figure 6.62 it can be seen that the water treatment induces a downward shift of the TiO_2 conduction. The extend of the band shift depends on the dye, the TiO_2 pretreatment and the age of the cell. In general one can expect water to behave like an acid in the alkaline electrolyte. Protons are transfered to the TiO_2 surface and thus charging it positive. One can see from figure 6.62a and 6.62b that this shift is more pronounced for N719 than for Z907 after 24 h at 80 °C. Together with the information about the recombination rate, which showed a similar trend, a likely reason for this observation is, that more water can absorb on a N719 sensitized surface. This would be in agreement with the idea that Z907 repels water from the surface due to its hydrophobic side chain [223]. For N719 the band shift is -50 mV and for Z907 -30 mV ($TiCl_4$ treatment) and -15 mV (no $TiCl_4$ treatment, not shown here) (s. table 6.11).
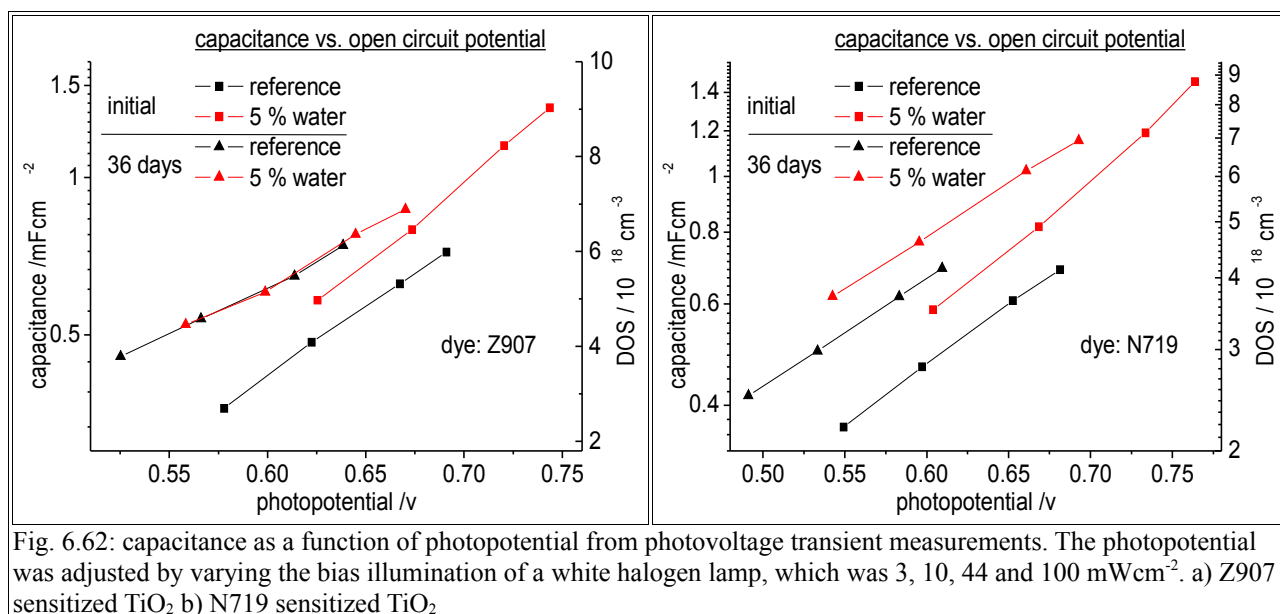
Fig. 6.62: capacitance as a function of photopotential from photovoltage transient measurements. The photopotential was adjusted by varying the bias illumination of a white halogen lamp, which was 3, 10, 44 and 100 mWcm^{-2}. a) Z907 sensitized TiO_2 b) N719 sensitized TiO_2

In the course of the aging experiment a band shift to lower energy is observed for both the reference cell and the water treated cells. So the decrease of the V_{OC} that is typically observed in aging experiments [224] is not only due to an enhanced recombination but also due to a positive bandshift. However, for water treated cells the shift is less pronounced reducing the difference to the reference cell.

Recapitulating it could be demonstrated that water adsorbs on the surface of the TiO_2 and slows down the recombination reaction with triiodide. At the same time the conduction band is shifted electrochemically positively in water treated cells. It was tried to quantify the shift of V_{OC} for each effect to estimate the overall change in open circuit potential. Table 6.11 compares the calculated and observed changes of V_{OC}. It can be seen that the calculated open circuit potential fits the experimental observation quite accurate. A deviation of up to 20 mV might be due to the relatively large error of the prexponetiell factors A and m_c in equation 6.77 and 6.78.

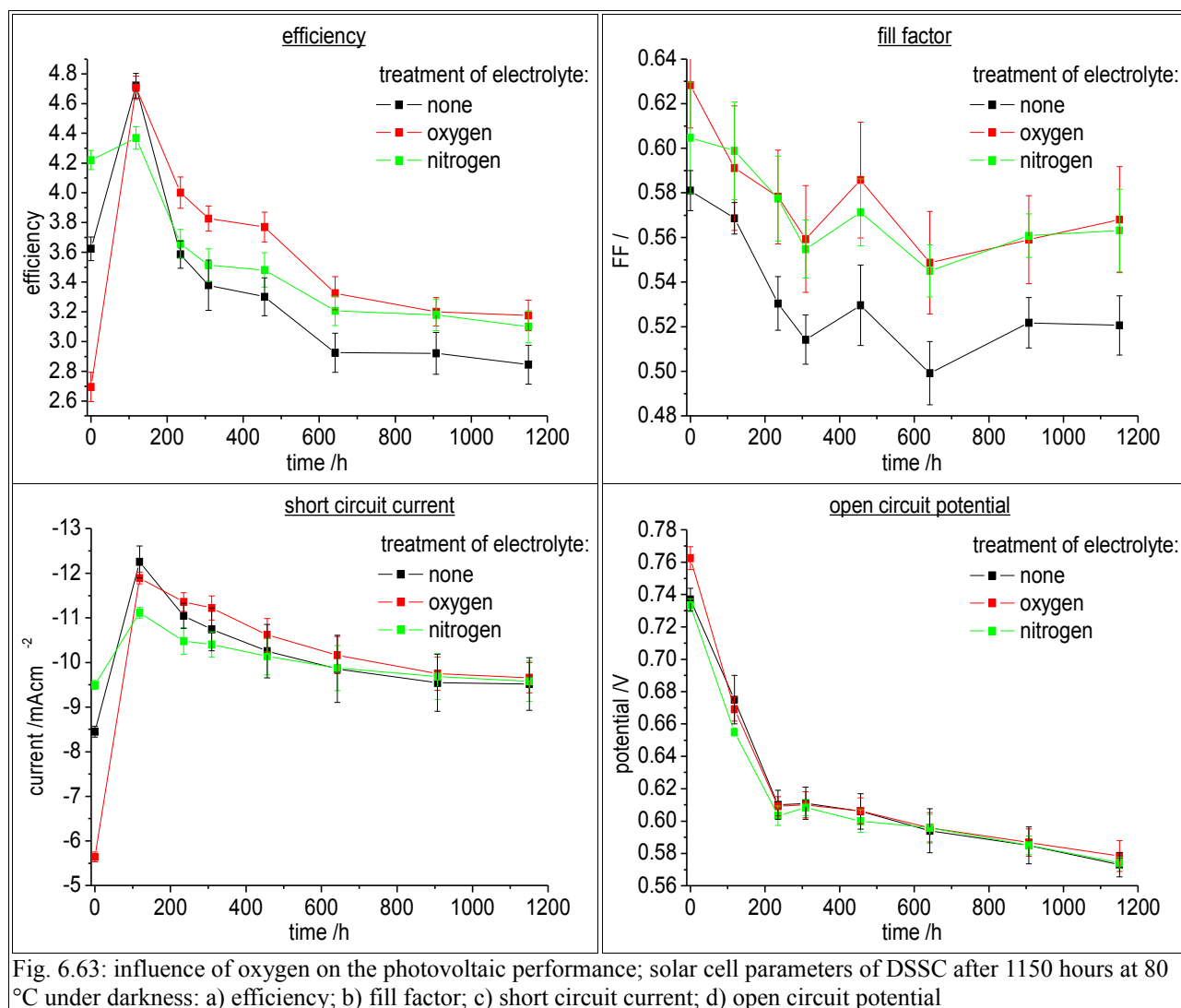|	ΔV_{rec} /mV	$\Delta V_{bandshift}$ /mV	$\Delta v_{calculated}$ /mV	$\Delta v_{observed}$ /mV
N719, TiCl$_4$, 24 h	150	-50	100	82
N719, TiCl$_4$, 1000 h	120	-40	80	83
Z907, TiCl$_4$, 24 h	110	-30	80	53
Z907, TiCl$_4$, 1000 h	15	5	20	31
Z907, **no** TiCl$_4$, 24 h	40	-15	25	34
Z907, **no** TiCl$_4$, 1000 h	10	-5	5	26

Table 6.11: calculated and observed change of V_{OC}

6.5.3 Influence of oxygen on the photovoltaic performance

Most polymers have a permeability for oxygen in the range of 10^{-13} $cm^2s^{-1}Pa^{-1}$. Thus a considerable uptake of oxygen has to be considered for sealed, liquid DSSCs and the impact on the cell stability needs to be scrutinized. This information is also very important for the development of NSCSCs, which are exposed to a high concentration of oxygen. However, no systematic study about the impact of oxygen on cell stability can be found in the literature.

In this chapter, an oxygen saturated electrolyte was compared with a nitrogen saturated and reference electrolyte. The electrolyte was split into three batches prior to the filling of the cells. Batch 1 was flushed with oxygen for three minutes, batch 2 with nitrogen for three minutes and batch 3 was used as a reference. Figure 6.63a-d show the solar cell parameters for the three different electrolytes during an aging experiment for 1150 hours at 80 °C. It can be seen that the oxygen treatment had a significant effect on the short circuit current initially but already after equilibration for 100 hours at room temperature all the cells in the test had very similar solar cell parameters. Repetition of this experiment with a higher time resolution revealed that an increase of the short circuit current like

$$A*(1-e^{\frac{-t}{B}}) \quad (6.80)$$

is observed in the beginning (Fig. 6.65a).

Fig. 6.63: influence of oxygen on the photovoltaic performance; solar cell parameters of DSSC after 1150 hours at 80 °C under darkness: a) efficiency; b) fill factor; c) short circuit current; d) open circuit potential

In Fig. 6.63a it is noted that the efficiency of the reference electrolyte seemed to be somewhat lower than the O_2/N_2-saturated electrolyte. This is most likely due to the fact, that the concentration of the O_2 and N_2 flushed electrolytes is a bit higher, since some of the solvent evaporated when the electrolyte was flushed with O_2/N_2. Therefore the conductivity of the electrolyte is higher and one obtains a higher fill factor due to a lower series resistance.

All other solar cell parameters stay remarkably constant during the aging experiment. The photovoltage/photocurrent transient measurements, which are not shown here, also suggest that the gas treatment seems to have little effect on the position of the TiO_2-conduction band, the recombination rate and the effective diffusion coefficient of the electrolyte.

It can be concluded from these experimental findings that there is an oxygen sink in the cell that prevents the oxidation of the dye or other organic compounds of the cell. The most straight forward

assumption is that the iodide reduces oxygen at platinum coated counter electrode. The overall reaction would be:

$$4I^- + 2O_2 + 4H^+ \rightarrow 2I_2 + 4OH^- \qquad (6.81)$$
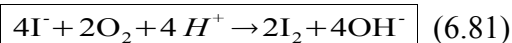
The protons involved in this reaction are taken from the water, which is always present in the electrolyte (up to 1 % were found in the organic solvent). To test this assumption a DMPII solution was purged with O_2 in a three electrode system and a negative potential of -0.2 V was applied to a platinum working electrode. The solution turned brownish within minutes indicating that iodide was oxidized to iodine. The reaction products, iodine and hydroxy ions, do not have a significant impact on the cell performance. The iodine/iodide ratio is affected a little bit and one would expect a little bit lower open circuit potential since the redox potential of the electrolyte is shifted electrochemically more positive. But since the maximum oxygen concentration can be estimated to be ca. $2.5*10^{-4}$ mol/l and is ca. 400 times lower than the iodine concentration (0.1 mol/l) the effect is too small to be measured. The generation of hydroxy ions will lower the pH of the electrolyte and shift the Fermi-level to higher energies, which should be reflected in a higher open circuit potential. And indeed a 30 mV higher open circuit potential was measured initially for the oxygen purged electrolyte (Fig. 6.63d).

Still it was very puzzling to see that the initial short circuit current was much lower for the O_2-saturated electrolyte compared to the reference. Since transient measurements could not reveal significant differences, impedance spectroscopy was used to characterize the cell. This technique has been proven to be a useful tool in the analysis of charge transport in DSSC [225][226][227], since it includes both the charge transport kinetics at the front/counter electrode and within the electrolyte.

Though the detailed analysis of the spectra requires a rather complicated equivalent circuit, the basic features are determined by mainly two interfaces: the charge transfer resistance at the Pt/electrolyte interface, which is characterized by an arc at low resistance in the Nyquist plot, and at the TiO_2/electrolyte interface with an arc at higher resistance. The corresponding equivalent circuit is shown in Fig. 6.64. A detailed introduction into impedance spectroscopy in DSSC in given in [226], the role of the electrolyte is discussed in [228].

Fig. 6.64: equivalent circuit used for impedance fitting
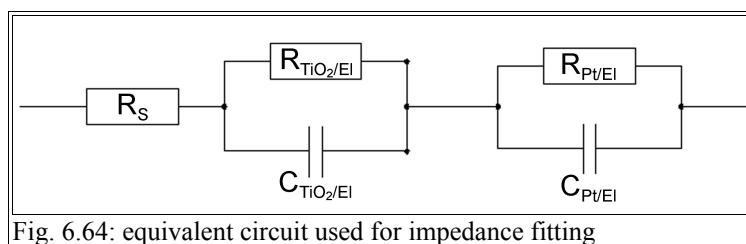
The Nyquist plot of DSSCs with O_2/N_2-flushed electrolytes is shown in Fig. 6.65b. Three arcs are visible, which partly overlap:

1) $Z' \approx 1.5\ \Omega$: charge transfer resistance at the interface between the platinized counter electrode and electrolyte $R_{Pt/El}$.

2) $1.5\ \Omega < Z' < 3\ \Omega$: charge transfer resistance at the interface between the TiO_2 and the electrolyte $R_{TiO2/El}$.

3) $Z' \approx 3.5\ \Omega$ (initial) and $Z' \approx 2.8\ \Omega$ (day 5): impedance of the electrolyte (not included into the analysis)
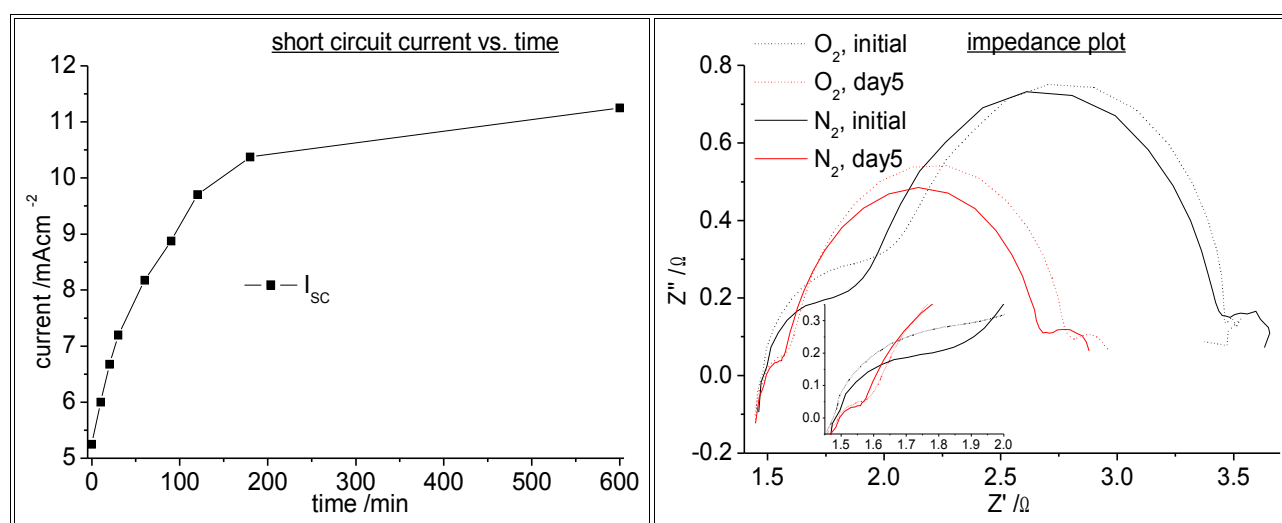

Fig. 6.65: a) short circuit current as a function of time for DSSC with oxygen-saturated electrolyte; illumination: Steuernagel solar simulator (100 mWcm^{-2})
b) impedance spectra of DSSC with O_2/N_2-saturated electrolyte. Frequency 1 Hz < ν < 100 kHz. Cells were measured under open circuit operation with a bias illumination of 100 mWcm^{-2} (Steuernagel solar simulator) with an Autolab potentiostat.

The spectra in Fig. 6.65b were modeled using the program ZPlot. The parameters extracted are given in table 6.12.

	O$_2$, initial	O$_2$, day 3	O$_2$, day 5	N$_2$, initial	N$_2$, day 3	N$_2$, day 5
R$_S$ / Ω	1.47	1.48	1.495	1.47	1.48	1.49
R$_{TiO2/El}$ / Ω	1.44	1.67	1.13	1.52	1.82	1.22
C$_{TiO2/El}$ / mF	1.1	1.78	2.28	1.42	2.4	1.8
R$_{Pt/El}$ / Ω	0.63	0.285	0.095	0.39	0.305	0.101
C$_{Pt/El}$ /mF	0.46	0.62	0.8	0.5	0.4	0.65

Table 6.12: parameters used to fit the impedance spectra in Fig. 6.65b

It can be seen that the charge transfer resistance at the Pt/electrolyte interface is significantly higher initially (0.63 Ω vs. 0.39 Ω) and that all other parameters are basically the same. After exposure to 80 °C the resistance decreases both for the oxygen and nitrogen treated cell whereas the effect is much more pronounced for the O$_2$-treated cell. After 5 days the resistance at this interface is about the same. Obviously the catalytic activity of the Pt is affected by the oxygen treatment, which was not expected since the binding energy of Pt to oxygen is typically low.

When examining the solvent propionitrile with GC-MS, it turned out that it contains a lot of impurities (total 1779 µg/l), ethyldi-n-butylamine (715 µg/l), 1-butanol (415 µg/l) 2-methylpropanenitrile (143 µg/l) being the most abundant one. When repeating the experiment with a distilled solvent (total impurity content 517 µg/l) the initial short circuit current was almost the same for the oxygen-flushed and the nitrogen flushed electrolyte. Thus it can be concluded that the poisoning of the Pt-electrode was most likely due to the products of a reaction between the oxygen and some of the contaminants.
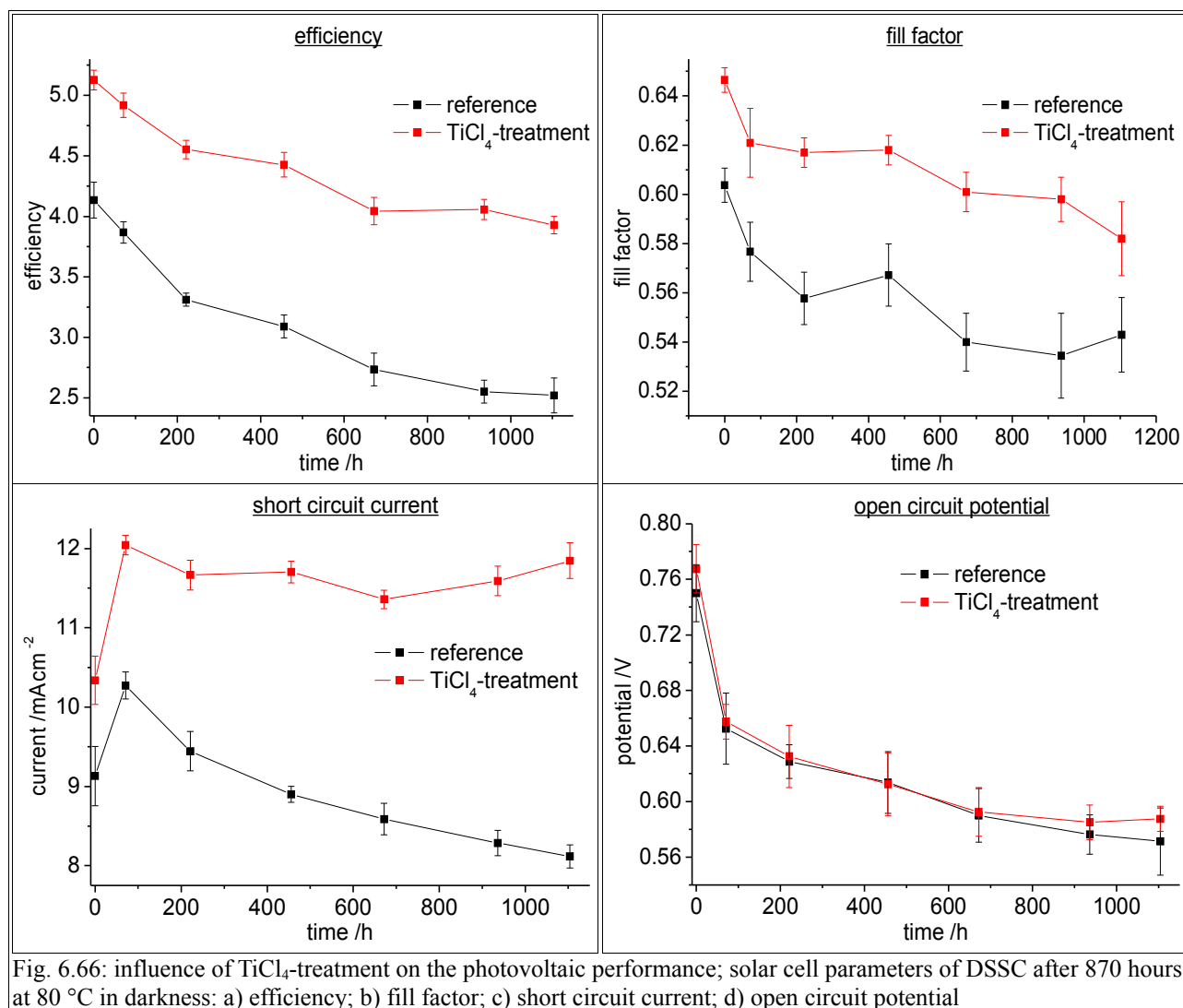
6.5.4 TiCl$_4$-treatment of the TiO$_2$-electrode

The deposition of a thin TiO$_2$-layer on top of TiO$_2$-nanoparticles either by electrodeposition [137] or by dip coating in an aqueous solution of TiCl$_4$ [229][230][231] or titaniumisopropoxide [232] and successive annealing is found to significantly improve the conversion efficiency of DSSCs. Though these empirical observations have been made already in 1993 [137], there is still no generally accepted explanation. Most often the authors report an increased short circuit current while the open circuit potential and the fill factor remain basically unaffected. TEM, BET and XRD measurements

revealed that the TiCl₄-treatment does not affect the layer thickness, but results in a 26 % smaller BET-surface area, a 6 % smaller electrode surface area and let the average particle size increase by 20 % [229]. Up to now the following explanations for the enhanced I_{SC} have been given.

1) The light scattering within the TiO_2 layer is enhanced [230]. This is especially important for longer wavelength where the absorbance of the layer is low.

2) The binding of the dye to the TiO_2 is improved [231]. Infrared spectroscopy suggest a stronger binding energy.

3) The recombination rate between conduction band electrons and iodine is suppressed, which overcompensates a shift of the TiO_2-conduction band to lower energy [229].

In this chapter the impact of TiCl₄ post treatment on the initial conversion efficiency and the long term stability is investigated by I-V-measurement, UV-VIS-spectroscopy and photovoltage/photocurrent transient measurements. The deposition of the additional TiO_2-layer was done by dip-coating. The electrodes were immersed into a 50 mM solution of TiCl₄*2THF in water for 30 min at 70 °C and rinsed with water and ethanol afterwards. Prior to the cell assembly the electrodes were fired for 10 min at 570 °C.

After preparation the cells were exposed to 80 °C for 1100 h. I-V-curves were taken at different points and the solar cell parameters are shown in Fig. 6.66. It can be seen that the initial efficiency was improved by ca. 24 % and the degradation after exposure to 80 °C could be significantly slowed done. After 1100 h the TiCl₄-treated cells gave a 58 % higher efficiency. The higher efficiency was mainly due to a better short circuit current and a slightly better fill factor, whereas the open circuit potential remained almost unaffected. The short circuit current was enhanced by ca. 13 % initially and 46 % after 1100 hours at 80 °C.
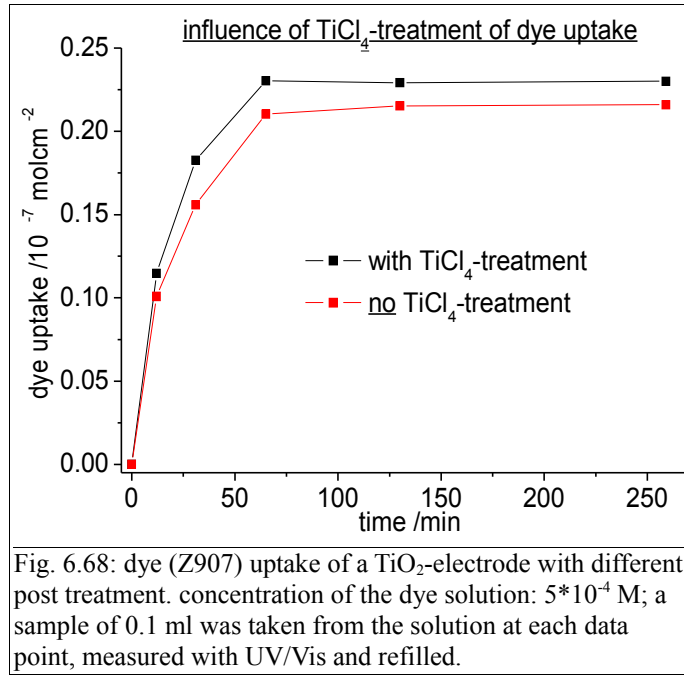
Fig. 6.66: influence of TiCl$_4$-treatment on the photovoltaic performance; solar cell parameters of DSSC after 870 hours at 80 °C in darkness: a) efficiency; b) fill factor; c) short circuit current; d) open circuit potential

The characterization of the TiO$_2$-electrodes was done with BET,TEM and XRD for electrodes that were prepared employing the same procedure [229]. As mentioned above the TiCl$_4$-treatment basically increases the average particle size whereas the effective electrode area remains about the same. The thickness of the layer for and after the TiCl$_4$-treatment is given in Fig. 6.67. It can be seen that the effect on the layer thickness is negligible indicating that the growth of the additional TiO$_2$-layer takes place only within the layer.

Fig. 6.67: impact of the TiCl$_4$-treatment on the layer thickness
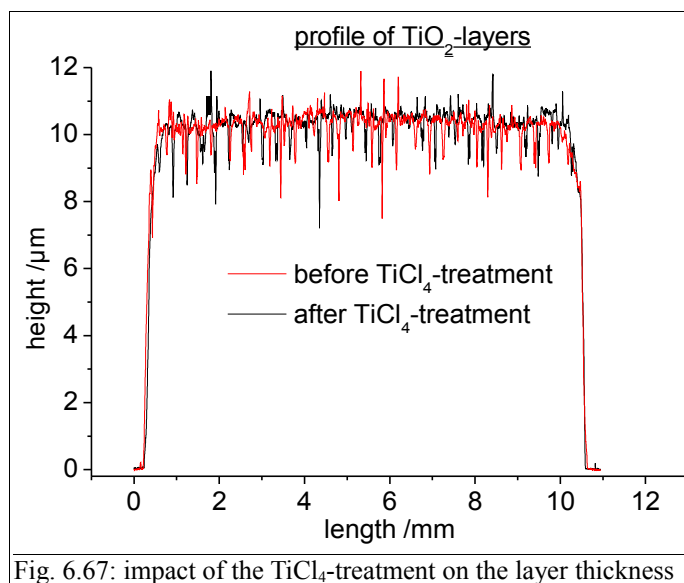
The active electrode area is mostly defined by its dye uptake. It emphasizes the importance of inaccessible parts of the TiO$_2$-surface area due to pore plugging or anchoring ability of different lattice planes in the crystal. The dye uptake can be determined by desorbing the dye from a TiO$_2$-electrode with aqueous NH$_3$-solution[229] and measuring the absorption of the solution. However, this method works only under the assumption that the desorption occurs quantitatively on both TiCl$_4$-treated electrode and the respective reference.

For this reason the dye uptake was measured directly by measuring the absorption of the dye solution in the staining process at different times. With the help of a calibration curve the lower absorption of the dye solution could be correlated with the dye uptake. In Fig. 6.68a it can be seen that about 6 % more dye is adsorbed on a TiCl$_4$-treated electrode compared to the reference electrode (for the same layer thickness).

Fig. 6.68: dye (Z907) uptake of a TiO_2-electrode with different post treatment. concentration of the dye solution: $5*10^{-4}$ M; a sample of 0.1 ml was taken from the solution at each data point, measured with UV/Vis and refilled.

However, when looking at the initial short circuit current in Fig. 6.66a, it turns out that a 11.9 % increase of the short circuit current was found indicating that the enhanced dye absorption can only partly explain the higher short circuit current. Besides the absorption efficiency of the layer η_{abs}, which is determined by the film morphology (light scattering) and dye loading, the injection efficiency η_{inj} and the extraction efficiency η_{ext} of the film contribute to the incident photon to current conversion efficiency IPCE.

$$IPCE = \eta_{abs} * \eta_{inj} * \eta_{ext}$$ (6.82)

The extraction efficiency might be influenced by the transport properties of the TiO_2-layer. However, since the electron extraction at I_{SC} is found to be about one order of magnitude faster than the electron lifetime (Fig. 6.69), only a negligible fraction of the injected electrons recombine in that time frame.

Still the photovoltage decay is significantly different in $TiCl_4$ treated and non-treated cells as can be seen in Fig. 6.69a. The photovoltage rise time is a good measure for the charge transport resistance at the TiO_2/FTO-interface. At low photopotential (in Fig. 6.69a the photopotential was 0.5 V) the rise time is significantly longer than the time resolution of the potentiostat, which was 20 μs. It can be seen that the rise time is about 16.5 times longer for the untreated electrode, which can be

rationalized in the following way: the charge transfer resistance is a function of the contact area between the TiO_2 and the FTO. For the untreated, spherical TiO_2-nanoparticles the contact area is significantly smaller compared to the situation where a thin TiO_2-film is deposited on the FTO-substrate.

Thus it can be expected that the series resistance in the untreated cell is higher, which might have an effect on the charge extraction efficiency. However, as can be seen in Fig. 6.69b, the current transient is only slightly retarded by ca. 1 ms. This time frame is much to short to have an impact on the charge extraction efficiency.
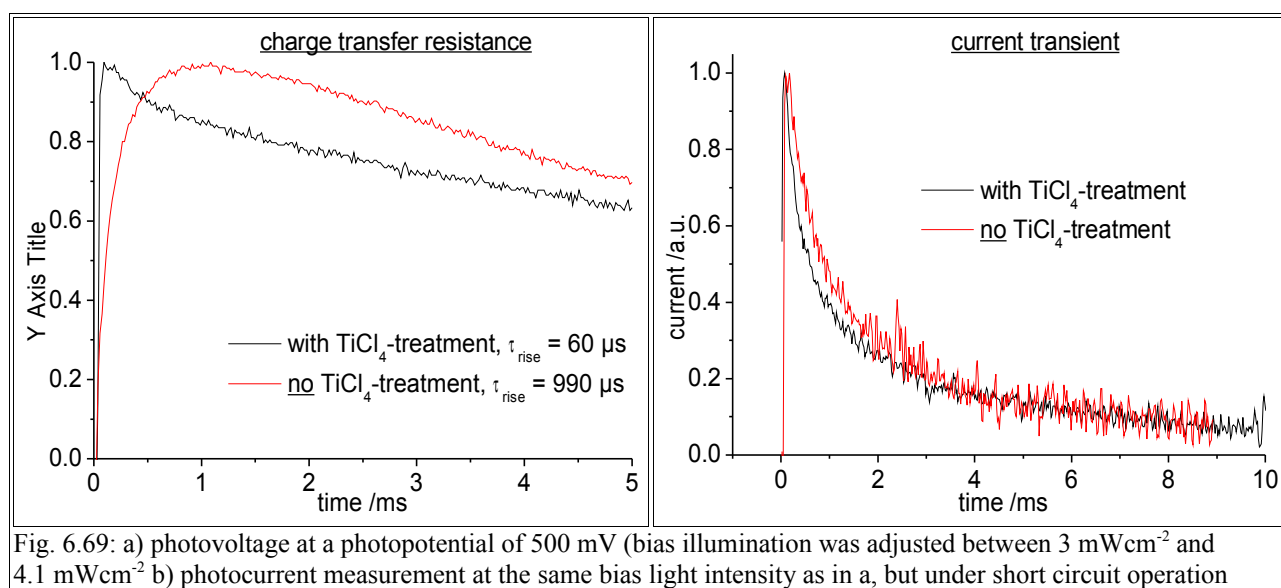

Fig. 6.69: a) photovoltage at a photopotential of 500 mV (bias illumination was adjusted between 3 mWcm^{-2} and 4.1 mWcm^{-2} b) photocurrent measurement at the same bias light intensity as in a, but under short circuit operation

The third factor in equation 6.82 is the charge injection efficiency η_{inj}. It will be mostly determined by the position of the TiO_2-conduction band. If its energy is shifted electrochemically more positive the driving force for charge injection is increased and thus charge injection efficiency is increased. The position of the TiO_2-conduction band can be determined by measuring the capacitance according to the procedure explained in chapter 6.3.5. One underlying assumption is that no additional trap states are generated by the $TiCl_4$-treatment. As can be seen in Fig. 6.70 about 2.03 times more trap states are available initially at the same photopotential. Although it cannot be ruled out that additional trap states might form, it is very unlikely that trap state concentration increases by 203 % and it is believed that the increased number of trap states is mainly due to a shift of the conduction band. Looking at the horizontal displacement it turns out that the $TiCl_4$-treatment induces a shift of 25 mV initially and 28 mV after 1000 hours in darkness. This additional driving

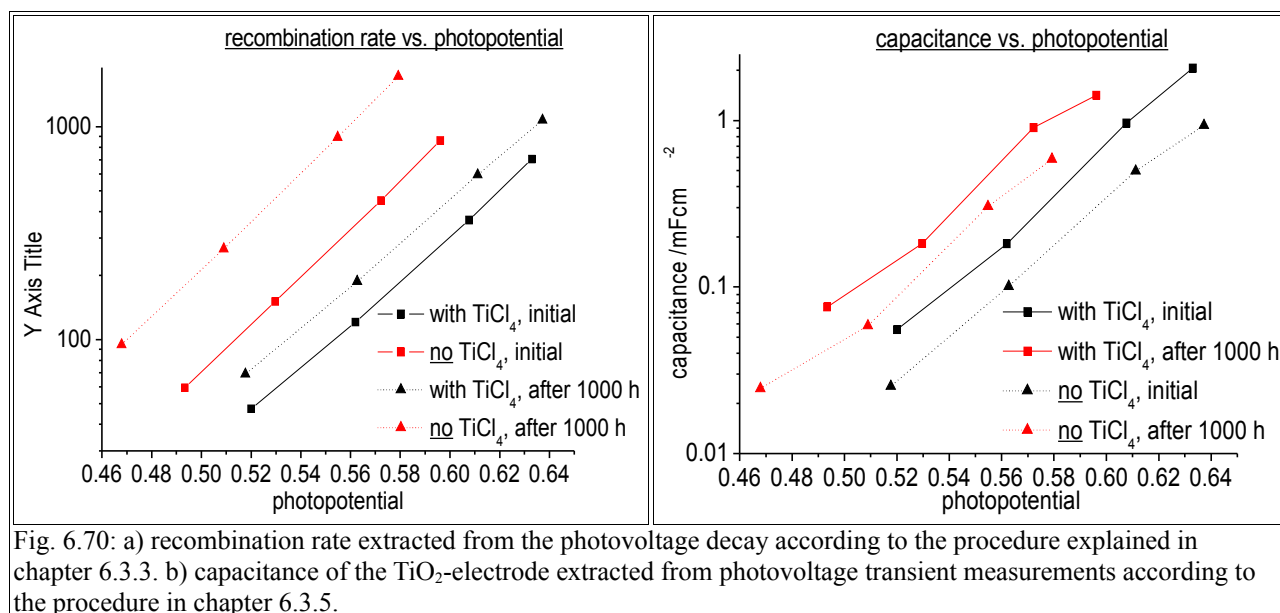force is believed to account for the better charge extraction efficiency.

Fig. 6.70: a) recombination rate extracted from the photovoltage decay according to the procedure explained in chapter 6.3.3. b) capacitance of the TiO$_2$-electrode extracted from photovoltage transient measurements according to the procedure in chapter 6.3.5.

It could be noted that the downward shift of the conduction band should give a lower V_{OC}. This does not occur initially and only after 1100 h at 80 °C a slight shift to lower open circuit potential is observed. This can be explained in terms of a lower recombination rate. Fig. 6.70a plots the recombination rate as a function of photopotential. It can be seen that the recombination rate is reduced by ca. 51 % initially and about 83 % after 1100 hours at 80 °C. Thus the TiCl$_4$-treatment suppresses effectively electron recombination, which compensates the downward shift of the TiO$_2$-conduction band. As a net result the open circuit potential remains about the same.

To summarize it could be demonstrated that the enhanced short circuit current of TiCl$_4$-treated cells is partly due to an improved dye uptake and partly due to a downward shift of the TiO$_2$-conduction band.

6.5.5 Purity of the starting material

In this chapter the impact of the solvent purity on the stability of DSSC is discussed. This is part of the more fundamental question: what is the demand on the purity of the starting materials (dye,

electrolyte, TiO_2) and the process itself to end up with an efficient and stable device.

Up to now, little evidence is found in the experimental section of publications that special care is taken to purify the chemicals. Most often the chemicals are used as received.

That might underestimate the impact of impurities especially in the electrolyte. The deposition of a few nmol of coadsorbents in the NSCSC (chapter 6.4.5) has demonstrated a drastic change of the TiO_2/electrolyte interface properties. If impurities with a high affinity to the TiO_2 are present in the electrolyte they might accumulate on the TiO_2-surface and alter the recombination rate or the flat band potential of the TiO_2.

Three different solvent batches were tested in DSSCs to scrutinize the impact on cell efficiency and cell stability (1000 h at 80 °C in darkness). First the most important impurities were identified and quantified. As can be seen in table 6.13, the purity of the solvent propionitrile varied significantly in the different batches. The batch of Aldrich with a guaranteed purity of 99 % contained about 0.18 % organic material, the batch of Merck with 99.5 % guaranteed purity about 0.27 %. Distillation could reduce the amount of impurities to 0.05 %.

	propionitrile (99 %) /µg*g^{-1}	propionitrile (99.5 %) /µg*g^{-1}	propionitrile distilled /µg*g^{-1}
?	74	224	32
acetaldehyde	55	116	26
propanal	83	580	58
2-propenenitrile	20	342	< 5
2-methylpropanenitrile	143	42	82
2-butennitrile	104	32	34
1-butanole	415	198	112
2-pentanone	< 5	5	< 5
3-pentanone	< 5	11	< 5
2-hydroxypropenenitrile	61	138	23
?	75	610	53
?	5	54	< 5
butanedinitril	20	64	14
ethyldi-n-butylamine	715	279	78
total	**1779**	**2694**	**517**

Table 6.13: HPLC-analysis of different propionitrile batches

If one converts the concentration in µg/g to the amount per square centimeter active cell area (in mol/cm²), the volume of the electrolyte per cm² active cell area and the molar mass of each component needs to be know. For example for propanal with a molar mass of 58 g/mol and an electrolyte volume of 3 µl/cm² the concentration of 83 µg/g corresponds to ca. $4.3*10^{-12}$ mol/cm² active cell area. That means impurities are present in the picomol-range and even if they accumulate on the TiO_2-surface less than 0.1 % of the TiO_2-surface is covered with a monolayer.

Beside organic impurities a significant amount of water was found by Karl-Fischer titration. According to table 6.14, the water content varied between 0.09 % (propionitrile 99 %) and 0.22 % (propionitrile distilled). As a rule of thumb, the exposition time to the ambient atmosphere determines the water content. The bottle with the distilled propionitrile has been in use for more than one year whereas the other bottles were opened immediately before the electrolyte preparation. Yet, the maximum difference of 0.13 % is believed to have no impact on the cell efficiency/stability based on the results presented in chapter 6.5.2. For this reason the impact of water is not discussed here.

	propionitrile (99 %) /%	propionitrile (99.5 %) /%	propionitrile distilled /%
water content	0.09	0.11	0.22

Table 6.14: water content of different propionitrile batches

The initial solar cell parameters and the aging of the cell at 80 °C for 1100 h in darkness is depicted in Fig. 6.71. It can be seen that the total content of impurity correlates quite well with the conversion efficiency and the open circuit potential. No efforts were undertaken to distinguish between the different contaminants in the electrolyte though it would be interesting to see which compound contributes to what extend. The following trends were identified:

1) The initial conversion efficiency $E_{intitial}$ was about 3 % higher for the distilled propionitrile compared to the less pure batches and the degradation rate ($E_{initial}/E_{final}$) was found to be only 20 % compared to 25 %. That means both initial efficiency and degradation rate was significantly improved if the solvent was distilled.

2) The higher efficiency was mainly due to a better fill factor and a higher open circuit potential. The open circuit potential was initially about the same for all three solvent batches. However, after exposure to 80 °C, the V_{OC} decreased by ca. 110 mV for the distilled

propionitrile, by 146 mV for the 99 % propionitrile and by 165 mV for the 99.5 % propionitrile. That indicates that the chemically induced alteration by the impurities needs some thermal activation before an effect in the solar cell parameter is visible.

3) The lower V_{OC} was partly compensated by a higher short circuit current. That indicate that the decreased V_{OC} is at least partly due to a shift of the flat band potential in the TiO_2. A downward shift increases the driving force for electron injection.
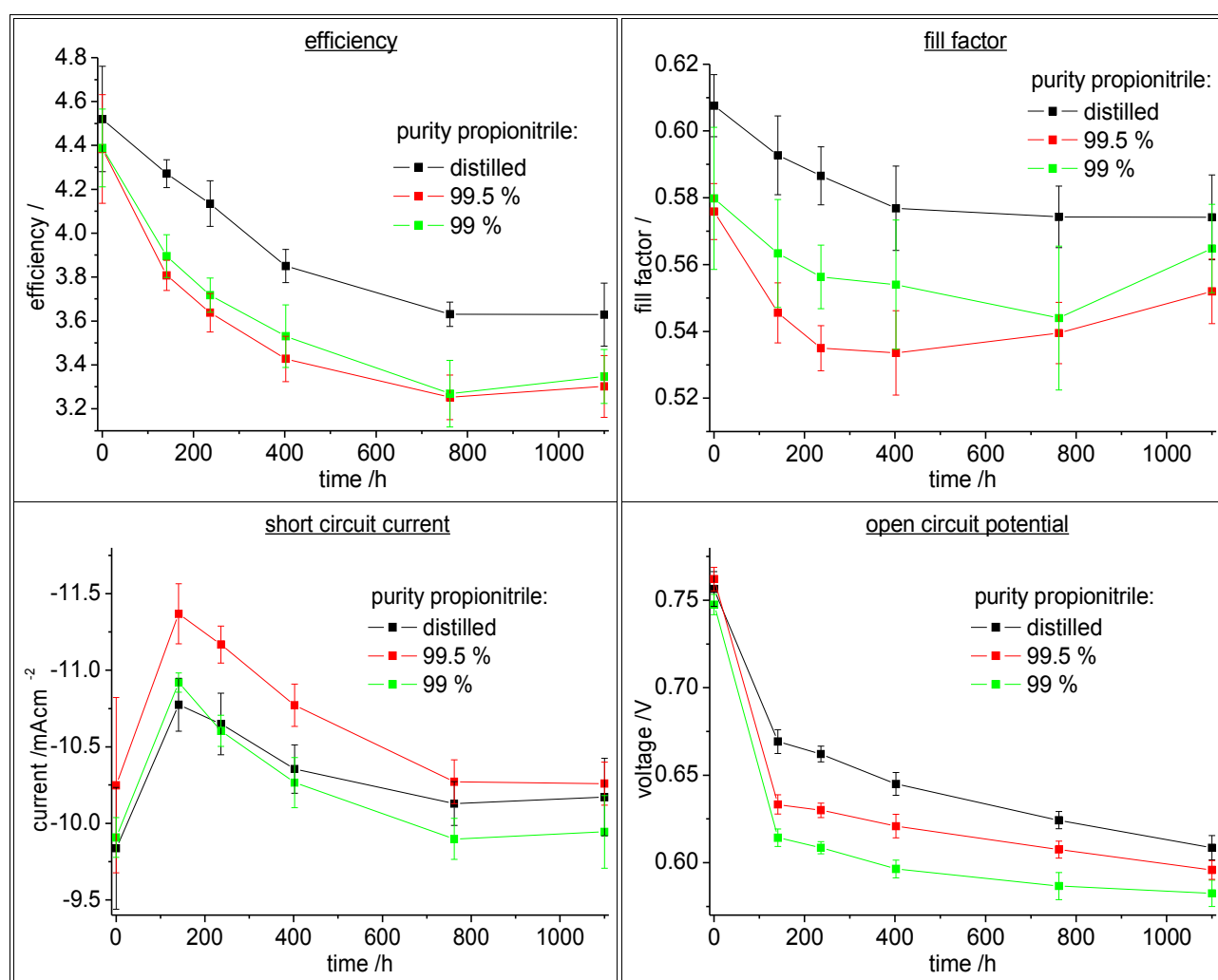

Fig. 6.71: influence of solvent purity on the photovoltaic performance: solar cell parameters of DSSC after 1100 hours at 80 °C in darkness: a) efficiency; b) fill factor; c) short circuit current; d) open circuit potential

The open circuit potential can be either altered by an enhanced recombination rate or by a shift of the TiO_2 conduction band. Transient photovoltage measurements were used to determine the band shift of the TiO_2 due to the adsorption of impurities. Figure 6.72a shows the capacitance of the electrode as a function of the photopotential after 141 h exposure to 80 °C. Under the assumption

that the impurities change the properties of the TiO_2/electrolyte interface only by inducing or withdrawing electron density, the horizontal displacement is a measure of the shift of the Fermi level. It can be seen that impurities shift the Fermi level by ca. 52 mV for the 99.5 % propionitrile and 42 mV for the 99 % propionitrile. Looking at the V_{OC} in Fig. 6.71d at the same time a 55 mV and 36 mV lower open circuit potential was measured. Thus the band shift is believed to be the main reason for the lower V_{OC}. Indeed the recombination rate is only modestly affected by the impurities and changed only by maximum 25 % (6.72b).
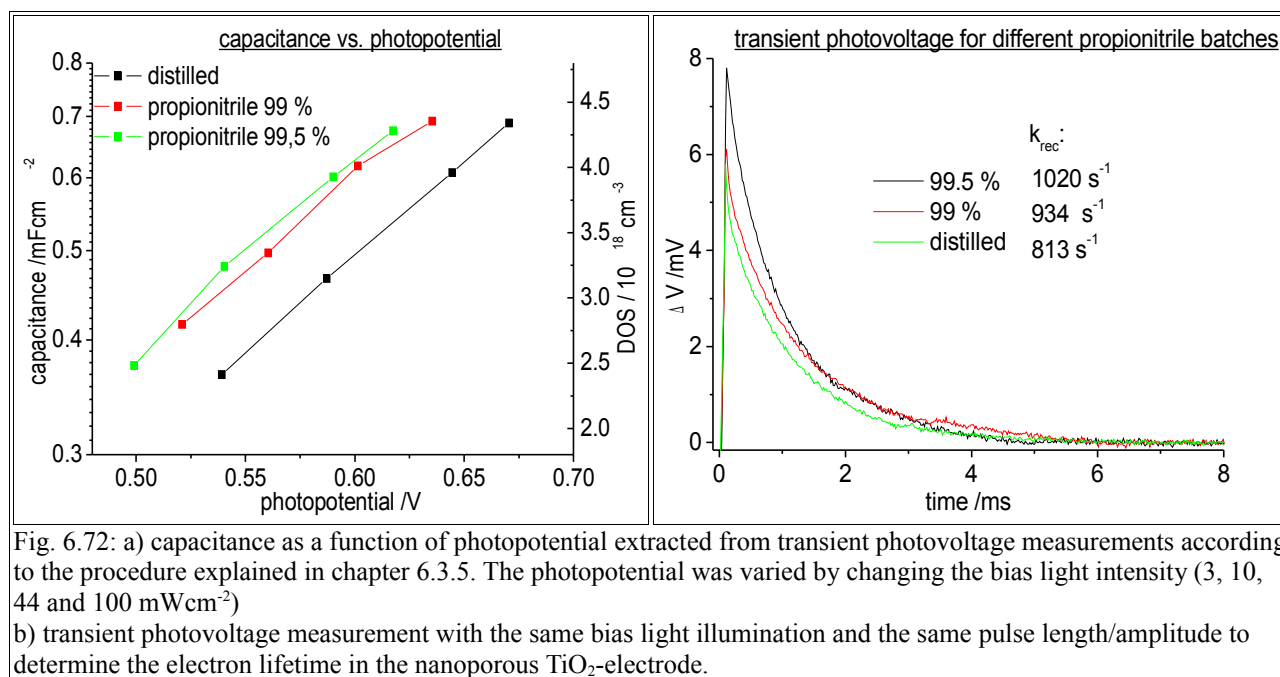

Fig. 6.72: a) capacitance as a function of photopotential extracted from transient photovoltage measurements according to the procedure explained in chapter 6.3.5. The photopotential was varied by changing the bias light intensity (3, 10, 44 and 100 mWcm^{-2})
b) transient photovoltage measurement with the same bias light illumination and the same pulse length/amplitude to determine the electron lifetime in the nanoporous TiO_2-electrode.

6.5.6 TiO$_2$ layer thickness

The influence of the TiO_2-electrode thickness on the stability of dye sensitized solar cell (DSSC) has not been discussed in the literature so far. For the initial conversion efficiency, there is an optimal layer thickness for each electrolyte/dye combination for the following reason: if the TiO_2-layer is too thin, the absorption of the sensitizer remains poor and only a fraction of the incident photons is injected. As a consequence, the short circuit current is low. If one increases the layer thickness d, the recombination rate increases proportionally with d. However, the absorption saturates at some point and thus the fraction of electrons that recombine increases. As a result a low open circuit potential is typically observed. The optimal layer thickness is believed to be between 12 - 14 µm [233].

In this chapter experimental evidence is given for these empirical findings and the effect of the layer thickness on long term stability at 80 °C in darkness is discussed.

Fig. 6.73 shows the initial I-V-curves of DSSCs with different TiO_2-layer thickness assembled according to the procedure described in chapter 6.5.1. For the electrolyte/dye combination in this experiment, the conversion efficiency increased with increasing layer thickness and up to 16 µm layer thickness no maximum is reached. As predicted the increase was due to a better short circuit current, which overcompensated the loss of open circuit potential. Interestingly a significant correlation between the fill factor and the layer thickness was found. The fill factor decreased by ca. 10 % as the layer thickness increased from 4 µm to 16 µm.
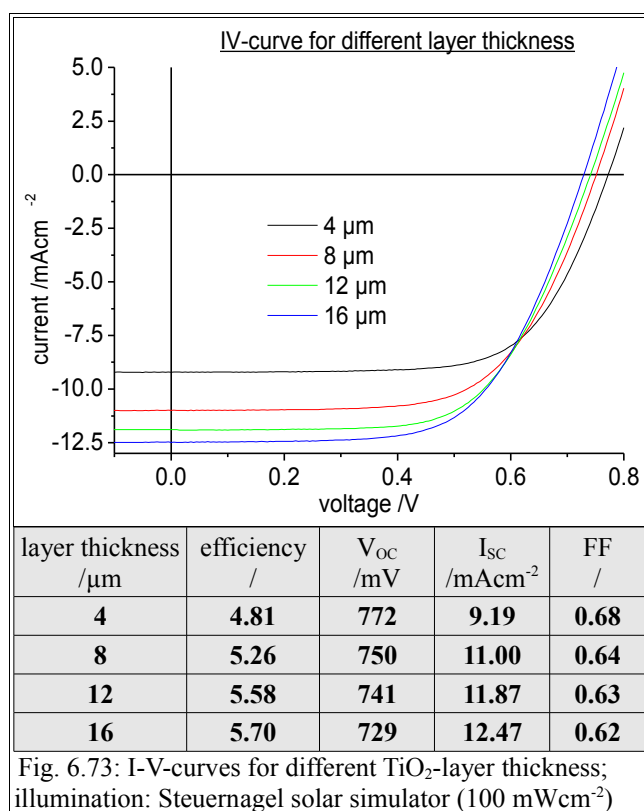

layer thickness /µm	efficiency /	V_{OC} /mV	I_{SC} /mAcm^{-2}	FF /
4	4.81	772	9.19	0.68
8	5.26	750	11.00	0.64
12	5.58	741	11.87	0.63
16	5.70	729	12.47	0.62

Fig. 6.73: I-V-curves for different TiO_2-layer thickness; illumination: Steuernagel solar simulator (100 mWcm^{-2})

During the staining of the electrode the correlation between the layer thickness and the dye uptake was measured. In earlier experiments some evidence was found that the TiO_2-pores were partly clogged by dye-agglomerates, which resulted in an incomplete dye coverage near the front electrode. However, by heating the dye solution to 40 °C this problem can be circumvented. As a result a linear increase of the dye uptake with the layer thickness was observed as can be seen in Fig. 6.74a. The factor of proportionality was found to be $1.15*10^{-8}$ mol*cm^{-2}*µm^{-1}.

Having proven a uniform dye distribution in the layer the incident photon to current conversion efficiency (IPCE) of the layer was measured. As can be seen in Fig. 6.74b, the IPCE did not increase with the layer thickness as long as the absorption of the layer is high. This is true for the peak in the UV-region at $\lambda \approx 350$ nm, which is a combination of direct band gap excitation of the TiO_2, surface trap state excitation and injection of the dye ($\alpha_{305\ nm} = 3.73*10^4$ $M^{-1}cm^{-1}$ in acetonitrile). Going to longer wavelength the absorption coefficient of the film becomes smaller and thus a thicker layer is needed for complete absorption. The absorbance A of the layer correlates very well with the IPCE indicating that the charge extraction efficiency under short circuit operation does not depend on the layer thickness, which means that the diffusion length is significantly longer than the thickest electrode (16 µm) in this experiment.
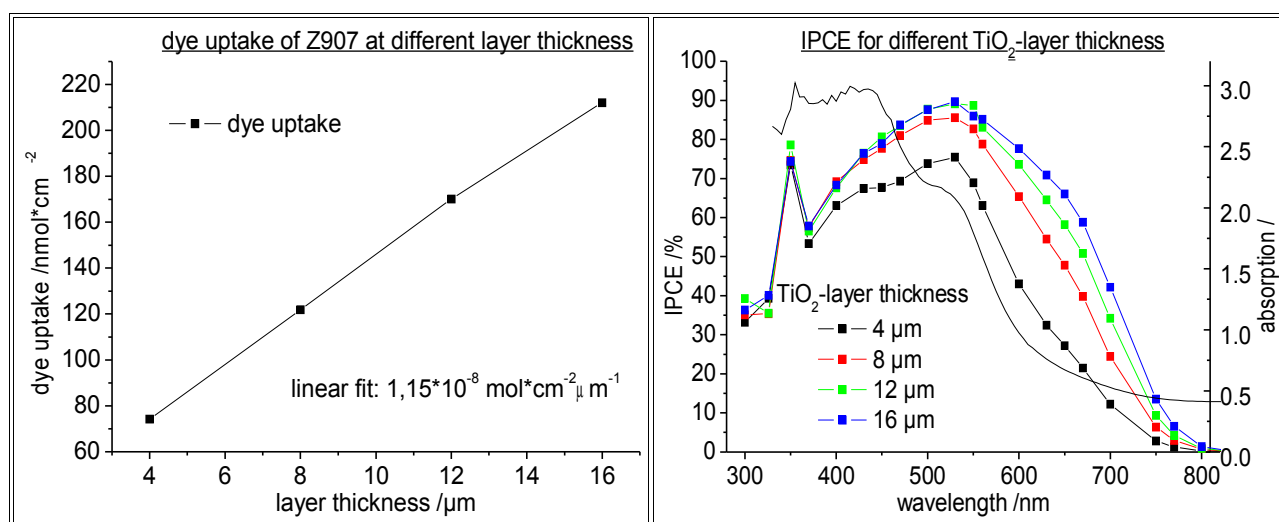

Fig. 6.74: a) dye uptake as a function of layer thickness: concentration: $5*10^{-4}$ M Z907-solution in t-butanol:acetonitrile 1:1
b) IPCE of DSSC with different layer thickness (line and symbol) and absorption of a cell with 8 µm film thickness using an integrating sphere (line).

It was tried to fit transient photovoltage measurements with the model developed in chapter 6.3. Calibration measurements of the effective diffusion coefficient D_{eff}, the recombination rate k_{rec} and the capacitance of the titanium dioxide TiO_2 as a function of the photopotential were done analogue to the procedure in chapter 6.3. Since the calibration curves were very similar, they are not shown here. The photovoltage transient of a 4 µm and 16 µm are compared in Fig. 6.75. The following conclusions can be drawn:
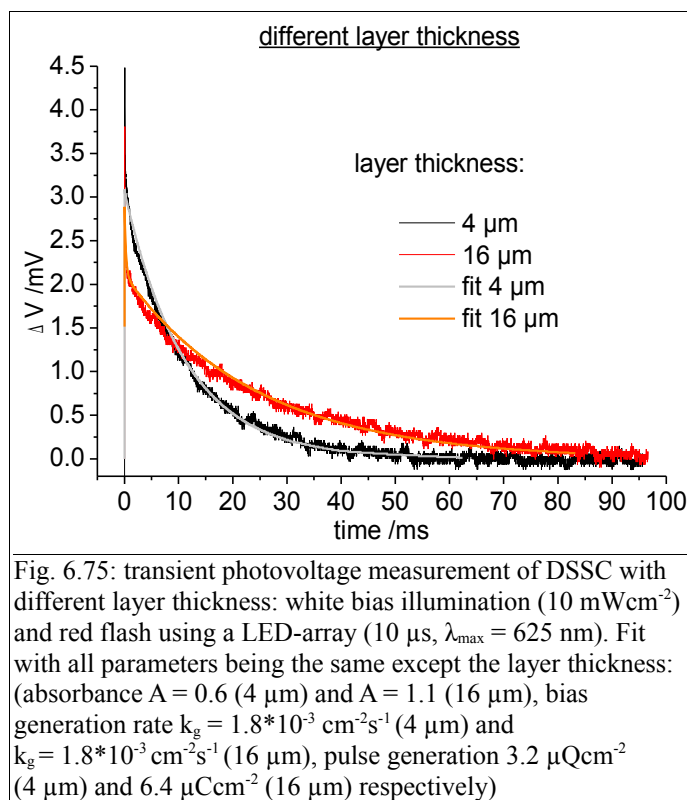
1) Since the absorption obeys Lamber-Beers-Law less electrons are injected with increasing distance to the front contact. Thus immediately after the pulse was triggered, the electrons

start to diffuse along the concentration gradient into the layer and the photopotential significantly decreases within the first 100 µs. This effect is more pronounced for the thicker layer since the capacitance increases with increasing layer thickness.

2) The different recombination rate constants are attributed to the different photopotential. The V_{OC} of the 4 µm thick layer is 39 mV higher compared to the 16 µm thick layer at the same bias illumination. The corresponding recombination rate is k_{rec} = 39.8 s^{-1} (4 µm) and 15.4 s^{-1} (16 µm) respectively. If the transient is measured at the same photopotential by adjusting the bias illumination, no difference in the recombination rate was found. The different photopotential can be rationalized qualitatively by looking at number of injected photons per trap state. Since the number of trap states increases linearly with the layer thickness but the number of injected electrons n_{Inj} correlate with the layer thickness d like

$$n_{Inj} \propto \frac{1}{A} * (1 - e^{-A*d})$$ (6.83), A = absorbance of the layer

less electrons per µm are injected with increasing layer thickness. As a consequence the open circuit potential decreases.

Fig. 6.75: transient photovoltage measurement of DSSC with different layer thickness: white bias illumination (10 mWcm^{-2}) and red flash using a LED-array (10 µs, λ_{max} = 625 nm). Fit with all parameters being the same except the layer thickness: (absorbance A = 0.6 (4 µm) and A = 1.1 (16 µm), bias generation rate k_g = 1.8*10^{-3} cm^{-2}s^{-1} (4 µm) and k_g = 1.8*10^{-3} cm^{-2}s^{-1} (16 µm), pulse generation 3.2 µQcm^{-2} (4 µm) and 6.4 µCcm^{-2} (16 µm) respectively)

Finally the long term stability at 80 °C was measured for 500 h in darkness. The solar cell parameters as a function of time are given in Fig. 6.76. It was found that the degradation occur basically in two time frames: within the first 70 h, the degradation rate correlate with the layer thickness. Then a slow degradation of ca. 6 % is found for all cells in the time frame between 70 h and 480 h. The degradation is mainly due to a lower open circuit potential, which decreased between 110 mV (16 µm) and 140 mV (4 µm) (Fig. 6.76 d). At the same time a steady increase of the short circuit current was observed (between 4 % - 6 %) (Fig. 6.76 c), which could partly compensate the lower open circuit potential.

The initial decrease is believed to be due to the partial desorption of the sensitizer. Analysis of the electrolyte with UV/Vis-spectroscopy revealed the presence of the sensitizer. The quantity could not be determined since the signal was superimposed by the absorption of iodine. It is interesting to note that the cell performance was much more effected for the thinner TiO$_2$-electrode (4 µm: -7.9 %, 8 µm: -9.5 %) compared to the thicker electrodes (12 µm: -3.4 %, 16 µm: -3.6 %). That stresses the importance of the sensitizer as a buffer if chemical degradation occurs: Theoretical considerations revealed [234] that the lifetime of a DSSC can be significantly enhanced if additional sensitizer is introduced.
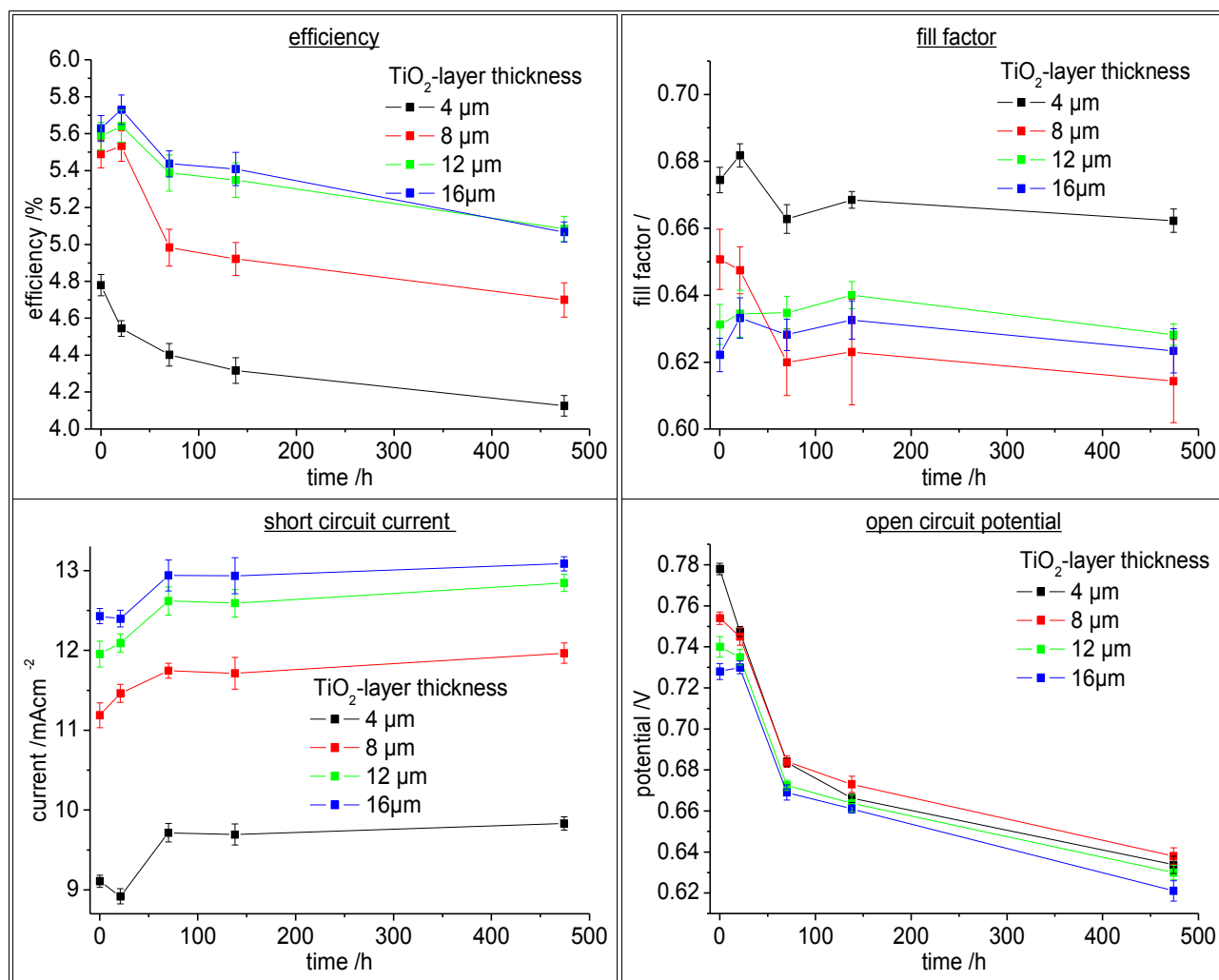
Fig. 6.76: influence of TiO$_2$ layer thickness on the photovoltaic performance: solar cell parameters of DSSC after 480 hours at 80 °C in darkness: a) efficiency; b) fill factor; c) short circuit current; d) open circuit potential

6.6 Carbon counter electrodes

A conventional dye sensitized solar cell (DSSC) employs platinum at the counter electrode to catalyze the reduction of triiodide. The deposition technique (sputtering, chemical bath deposition, ...) has a strong influence on the catalytic activity of the platinum. For most preparation modes, a load of 50 mg/m² is sufficient and further deposition does not increase the cell performance. The sheet resistivity of the underlying substrate decreases with increasing Pt-loading (e.g. 5 times for 250 mg/m²) [235], but this approach to lower the series resistance is not applicable due to the high price of the noble metal. Though platinum has become a standard for DSSC counter electrodes there are several disadvantages associated with this metal:

–   its chemical stability in long term tests has not been proven yet. Thermodynamic calculations accompanied with ex situ measurements have shown that Pt can dissolve in iodine containing solutions [236].

$$\boxed{Pt + 2I_2 \rightarrow PtI_4} \quad (6.84)$$
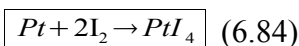
One typical observation when exposing DSSCs to high temperature is that the open circuit potential decreases with time. Though other mechanisms also contribute to the V_{OC} decay (e.g. shift of TiO_2 conduction band), one reason is believed to be that weakly bounded platinum dissolves in the electrolyte, diffuses to the front electrode where it enhances the recombination reaction of TiO_2-conduction band electrons with the electrolyte and thus lowers the open circuit potential.

–   The deposition is either very expensive (sputtering) or requires a firing step (CBD). The latter restricts the choice of substrates to heat resistant materials like glass.

–   For large area applications the availability of platinum might not be ensured. For 1 GW_p about 1000 kg platinum are needed.

Most other metals (e.g. gold, s. chapter 6.4.6) are not stable enough towards the iodine electrolyte.

Carbon as a cheap, abundantly available material with high catalytic activity and good chemical stability has therefore been developed as an alternative. Already in 1996, small monolithic modules

of ca. 3 cm² have been developed with a conversion efficiency of 5.3 % [237]. In theses cells a ca. 50 μm thick layer of a graphite/carbon black mixture with TiO_2 as a binder was used as a counter electrode. Today a conversion efficiency of 9.1 % with a similar technique has been achieved for small area cells (0.16 cm²) [156]. However, the use of TiO_2 as a binder requires a temperature treatment of 450 °C, which allows only glass to be used as a substrate. Lower temperature approaches with different carbon pastes gave about 4 % efficiency, which was about the same as the reference cells with Pt-counter electrodes [238]. Omitting a firing step opens a window for a large variety of conducting plastic substrates, for which the best efficiencies are 4.9 % at the moment [239].

6.6.1 Development of highly conducting carbon layers

The focus of the present approach was to develop a carbon counter electrode, that acts both as a catalyst and a conductor and can be deposited at temperatures <150 °C. The following requirements had to be fulfilled.

– a low sheet resistance of ca. 10 Ω/□ (the resistance of FTO).

– good mechanical stability and adhesion to the substrate (glass or plastic)

– a catalytic activity comparable to that of platinum

First different carbon suspensions were screened for their mechanic and electric properties. It was decided to use a carbon glue as an adhesive, which allowed room temperature preparation. The glue employed in this study was C-Leit from Provac GmbH, which contains polyacryl-coated carbon particles in a viscous paste of xylene and toluene. The glue was mixed with different carbon powders and the paste was suspended in isopropanol by ultrasonic treatment for 1 min (table 6.15). Then the suspension was spread on a glass substrates with the doctor blade method and dried at room temperature. By repeating this step the layer thickness could be varied. Afterwards the sheet resistance was determined with the four-point-method, the sheet thickness with a profilometer and the mechanical stability by scratching with a scalpel.

Except Norit SX Ultra CAT, for which no preparation procedure was found, all other carbon powder

are so-called furnace-blacks, which are made by incomplete combustion of aerosols. Depending on the number of double bounds they contain, these carbon powders might irreversibly take up a certain amount of iodine from the electrolyte. However, the kinetics at room temperature are slow and a significant iodine uptake is believed to be negligible initially. This might be different when in long term stability tests at higher temperature.

carbon	surface area		layer thickness	sheet resistance	amount	mechanical stability and scratch resistance
	micropores	mesopores				
	m^2/g		µm	$\Omega/\square$	mg	
Vulkan Kohlenstoff 1996 (Cabot) Vulcan XL72R No3	150	100	30	75	15	sufficient
Norit SX Ultra CAT 94064-3	600	300	50	500	35	poor
Printex XE 2 Degussa 950812	300	800	25	20	18	good
Ketjen Black RC 300 (pH 8-10)	500	350	35	150	22	sufficient

Table 6.15: x mg of the respective carbon powder was mixed with 150 mg of C-Leit (Provac GmbH). 1 ml isopropanol was added and the suspension was homogenized for 1 min in an ultrasonic bath. The viscosity of the suspension determined the amount of carbon that was added. No correlation between the surface area of the carbon powder and the viscosity of the suspension was found. The table gives, for each carbon powder, the values for the layers with the lowest sheet resistance.

According to table 6.15 the following trends were found:

– the mechanical stability and scratch resistance decreased with an increasing amount of carbon powder. Without any carbon powder, the layer was very stable and can be hardly scratched with a scalpel. Good stability means that the layer was not scratched by a pencil, sufficient stability means it was stable when touching it with a glove and poor stability that cracks could be seen even by visible inspection. Since all carbon particles are charged to some extend and no effort was undertaken to find the isoelectric point, repulsion of the carbon particles were suppressed by adding binder (the carbon glue). With an increasing fraction carbon glue, the layer became more and more stable.
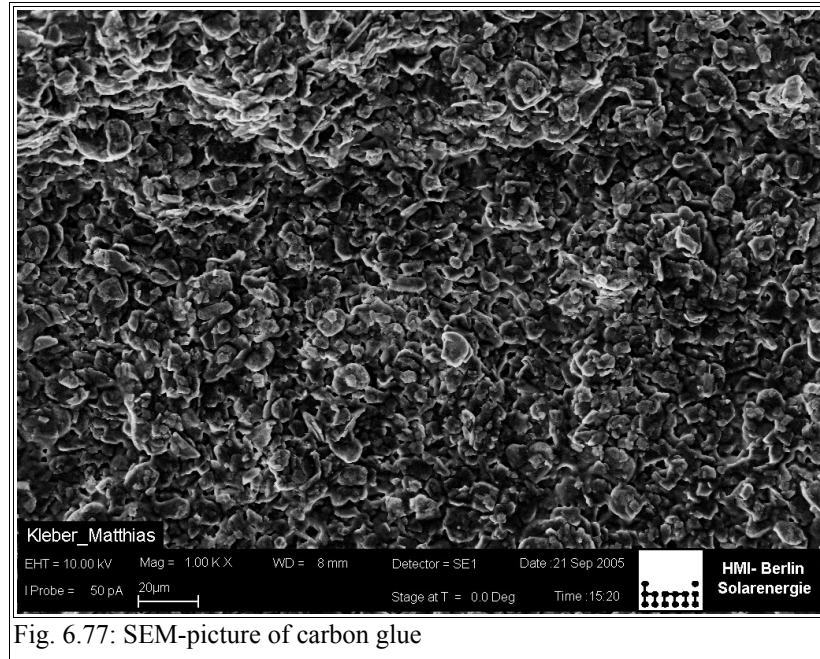
Fig. 6.77: SEM-picture of carbon glue

– the conductivity increases with increasing amount of carbon powder. From SEM-picture 6.77 it can be seen that the carbon glue forms big flakes of several μm thickness. The very small carbon particles penetrate the pores of the carbon glue matrix (particle size distribution Fig. 6.78) and significantly increase the percolation pathways for electrons. It was found that the conductivity of the carbon powder itself is less important and the resistance of the layer is mainly determined by its mechanical properties.

Fig. 6.78: particle size distribution of different carbon-blacks
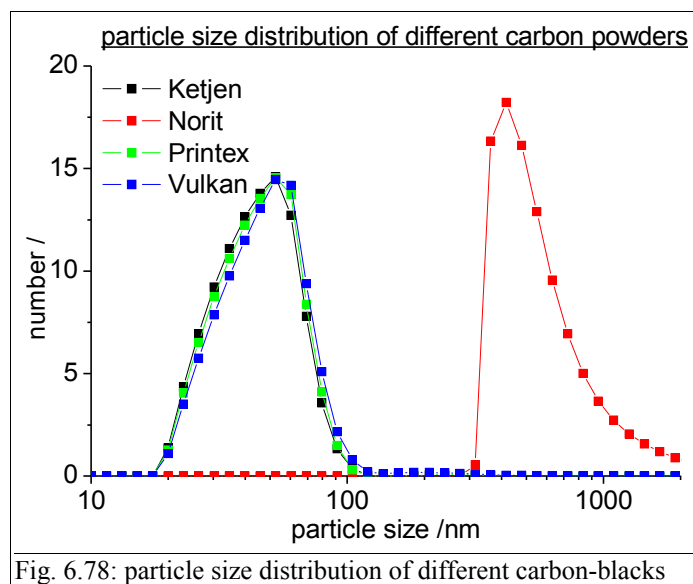
– the mechanical stability decreased with increasing layer thickness because tension within the layer was less compensated by the adhesion to the substrate.

To summarize, a compromise had to be find between mechanical stability and sheet resistance. As Printex 2 performed best in the screening tests it was chosen for further experiments. Two parameters were checked systematically in order to find the best layer composition: the layer thickness and the influence of heat treatment after preparation.
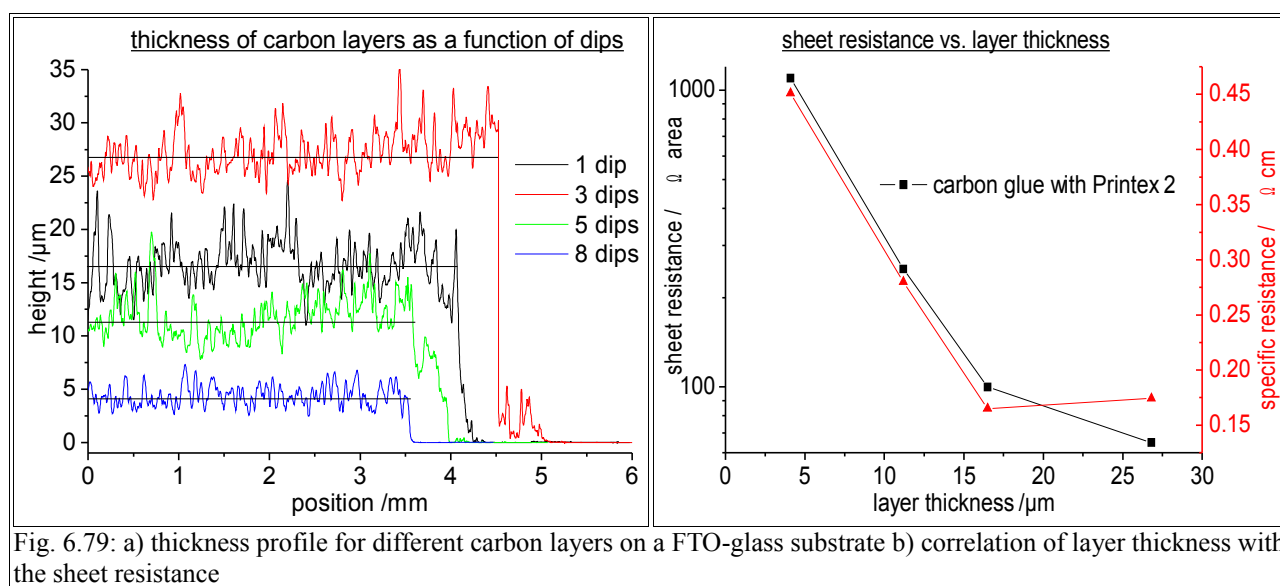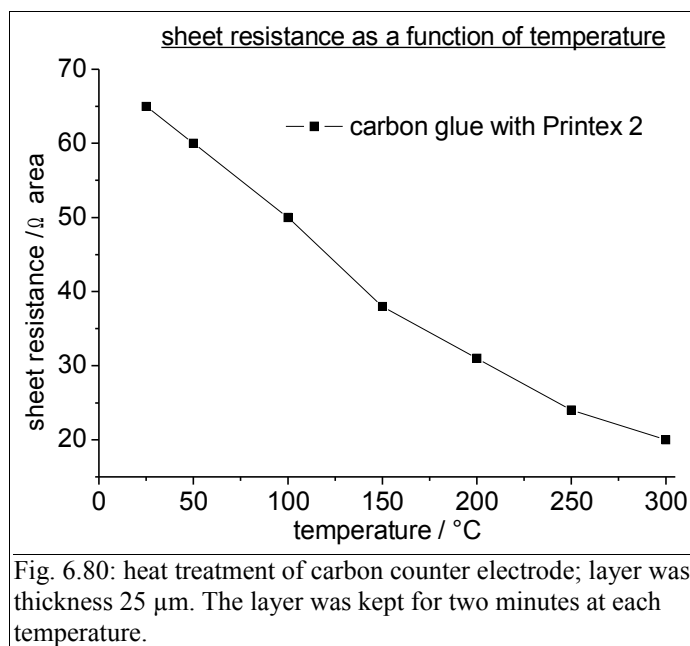

Fig. 6.79: a) thickness profile for different carbon layers on a FTO-glass substrate b) correlation of layer thickness with the sheet resistance

As can be seen in Fig. 6.79b the sheet resistance decreased exponentially with increasing layer thickness d for d <17 µm. That again indicates that percolation pathways play a dominant role and the conductivity of each individual particle is less important. Otherwise a linear increase would have been expected and the specific resistance would have been constant. Going from 16.5 µm to 27 µm a slight increase in the specific resistance was noticed. That is likely due to the formation of small cracks that could be seen under the microscope. Layers >30 µm were instable with Printex 2 and could thus be not characterized.

It turned out that the sheet resistance decreased further if the layer was exposed to higher temperatures for some time. From Fig. 6.80 one can see that the sheet resistance decreased almost linear with the temperature for an interval 25 °C < T < 300 °C. The time of exposure did not influence the sheet resistance. For 1, 2, 5, 20 minutes, the same decrease was found. It can be concluded reorganization in the layer is a rather fast process. For temperatures <150 °C it is expected that the higher conductivity is due to solvent evaporation. 2-propanole as the main

component of the suspension and xylene/toluene as the main ingredients in the carbon glue evaporate at 82 °C and around 140 °C respectively. It was found that if the layer was kept at 20 °C for a few days the resistance decreased about the same. The same effect was observed when the layer was kept at reduced pressure (10^{-4} mbar) for 30 min.

Fig. 6.80: heat treatment of carbon counter electrode; layer was thickness 25 μm. The layer was kept for two minutes at each temperature.

At temperature >150 °C the particles start to sinter. The effect is the same as for the evaporation of the solvent: the resistance between the particles and thus the overall sheet resistance decreases. For a temperature >250 °C the layer became mechanically instable. This is not reflected in the sheet resistance, so most likely the instability is due to different thermal expansion coefficients of the substrate and carbon layer and the carbon simply peels off the substrate.

Finally the carbon layers were exposed to the standard electrolyte (0.6 M PMII, 0.5 M TBP, 0.1 M I_2 in acetonitrile) for one hour in order to check if swelling affects the mechanical stability and/or the sheet resistance. It was found that the sheet resistance increased about 30 % after electrolyte treatment and the mechanical stability slightly decreased. To test which component caused this decrease each component was tested separately.

It turned out that iodine had by far the most significant effect. It is assumed that physisorption of iodine on the carbon particles either affects the surface conductivity or the resistance between different carbon particles. The base t-butylpyridine (TBP) and the solvent did neither affect the

mechanical stability nor the sheet resistance, which indicates that the carbon glue is already a good choice. Other groups found an increase of the sheet resistance by a factor of two upon electrolyte exposure [237]

To summarize carbon layers consisting of a carbon glue and a carbon powder were made with a sheet resistance as low as 20 $\Omega/\square$ (300 °C) and about 36 $\Omega/\square$ (150 °C). The electric properties are mainly governed by the composition of the carbon paste and the thickness of the layer. Although the conductivity of FTO (10 $\Omega/\square$) was not reached it should be noted that the employment of different carbon powders, deposition techniques, and or other additives leaves enough room for optimization. Thus it is believed that the employment of a carbon glue in combination with a carbon powder might be an alternative to the platinized FTO-substrate.

6.6.2 Dye sensitized solar cells with carbon counter electrodes

Having developed a counter electrode with a low sheet resistance, solar cells were made in order to test the catalytic activity of the electrode. A sketch of the cell layout is shown in Fig. 6.81
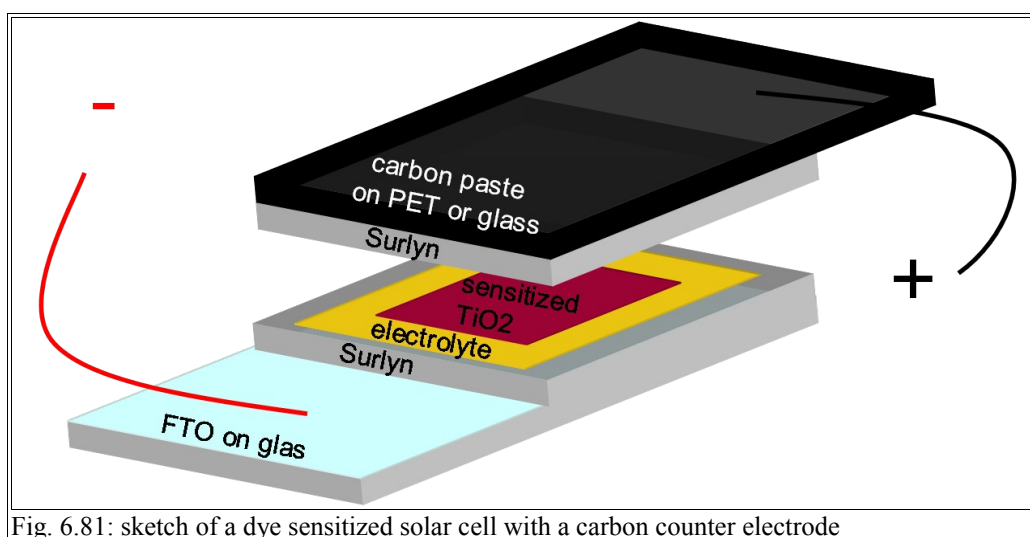

Fig. 6.81: sketch of a dye sensitized solar cell with a carbon counter electrode

In principal the general procedure of cell assembly was followed as described in chapter 5 except two modifications. In order to enhance the adhesion of the carbon layer to the substrate, the glass

surface was roughened with a sand blaster prior to the deposition of the carbon layer. Secondly the thickness of the Surlyn® foil was 60 μm instead of 25 μm to avoid any contact between the counter electrode and the sensitized TiO_2. Details are given in table 6.16.

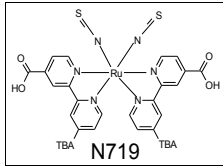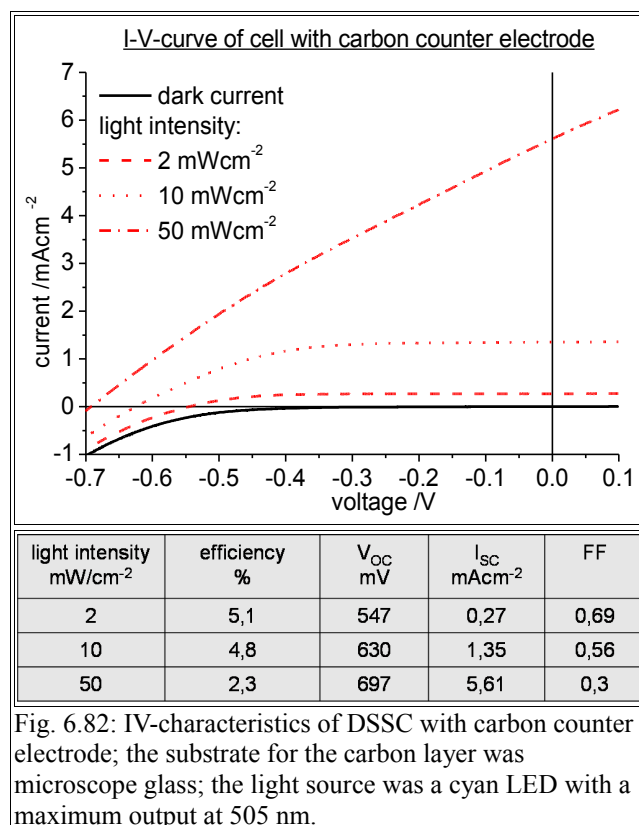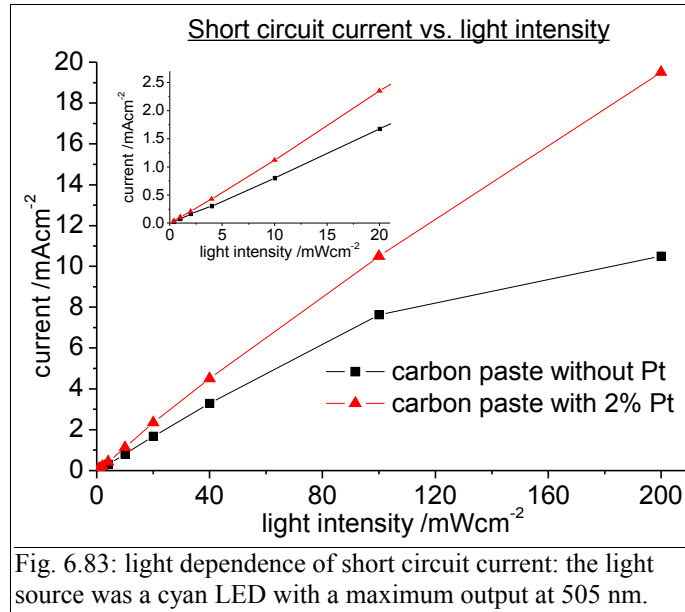| TiO_2-layer	carbon layer	sensitizer	electrolyte	cell area
23 nm anatase particles layer thickness 9,7 μm $TiCl_4$ post-treatment deposition by screen printing	150 mg C-Leit (Provac GmbH) 18 mg Printex 2 1ml 2-propanol layer thickness: 25 μm deposition by doctor blade method heated to 250 °C for 5 min after deposition sheet resistance: 21 $\Omega/\square$ (without electrolyte)	N719	0.6 M PMII 0.5 M TBP 0.1 M I_2 in acetonitrile	1 cm^2

Table 6.16: dye sensitized solar cells with carbon counter electrodes

From Fig. 6.82 one can see that a respectable conversion efficiency of 5.1 % was achieved at 2 $mWcm^{-2}$ light intensity. Furthermore a linear increase of the short circuit current with the light intensity was observed between 2-10 $mWcm^{-2}$ indicating that no transport limitation is present at low light intensity (Fig. 6.83). Between 10-50 $mWcm^{-2}$ the short circuit current increased only by a factor of 4.1, which shows that there is a loss mechanism at higher light intensities. More importantly the fill factor decreases significantly so that the conversion efficiency drops to 2.3 % at 50 $mWcm^{-2}$. The following explanations are proposed.

I-V-curve of cell with carbon counter electrode

light intensity mW/cm^{-2}	efficiency %	V_{OC} mV	I_{SC} mAcm^{-2}	FF
2	5,1	547	0,27	0,69
10	4,8	630	1,35	0,56
50	2,3	697	5,61	0,3

Fig. 6.82: IV-characteristics of DSSC with carbon counter electrode; the substrate for the carbon layer was microscope glass; the light source was a cyan LED with a maximum output at 505 nm.

1) At higher light intensity the catalytic activity of the carbon paste is not sufficient to support the short circuit current. A large overpotential at the counter electrode builds up, which explains the poor fill factor and the low short circuit current. To test this assumption, a cell containing a carbon paste with 2 % Pt was made and compared to the reference cell without Pt. As can be seen in Fig. 6.83, the short circuit current increased linearly with the light intensity up to 20 mAcm^{-2}. However, adding platinum to the carbon matrix is not an option for this device as some of it dissolves in the electrolyte and the open circuit potential is much lower compared to the reference cell. Future investigations have to focus on the optimization of the carbon catalyst for improving the cell efficiency at higher light intensity.

Fig. 6.83: light dependence of short circuit current: the light source was a cyan LED with a maximum output at 505 nm.

2) the series resistance is higher compared to a cell containing FTO as a substrate. The sheet resistance is assumed to be 27 $\Omega/\square$ (21 $\Omega/\square$ without electrolyte, 30 % increase after swelling), which is 2.7 times higher than the FTO. The higher series resistance R_S is reflected by the flat slope of the IV-curve near V_{OC}. In the one diode model, R_S would be

$$R_S = [\frac{\delta U}{\delta I}]_{V_{OC}} \quad (6.85)$$

3) the parallel resistance R_P is also lower compared to a cell with a FTO/Pt-counter electrode. For an one diode model R_P is

$$R_P = [\frac{\delta U}{\delta I}]_{I_{SC}} \quad (6.86)$$

It is believed that large carbon particles (>60 μm) can short circuit the cell at some points. From Fig. 6.77 it can be seen that the surface of the carbon layer is very rough and from microscope images it could be seen that some big particles could not be downsized by ultrasonic treatment. Yet it is difficult to estimate R_P since the IV-curve cannot be fit with an one diode model and $(\delta U/\delta I)_{Isc}$ is also affected by the catalytic activity at the carbon counter

electrode. However, to exclude this problem, big carbon particles should be filtered in the future.

Next the layer thickness of the carbon counter electrode was varied to check the influence on the photovoltaic performance. In this experiment, the carbon paste was deposited on a FTO-coated glass. This way, only the catalytic activity was tested and not the electric conductivity. Otherwise the cell composition was as described in table 6.16. From Fig. 6.84 it can be seen the catalytic activity increased significantly with increasing layer thickness. For thin layers (5-15 μm) an overpotential at the counter electrode builds up. This is reflected by the small currents around V_{OC} where the driving force for triiodide reduction is low and an efficient catalyst is needed that reduces the overpotential. On the other hand, it can be seen that the open circuit potential increases with decreasing layer thickness. Two reasons might contribute to this observation:

– the carbon layer change the redox potential of the iodine/iodide electrolyte. As mentioned before it is believed that some triiodide adsorbs on the carbon layer, which shifts the potential of the electrolyte more negative. With increasing layer thickness more triiodide is adsorbed and the potential difference between TiO_2 conduction band and the electrolyte becomes smaller

– t-butylpyridine (TBP) might also adsorb on the carbon particles. With decreasing TBP-concentration the TiO_2 conduction band shifts upwared and again the open circuit potential decreases.

I-V curve for different carbon layer thicknesses

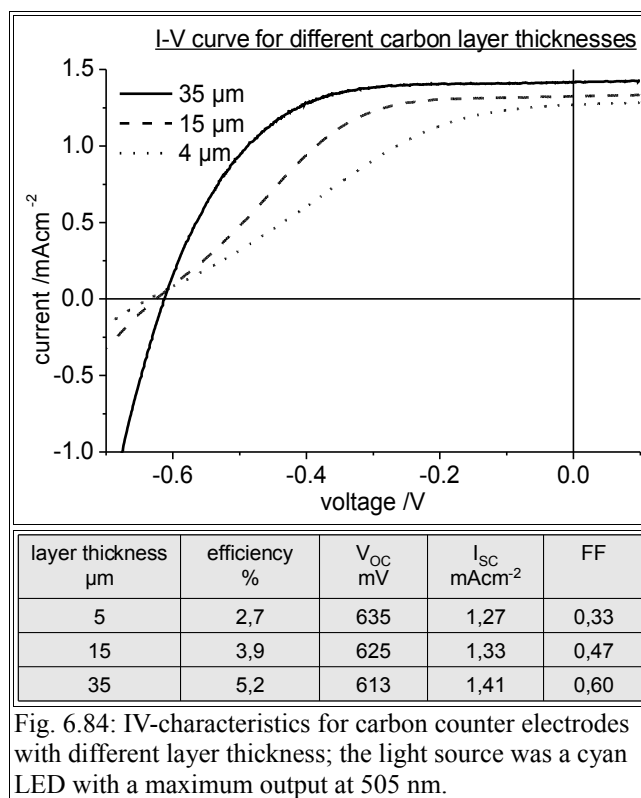| layer thickness μm	efficiency %	V_{OC} mV	I_{SC} mAcm^{-2}	FF
5	2,7	635	1,27	0,33
15	3,9	625	1,33	0,47
35	5,2	613	1,41	0,60

Fig. 6.84: IV-characteristics for carbon counter electrodes with different layer thickness; the light source was a cyan LED with a maximum output at 505 nm.

It should be noted that for a reference cell with all parameters being the same except a Pt-counter electrode, the open circuit potential is between 50-75 mV higher compared to a carbon counter electrode. So triiodide- and TBP-adsorption seems to play a significant role in DSSC with carbon counter electrode and it is likely that a different electrolyte composition is needed in these devices.

Finally it was tried to use flexible plastic instead of glass as a substrate for the counter electrode. The advantage with this cell layout is that very fast role-to-role processes become applicable and the weight of the cell is significantly reduced. This is expected to reduce the overall cost per W_P. On the other hand, it should be noted that standard polymers are permeable for water and gases to some extend and cannot be exposed to temperatures more than ca. 150 °C. For the following experiment Polyethylenterephthalate (PET) was used. PET is a flexible but very durable polymer with a tensile strength of about 80 MPa. It is resistant to most organic solvents (alcohols, aromatic hydrocarbons, acids...) and in particular to the electrolyte chosen (acetonitrile, 0.5 M TBP, 0.6 M PMII, 0.1 M I_2). It contains about 0.7 % water when equilibrated with water and has a permeability for water of $1*10^{-11}\,s^{-1}Pa^{-1}$. Experiments (chapter 6.5.2) have proven that a certain content of water does not influence the cell performance and cell stability, so no extra sealant was used. The thickness of the PET-foil was 200 μm. Again the composition was as described in table 6.16. Since the heat capacitance of the PET substrate was much lower compared to glass, the time of lamination was

reduced from 90 s to 15 s. Fig. 6.85 shows the IV-curves of a plastic counter electrode and a reference glass counter electrode. It can be seen that the short circuit current and the open circuit potential is about the same for both substrates. However, the fill factor is about 40 % less. This is because the sheet resistance (without electrolyte) was almost two times higher (36 Ω/□ instead of 20 Ω/□) as the electrode was only heated to 150 °C. Besides this intrinsic problem it was found that the adhesion of the carbon layer to the plastic was less stable compared to the glass substrate. Furthermore surface analysis with a profilometer revealed that the surface is not perfectly flat with deviations of up to 50 µm. The distance between the counter electrode and the titanium dioxide layer was in average about 27 µm larger compared to the glass substrate, which means that additional ohmic losses within the electrolyte might contribute to the poor fill factor. It is bothering that even with a small active cell area of 1 cm^2 it seems to be difficult to control the distance between front and counter electrode. For larger modules this might be a serious problem and an additional spacer might have to be introduced.

To summarize it was shown that dye sensitized solar cells with carbon counter electrodes that act both as a catalyst and as a conducting layer can be made with remarkable conversion efficiencies of 5.1 %. Though in principle a large variety of substrates might be employed in this cell layout, glass was superior to any plastic substrate.

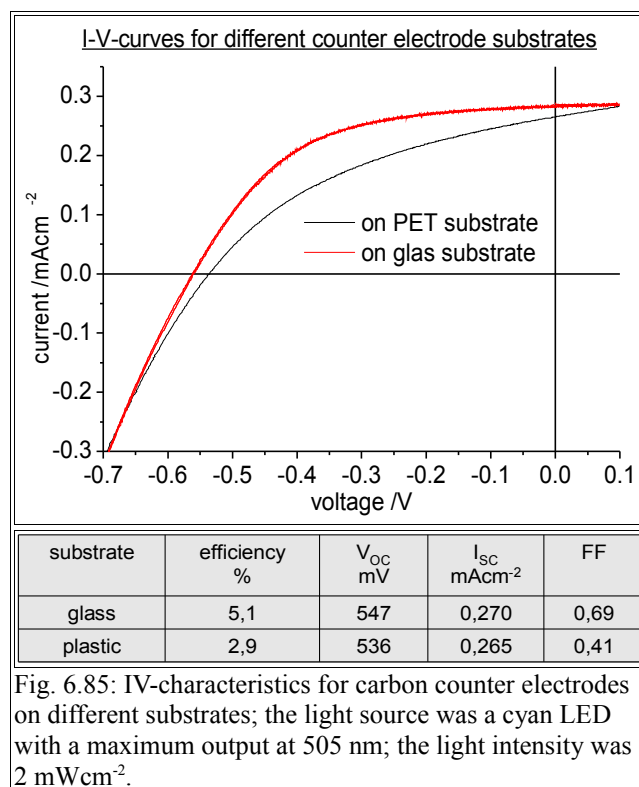| substrate	efficiency %	V_{OC} mV	I_{SC} mAcm^{-2}	FF
glass	5,1	547	0,270	0,69
plastic	2,9	536	0,265	0,41

Fig. 6.85: IV-characteristics for carbon counter electrodes on different substrates; the light source was a cyan LED with a maximum output at 505 nm; the light intensity was 2 mWcm^{-2}.